UNIVERSITY OF SOUTHAMPTON

FACULTY OF PHYSICAL SCIENCES AND ENGINEERING

Optoelectronics Research Centre

Integrated Optical Devices in Side-Polished Fibres

by

Haojie Zhang

A doctoral thesis submitted in partial fulfilment of the requirements for the award of Doctor of Philosophy

November 2017

SUPERVISOR:

Prof. Anna Peacock and ***Dr. Noel Healy***

Dedicated to my family

UNIVERSITY OF SOUTHAMPTON

ABSTRACT

FACULTY OF PHYSICAL SCIENCES AND ENGINEERING

Optoelectronics Research Centre

Doctor of Philosophy

Integrated Optical Devices in Side-Polished Fibres

by Haojie Zhang

Fibre side-polishing technology was explored to meet the need for miniature, multifunctional, and low-loss device platforms for optical applications. Different polishing techniques were investigated to achieve side-polished fibres with low transmission loss, high polished surface quality and long interaction lengths. This side-polished fibre platform was combined with some of the most popular two-dimensional materials, including graphene and molybdenum disulfide, to fabricate integrated optical fibre devices. A high refractive index polyvinyl butyral layer was coated on top of graphene and molybdenum disulfide to enhance the light-matter interaction between the evanescent field of the core guided mode and the two-dimensional materials. By using the excellent photonic properties of graphene, a broadband graphene-based fibre polariser was proposed and fabricated using the low-loss side-polished optical fibre platform. Characterisation of the optical properties revealed that the graphene-based polariser retains low transmission losses and high extinction ratios across an extended telecoms band. The graphene-based fibre device was also utilized to demonstrate a high-speed, in-fibre optical modulator, which realised fast modulation speed and high modulation depth. By using the same design, a low-loss molybdenum disulfide-based all-optical modulator was also demonstrated with a even higher modulation depth. Wavelength-dependent interaction and spectral broadening was observed in the molybdenum disulfide sheet, suggesting that the higher modulation depth was from a resonance-enhanced interaction. To extend the application scenarios of the side-polishing technique, a low loss, wideband multi-core to single-mode fibre coupler was also demonstrated. The coupler was designed to access light from a single core of the multi-core fibre without disrupting the signal propagation in the remaining cores. The coupling ratio between the two fibres could be continuously tuned over the entire spectral band via a simple mechanical displacement method.

Declaration of Authorship

I, **Haojie Zhang**, declare that the thesis entitled **Integrated Optical Devices in Side-Polished Fibres** and the work presented in it are my own and has been generated by me as the result of my own original research. I confirm that:

- This work was done wholly or mainly while in candidature for a research degree at this University;
- Where any part of this thesis has previously been submitted for a degree or any other qualification at this University or any other institution, this has been clearly stated;
- Where I have consulted the published work of others, this is always clearly attributed;
- Where I have quoted from the work of others, the source is always given. With the exception of such quotations, this thesis is entirely my own work;
- I have acknowledged all main sources of help;
- Where the thesis is based on work done by myself jointly with others, I have made clear exactly what was done by others and what I have contributed myself;
- Parts of this work have been published.

Signed: ..... Date: 21/05/2018 .....

Acknowledgements

First of all, I would like to give the greatest gratitude to both of my supervisors Prof. Anna Peacock and Dr. Noel Healy. I really appreciate their generous and insightful guidance as well as wise advice in the past four years of my PhD study, which encouraged me to build my own career that I am so passionate about. I appreciate that they shared with me their valuable experiences, not only in science, but also in life.

Secondly, I would also like to thank all the other colleagues in Nonlinear Semiconductor Photonics Group for their help and supports. In particular, I wish to express my appreciation to Dr. Li Shen, Dr. Antoine Runge, Dr. Fariza Suhailin and Mr Haonan Ren for their kindly help and valuable ecouragement.

Thirdly, I would like to thank my parents, Mr Hongjun Zhang and Ms Shuqin Jiang, as well as my parents in law Mr Zhexiong Li and Ms Chunyan Gao, for their endless love and full support on my PhD study.

Last but not the least, I would like to express my deepest appreciation to my wife, Dr. Xuan Li. Thanks for her love, understanding and support.

List of Publications

Journal Papers

1. **Haojie Zhang**, Noel Healy, Sonali Dasgupta, John R. Hayes, Marco N. Petrovich, David J. Richardson, Anna C. Peacock, "A tuneable multi-core to single mode fiber coupler", *IEEE Photonics Technology Letters*, Vol. 29, pp. 591-594, Apr. 2017.

2. **Haojie Zhang**, Noel Healy, Li Shen, Chung Che Huang, Daniel W. Hewak, Anna C. Peacock, "Graphene-based fiber polarizer with PVB-enhanced light interaction", *Journal of Lightwave Technology*, Vol. 34, pp. 3563-3567, Aug. 2016.

3. **Haojie Zhang**, Noel Healy, Li Shen, Chung Che Huang, Daniel W. Hewak, Anna C. Peacock, "Enhanced all-optical modulation in a graphene-coated fibre with low insertion loss", *Scientific Reports*, Vol. 6, p. 23512, Mar. 2016.

4. **Haojie Zhang**, Noel Healy, Antoine F. J. Runge, Chung Che Huang, Daniel W. Hewak, Anna C. Peacock, "Optical-Resonance-Enhanced Nonlinearities in a MoS_2-Coated Single-Mode Fiber", *Optics Letters*, Vol. 43, no. 10, Apr. 2018.

Conference Papers

1. **Haojie Zhang**, Noel Healy, Sonali Dasgupta, John R. Hayes, Marco N. Petrovich, David J. Richardson, and Anna C. Peacock, "A tuneable multi-core to single mode fiber coupler", *IEEE Photonics Conference*, 1-5 October 2017, Lake Buena Vista, Florida, USA.

2. Noel Healy, **Haojie Zhang**, and Anna C. Peacock, "Functionalized Optical Fibers", *the Pacific Rim Conference on Lasers and Electro-Optics*, 31 July - 4 Aug 2017, Singapore. (Invited)

3. **Haojie Zhang**, Noel Healy, Antoine Runge, Chung Che Huang, Dan Hewak, Anna C. Peacock, "MoS_2 coated side polished fibers for nonlinear optics", *The European Conference on Lasers and Electro-Optics and the European Quantum Electronics Conference*, 25-29 June 2017, Munich, Germany.

4. Artemios Karvounis, Davide Piccinotti, Angelos Xomalis, **Haojie Zhang**, Vassili Savinov, Behrad Gholipour, Yongmin Jung, Anna C. Peacock, Eric Plum, Kevin F. MacDonald, David J. Richardson, Nikolay I. Zheludev, "Active metadevices on optical fibre platforms", *MRS Spring Meeting*, 17-21 April 2017, Phoenix, USA.

5. Angelos Xomalis, Davide Piccinotti, Artemios Karvounis, **Haojie Zhang**, Vassili Savinov, Behrad Gholipour, Yongmin Jung, Anna C. Peacock, Eric Plum, Kevin F. MacDonald, David J. Richardson, Nikolay I. Zheludev, "Fibre-coupled photonic meta devices", *6th International Topical Meeting on Nanophotonics and Metamaterials*, 4-7 January 2017, Seefeld (Tirol), Austria.

6. Noel Healy, **Haojie Zhang**, Anna C. Peacock, "Functionalized optical fibers for non-linear optics", *Asia Communications and Photonics Conference*, 02-05 November 2016, Wuhan, China. (Invited)

7. **Haojie Zhang**, Noel Healy, Li Shen, Chung Che Huang, Dan Hewak, Anna C. Peacock, "In-fiber all-optical modulation based on an enhanced light-matter interaction with graphene", *Conference on Lasers and Electro-Optics*, 05-10 June 2016, San Jose, USA.

8. **Haojie Zhang**, Noel Healy, Li Shen, Hans C. Mulvad, David J. Richardson, Anna C. Peacock, "Tunable 7-core fiber coupler based on a side-polishing technique", *Conference on Lasers and Electro-Optics*, 05-10 June 2016, San Jose, USA.

9. **Haojie Zhang**, Noel Healy, Li Shen, Chung Che Huang, Nikos Aspiotis, Dan Hewak, Anna C. Peacock, "High-performance low-loss fibre Polarizer based on graphene and PVB", *The European Conference on Lasers and Electro-Optics and the European Quantum Electronics Conference* , 21-25 June 2015, Munich, Germany.

Contents

List of Figures

List of Tables

Nomenclature

$2D$	Two-dimensional.
$TMDCs$	Transition-metal dichalcogenides.
MoS_2	Molybdenum disulfide.
$MCFs$	Multi-core fibres.
SDM	Space-division multiplexing.
CVD	Chemical vapor deposition.
SEM	Scanning electron microscope.
FOM	Figure of merit.
SMF	Single-mode fibre.
OSA	Optical spectrum analyser.
MFC	Mass flow controller.
CCD	Charge-coupled device.
$FWHM$	Full-width at half maximum.
PVB	Polyvinyl butyral.
FEM	Finite element method.
CW	Continuous wave.
BS	Beam splitter.
LA	Lock-in amplifier.
FD	Frequency driver.
PD	Photo-diode.
ASE	Amplified spontaneous emission.

Chapter 1

Introduction

This introductory chapter starts with a basic overview of the background and the motivation of the research work. Then, Section 1.1 introduces the outline of this thesis and Section 1.2 presents the major achievements during the research. Finally, Section 1.3 gives details of my contribution to the work presented in this thesis and outlines the various contributions of the team members.

Side-Polished Optical Fibres

The optical fibre has truly revolutionised the world of telecommunications, mainly because of its capacity to transmit large quantities of information. Progress in this field has enabled the parallel development of optical fibre devices, in which the principle operations involve modulation of the amplitude, wavelength, polarisation, or phase of the transmitted light [1]. Fibre-based devices have several advantages over conventional bulk devices, such as low weight, high sensitivity, geometric flexibility, fast response and immunity to electromagnetic interference [2]. The main task of this work is to develop a new range of optical fibre devices that can take advantage of recent demonstrated two-dimensional (2D) material technology. It will follow the development of optical fibre devices from the design and characterization stage to the demonstration of practical all-fibre devices. The fabrication of these hybrid structures will utilize optical fibres as templates onto which different functional materials will be incorporated. The light propagating through the fibre can then directly interact with the materials. Various geometries exist to access propagating light within a fibre by modifying its structure, including fibre etching, tapering or polishing [3].

Of these techniques, fibres that have been tapered or etched tend to be more fragile than the polished structures [4]. Thus, fibre polishing has long been used for lateral interaction with the propagating core mode for device fabrication [5]. In fibre polishing, a portion of fibre cladding is removed over a length of several millimetres or even centimetres via abrasive action to form a polished region. The resulting fibres are known as side-polished fibres and the fibre cross-section at the polishing region is similar to the upper-case letter 'D', as shown in Figure 1.1. A schematic representation of a side-polished fibre is shown in Figure 1.2. Side-polished fibres represent ideal miniaturized platforms to realise interaction between the guided light and the external environment for optical device fabrication. Optical devices based on side-polished fibre platforms have several significant advantages like controlled interaction lengths and interaction strengths between transmitted light and overlayers and almost no back reflection. Numerous applications already exist for side-polished fibre components, such as tunable photonic crystal fibre couplers [6], fibre optic surface plasmon resonance sensors [7], broadband polarisers for telecommunications [8], temperature sensors [9], and chemical sensors for industrial and medical applications [10]. Such devices play an increasingly important role and have been widely used in communications, medical treatment, aviation, chemical sensing, etc [2]. To meet the need for miniature, multifunctional, and sensitive device platforms, a side-polished fibre with low transmission loss, high surface quality and selectable interaction length is required. However, existing polishing approaches could not satisfy all these requirements, thus it was necessary to develop a new fibre polishing method, which will be described in detail in Chapter 3.

2D Materials

Owing to their wide range of exceptional properties, 2D materials including graphene and transition-metal dichalcogenides (TMDCs), such as molybdenum disulfide (MoS_2), have emerged as exciting media for the development of highly functional optoelectronic devices. Among these, graphene has become one of the most studied materials due to its unique optical and electrical properties. Graphene is a strictly 2D material formed by a single layer of carbon atoms packed into a hexagonal lattice, as shown in Figure 1.3 [11]. The unique structure of graphene allow multi-functions such as light emission, modulation, and detection to be realized in one material [12]. Depending on the application, another

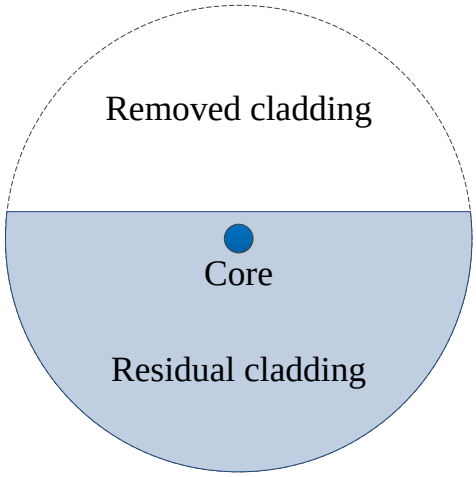

Figure 1.1: Cross-section of side-polished region.

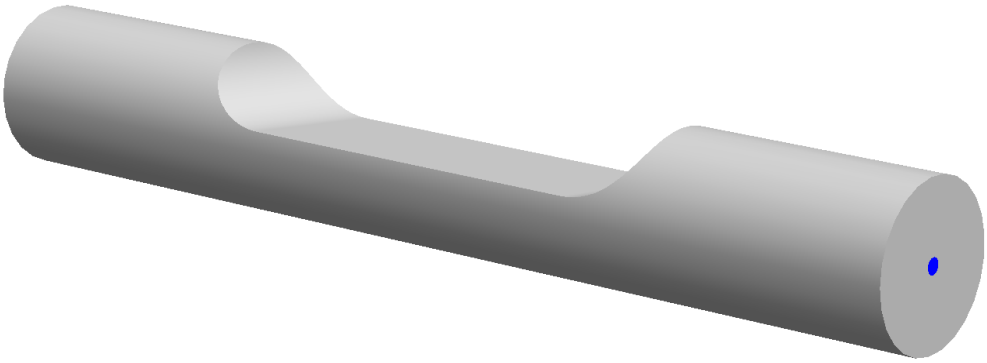

Figure 1.2: Schematic of the side-polished fibre.

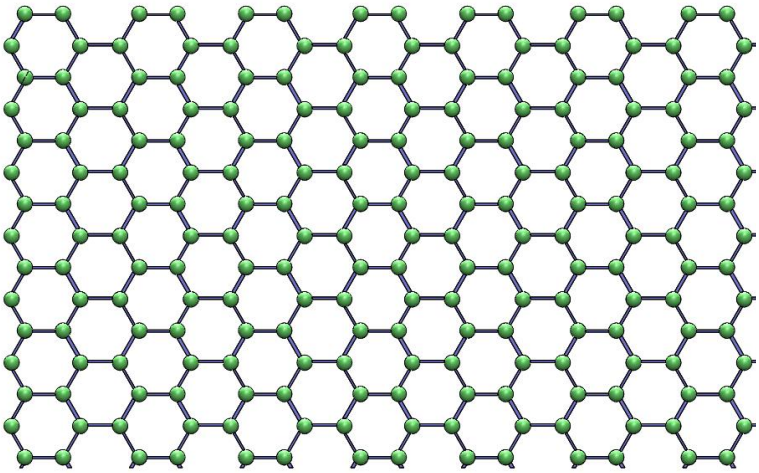

Figure 1.3: Schematic top view of mono-layer graphene. Green: carbon atoms.

advantage of graphene, compared to silicon and III-V semiconductors, is that the electron and hole mobility are equally high, due to the symmetric band structure [11]. Owing to these desirable optoelectronic properties, graphene has been considered for a wide array of optical devices including a broadband fibre polarisers [8], optical limiters [13], wavelength converters [14], all-optical modulators [15], Q-switched or mode-locked ultrafast lasers [16, 17], and ultra-broadband photodetectors [18]. Compared with conventional devices, graphene-based optical devices can be more compact, operate over a broad wavelength band, and offer lower optical propagation losses. Particularly remarkable is its broadband nature so that it can respond to signals spanning the microwave to ultraviolet spectral regions, including the commonly used fibre-optic communication band [8]. In this work, these features has been utilised based on a single mode side-polished fibre platform to develop a low loss, high extinction ratio graphene-based polariser, which will be discussed in detail in Chapter 5 and a fast-speed, high modulation depth all-optical modulator, which will be presented in Chapter 6.

Despite the remarkable properties of graphene, its zero bandgap retards its application in logic electronics [19]. TMDCs have attracted great attention due to their 2D layer structure analogous to graphene [19]. TMDCs, such as MoS_2, $MoSe_2$, WS_2 and WSe_2, consist of hexagonal layers of metal atoms (W or Mo) sandwiched between two layers of chalcogen atoms (S or Se) [20]. The quantum structure of TMDCs has three sub-layers where two layers of chalcogen atoms are separated by a layer of metal atoms. TMDCs can offer properties that are unattainable in graphene since they are often semiconductors, and their optoelectronic properties can be tuned quite dramatically by controlling the material thickness. For example, in some materials, like MoS_2, it is possible to tune the electronic bandgap from indirect in a few layers, to direct in a single layer [21], which is of significant interest for the development of lasers. The layer-dependent bandgap structure makes MoS_2 a useful material for fabricating a variety of optoelectronic devices including gigahertz transistors [22], high sensitivity chemical sensors [23]. In fact, in this material, as well as controlling the bandgap, the layer thickness can also be used to control the size of the nonlinear coefficients which is useful for applications involving high power light. Mak et al. has shown that second order nonlinearity $\chi^{(2)}$ of MoS_2 turns on when the layer number is odd in Ref [21] and Wang et al. discusses third order nonlinearity $\chi^{(3)}$ of MoS_2 in Ref [24]. Several other researchers have also discussed its saturable absorption

property [25, 26] as well as its application for mode-lock or Q-switched lasers [27, 28]. But most of these nonlinear-related studies have so far focused on wavelengths less than 1000 nm, with the nonlinear optical properties of MoS_2 within telecoms band being less well reported. Thus, in Chapter 7, the nonlinear properties of a few-layer MoS_2 film with in near-infrared wavelength range will be presented based on a single mode side-polished fibre platform. Similar to graphene, the saturable absorption feature of MoS_2 has also been utilised to demonstrate an all-optical modulator with even higher modulation ratio compared to the graphene-based modulator.

Multi-Core Fibres

The side-polishing technique developed in this work was also used in multi-core fibres (MCFs). MCFs, defined as fibres with an array of physically distinct single-mode cores, are currently experiencing increased research attention due to heightened interest in space-division multiplexing (SDM) technologies [29]. This surge in activity is primarily fuelled by the need to increase the capacity of the networks that modern day life has come to depend on [29]. SDM over MCFs has been proposed as an attractive technology to overcome the capacity limit of current optical communication systems [30]. Actually, MCFs have been used to realise the highest capacities and longest transmission distances demonstrated so far in SDM systems [29]. The main type of MCF is the uncoupled-core MCF, which utilizes each core as an individual spatial channel, thus requiring large core-to-core spacing for low core-to-core crosstalk [31, 32]. Another type of MCF is the coupled-core MCF, which has a shorter core-to-core distance and a higher spatial density compared to uncoupled-core MCFs to permit strong mode coupling between cores [32, 33]. In Chapter 8, a multi-core to single-mode fibre coupler will be discussed using the side polishing technique. The MCF used in this work is an uncoupled-core MCF, thus each core can be considered separately.

1.1 Outline of Thesis

Chapter 1 presents a brief introduction of the work. It also outlines the thesis structure, summarises the key achievements, and lists details of the work contribution.

Chapter 2 provides the background theory to the work. It begins by giving a brief

description of optical fibre structures and light propagation in fibres. Then, the basic optical proprieties of 2D materials used in this work, graphene and MoS_2, are discussed.

Chapter 3 describes the development and benchmarking of the side-polished fibres that are used throughout the work. The investigated polishing processes are discussed in detail and the key procedures to realise ultra-smooth polishing surfaces are indicated. The optical characterisation properties of the polished fibres are presented across a broadband wavelength range.

Chapter 4 addresses the fabrication methods of integrated optical devices based on 2D materials and side-polished fibres. It begins with chemical vapor deposition (CVD) growth methods of graphene and MoS_2. Raman spectroscopy measurements and scanning electron microscope (SEM) measurements were performed on the 2D material samples to reveal the film quality and thickness. Then, the methods to separate the 2D materials and the growth substrates are discussed, as well as the methods used to transfer the 2D films onto the side-polished fibre platforms.

Chapter 5 presents a novel approach to producing a low loss, high extinction ratio graphene-based fibre polariser. The device design is discussed first, then, simulations used to indicate the PVB-enhanced light-matter interaction are presented. Finally, characterisation results of the optical experiments show the device performance across a broadband wavelength range.

Chapter 6 presents demonstration of an all-optical modulator using the graphene-based fibre device. It starts with nonlinear measurements of the device to show its saturable absorption. Finally, using a pump-probe setup, an all-optical modulation was tested with a high modulation depth achieved.

Chapter 7 presents nonlinear properties of a MoS_2-based optical device based on the side-polished fibre. It starts with linear measurements of the device. Subsequent nonlinear transmission measurements show evidence of spectral broadening and saturable absorption due to the MoS_2 sheet. Based on this, an all-optical modulation experiment was also undertaken using a pump-probe setup to compare its performance with the graphene-based device.

Chapter 8 presents a multi-core to single-mode fibre coupler using the side polishing technique developed in Chapter 3. The coupler design and fabrication are discussed at first.

Then, an experiment was performed to characterize the transmission losses of the coupler and check the coupling ratio response via different displacements. Finally, simulation results are used to explain the experimental results.

Chapter 9 summarises the work.

1.2 Key Achievements

A brief summary of the key achievements during the author's PhD study are listed here:

1. A novel method for producing side polished fibres which enable strong light-matter interaction while maintaining an ultra-low transmission loss has been designed and experimentally demonstrated. The side-polished fibre can be used as an excellent platform on which to exploit the rich optical functionalities of 2D materials and for optical device fabrication.

2. A graphene-based fibre polariser with a high extinction ratio $\sim$37.5 dB and a low device loss $\sim$1 dB at 1550 nm has been designed and experimentally demonstrated with an enhanced light-graphene interaction. An extinction ratio greater than 26 dB was recorded across the wavelength range 1425 to 1600 nm, with an additional value of 13 dB at 2000 nm.

3. A robust and stable all-optical graphene-based fibre modulator with an extinction ratio as high as 9 dB and operation bandwidth of 0.5 THz has been designed and experimentally demonstrated. When compared to previous similar devices, our approach presents a significant improvement in performance in all key measures to simultaneously obtain low loss, high speed, and high modulation depth. The figure of merit (FOM) of the modulator was double that of the state of the art at the time. This simple and effective scheme for enhanced light-matter interaction could easily be adapted for other 2D materials.

4. A few-layer MoS_2-based device has been designed and experimentally demonstrated for use in nonlinear optical applications. Strong wavelength-dependent interaction and spectral broadening was observed in this device, which suggested a resonance-enhanced light-matter interaction. An all-optical modulator with a higher modulation ratio of 20 dB was realised in this device compared to the graphene-based device.

5. A tunable wideband multi-core to single-mode fibre coupler with a low device loss

$\sim$1 dB has been designed and experimentally demonstrated. The robust and low loss tunable coupler enables light access from a single core of the multi-core fibre without disrupting the signal propagation in the remaining cores.

1.3 Contributions

The author is responsible for all the work presented in this thesis under the supervision of Prof. Anna Peacock and Dr. Noel Healy.

Fabrication of all side-polished fibres used in this work was carried out by the author. The aluminium blocks were designed by the author and fabricated by the ORC workshop. Fabrication of the graphene and MoS_2 films and their Raman spectroscopy were performed by Dr. Chung Che Huang.

All of the optical images in this work were acquired by the author. The SEM images in Chapter 3 were acquired by the author. The SEM image in Chapter 4 was acquired by Dr Oleksandr Buchnev with assistance of Dr. Chung Che Huang and the author.

All the experiments in Chapter 3 to Chapter 8 were carried out and analysed by the author. Dr. Chung Che Huang helped in experiments in Chapter 4. Dr. Li Shen helped in experiments in Chapter 5. Dr. Antoine Runge helped in experiments in Chapter 7. The simulations in Chapter 5 were performed by the author. The simulations in Chapter 8 were performed by Dr. Sonali Dasgupta with the assistance of the author.

Chapter 2

Background

2.1 Introduction

In this chapter, light propagation theory in optical fibres will be discussed as well as the optical properties of graphene and MoS_2. The optical fibres form the platforms to be integrated with 2D materials for the fabrication of optical devices. The structures of optical fibres, which will strongly influence the propagating light, will be discussed at first. Then, the optical mode theory and the evanescent coupling theory will be presented. Finally, the optical properties of graphene and MoS_2, including their band structures, optical absorptions and saturable absorptions, will be introduced in detail. These features underpin the working principle of the integrated optical devices developed in this work which will be presented in the following chapters.

2.2 Light Propagation in Optical Fibres

2.2.1 Structure of Optical Fibres

An optical fibre is a long, flexible, cylindrical waveguide that can transport light in the visible or infrared region of the electromagnetic spectrum depending on the core material [34]. It is composed of a centre core region in which the light is guided and the core is surrounded by a cladding region. The fibre is usually coated with a polymer protective coating that protects it from damages. The core and cladding are typically made of dielectric materials such as silica. Mostly, the silica in the core is doped with germanium to raise

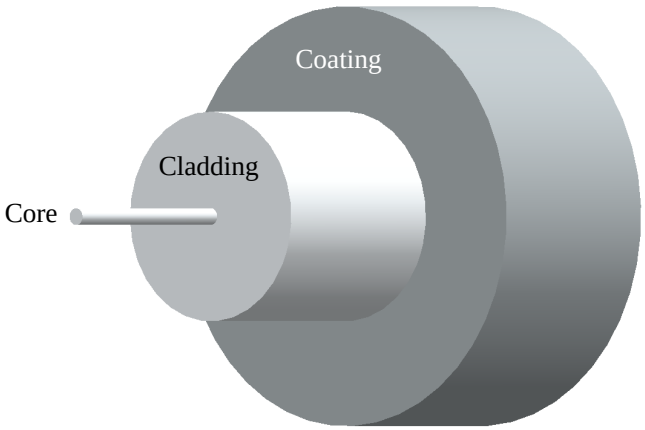

Figure 2.1: The structure of a standard SMF.

its refractive index relative to the cladding silica, so as to permit the light to propagate in the core via total internal reflection [34]. Optical fibres can be classified into two categories, single-mode and multimode. A single-mode fibre (SMF) has a small diameter core (typical around 9 μm for operation wavelengths 1310 nm and 1550 nm) that allows only one mode of light to propagate, while a multimode fibre has a large diameter core (typical 50 μm or 62.5 μm) that allows multiple modes of light to propagate. The cladding diameter of these single-mode and multimode fibres is usually around 125 μm and the outside buffer diameter is around 250 μm. A structure illustration of a standard SMF can be seen in Figure 2.1. The refractive index profile of a stepped-index SMF is shown in Figure 2.2. The two dimensionless quantities n_1 and n_2 are refractive indexes of the core and cladding, respectively. Δn is refractive index difference between n_1 and n_2 and defined in Equation 2.1 [34]. Most optical fibres satisfy the 'weak guidance' criteria, meaning that the relative refractive index difference Δn is very small and less than 1% typically [35].

$$\Delta n = \frac{n_1^2 - n_2^2}{2\,n_1^2} \cong \frac{n_1 - n_2}{n_1}. \tag{2.1}$$

The numerical aperture (NA), used to characterise the light-gathering capacity of an optical fibre, is defined in Equation 2.2.

$$NA = \sqrt{n_1^2 - n_2^2}. \tag{2.2}$$

Large NA optical fibres have a higher angle range of light rays that can be captured within the fibre core. The number of allowable modes of an optical fibre is determined by

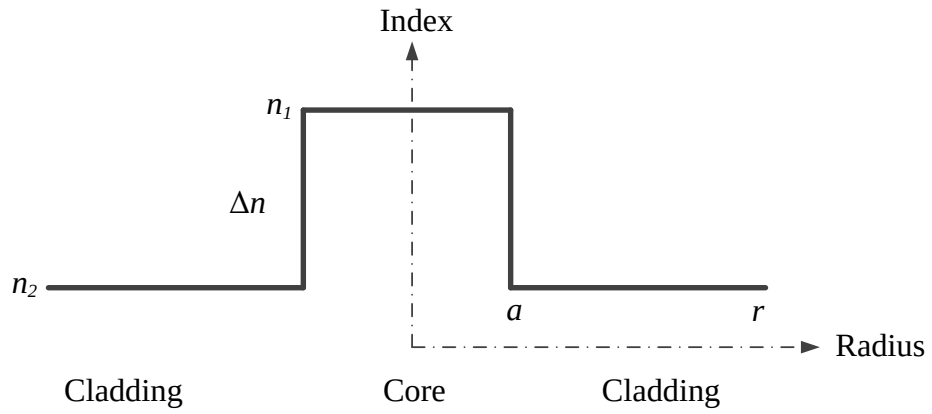

Figure 2.2: The refractive index profile of a standard SMF.

Table 2.1: Sellmeier coefficients for undoped silica cladding and doped silica core.

Sellmeier coefficient	Undoped silica cladding	Doped silica core
a_1	0.6968	0.6867
b_1	0.06907	0.07268
a_2	0.4082	0.4348
b_2	0.1157	0.1151
a_3	0.8908	0.8966
b_3	9.901	10.00

the V parameter and can be approximated by Equation 2.3 [35].

$$V = \frac{2\,\pi\,a}{\lambda}\sqrt{n_1^2 - n_2^2} = k_0\,a\sqrt{n_1^2 - n_2^2}, \tag{2.3}$$

where λ is the free-space wavelength of the light, a is the radius of the core, and k_0 is the free-space wave number. A fibre is considered as single-mode if the normalised V of the fibre is less than the normalised cut-off value of the second mode. Typically, a stepped-index fibre will allow single-mode operation if $V < 2.405$ [35].

For a standard SMF with a germanium-doped silica core and an undoped silica cladding, the wavelength dependent refractive index n of the core and cladding are given in Equation 2.4 using the Sellmeier equation for wavelengths between 0.21 μm and 2.2 μm [36]. The coefficients a_1, a_2, a_3, b_1, b_2, b_3 are given in Table 2.1 [36], and λ is the wavelength in microns. The refractive indexes of the fibre core and cladding between 1 μm and 2 μm are

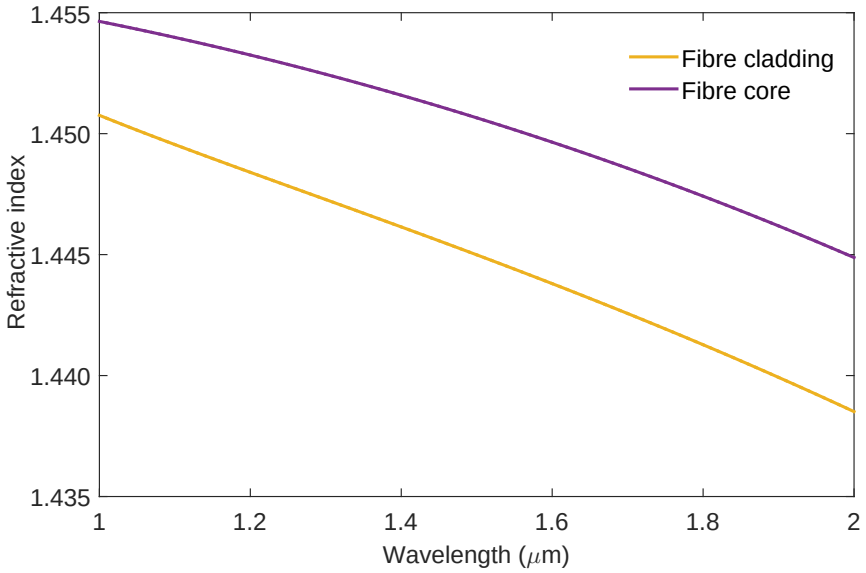

Figure 2.3: Refractive index of the fibre core and cladding.

plotted in Figure 2.3.

$$n(\lambda) = \sqrt{1 + \frac{a_1\lambda^2}{\lambda^2 - b_1^2} + \frac{a_2\lambda^2}{\lambda^2 - b_2^2} + \frac{a_3\lambda^2}{\lambda^2 - b_3^2}}. \tag{2.4}$$

2.2.2 Mode Theory

Mode theory is used to describe the types of waves able to propagate along an optical fibre. Propagating light in an optical fibre is affected by a number of physical mechanisms. As a type of electromagnetic wave, propagating light can be described by solving Maxwell's equations subjected to the cylindrical conditions of the fibre as follows [37]:

$$E_y = -\frac{j\beta}{k^2}\frac{\partial E_z}{\partial y} + \frac{j\omega\mu}{k^2}\frac{\partial H_z}{\partial x}, \tag{2.5}$$

$$H_y = -\frac{j\omega\varepsilon}{k^2}\frac{\partial E_z}{\partial x} - \frac{j\beta}{k^2}\frac{\partial H_z}{\partial y}, \tag{2.6}$$

$$E_x = -\frac{j\beta}{k^2}\frac{\partial E_z}{\partial x} - \frac{j\omega\mu}{k^2}\frac{\partial H_z}{\partial y}, \tag{2.7}$$

$$H_x = \frac{j\omega\varepsilon}{k^2}\frac{\partial E_z}{\partial y} - \frac{j\beta}{k^2}\frac{\partial H_z}{\partial x}, \tag{2.8}$$

$$k^2 = (k_0\, n)^2 - \beta^2, \tag{2.9}$$

$$(\frac{\partial^2}{\partial x^2} + \frac{\partial^2}{\partial y^2} + k^2)H_z = 0, \tag{2.10}$$

$$(\frac{\partial^2}{\partial x^2} + \frac{\partial^2}{\partial y^2} + k^2)E_z = 0, \tag{2.11}$$

where β is the propagation constant, k is the wave-number, ω is the angular frequency, ε is the permittivity, μ is the permeability, n is the refractive index, the free space wave-number $k_0 = 2\pi/\lambda$, E_z and H_z are z-components of the electric and magnetic field distributions for the transverse waves respectively. When applying the boundary conditions at the core-cladding interface, transverse field components of E_z and H_z can be solved using Equations 2.5 to 2.8 and longitudinal field components of E_z and H_z can be solved using the Equations 2.9 to 2.11. A brief introduction is presented here since complex mathematical calculations are not the focus of this chapter. Electromagnetic waves are considered in a cylindrical coordinate system (r, ϕ, z). Considering the waves propagate along the z-axis, E_z and H_z can be solved using [37]:

$$E_z(r,\phi,z) = E_z(r,\phi)exp[-j(\omega t\, -\, \beta z)], \tag{2.12}$$

$$H_z(r,\phi,z) = H_z(r,\phi)exp[-j(\omega t\, -\, \beta z)]. \tag{2.13}$$

By solving Equation 2.12 to 2.13, the wave equations for both E_z and H_z in the cylindrical coordinate system can be obtained as follows [37]:

$$\frac{\partial^2 E_z}{\partial r^2} + \frac{1}{r}\frac{\partial E_z}{\partial r} + \frac{1}{r^2}\frac{\partial^2 E_z}{\partial \phi^2} + (\frac{\omega^2}{v^2} - k^2)E_z = 0, \tag{2.14}$$

$$\frac{\partial^2 H_z}{\partial r^2} + \frac{1}{r}\frac{\partial H_z}{\partial r} + \frac{1}{r^2}\frac{\partial^2 H_z}{\partial \phi^2} + (\frac{\omega^2}{v^2} - k^2)H_z = 0, \tag{2.15}$$

where $v = c/n$ is the speed of light in the dielectric medium of n and c is the vacuum light speed. Fibre modes are called transverse-electric (TE) modes when $E_z = 0$, transverse-magnetic (TM) modes when $H_z = 0$, and hybrid HE or EH modes if both E_z and H_z are non zeros. Equation 2.14 and Equation 2.15 are solved for the regions in the core and cladding. Since the field distribution in the core and cladding regions have the same form, the electric field corresponds to a non-uniform wave travelling in the z-direction [35]. Specifically, when light propagates in a fibre core, it is a standing wave in the fibre core and a evanescent wave in the cladding region. The evanescent wave decays exponentially from the core cladding interface. This evanescent field allows the light to be accessed in a manner useful to develop integrated optical fibre devices.

2.2.3 Evanescent Coupling Theory

The modes of two or more closely spaced waveguides can exchange energy via evanescent coupling, which forms the operation principle of some optical couplers [38]. To predict the performance of the optical coupling, it is necessary to solve Maxwell's equations governing the electromagnetic fields. The total field of the coupled waveguides can be expressed as a linear combination of the mode fields [39]. By using the coupled mode theory [40], the power guided in the entire coupled waveguides can be defined as follow:

$$P(z) = \frac{1}{4}\int (E \times H^* + E^* \times H) \cdot \hat{z} da = \sum_{ij} a_i^*(z) P_{ij}\, a_i(z). \tag{2.16}$$

where a is the amplitude. By using the mode-matching method [41], the guided mode in each waveguide is described as follows [40]:

$$P_1(z) = cos^2(Sz) + \left[\frac{cos(\eta) - sin(\alpha)sin(\alpha+\eta)}{cos(\alpha)}\right]^2 sin^2(Sz), \tag{2.17}$$

$$P_2(z) = sin^2(\alpha)cos^2(Sz) + sin^2(\eta)sin^2(Sz), \tag{2.18}$$

$$S = \sqrt{\delta^2 + \tau^2}, \tag{2.19}$$

where δ is the phase mismatch factor, τ is the coupling coefficient, η is defined as $tan(\eta) = \tau/\delta$, P_1 is the remaining output power and P_2 is the coupled output power. Thus, the optical power at two outputs can be calculated numerically.

2.3 Optical Properties of Graphene and MoS_2

2.3.1 Band Structure and Optical Absorption of Graphene

The hexagonal structure and corresponding Brillouin zone of graphene is shown in Figure 2.4(a) and (b), correspondingly [11]. The hexagonal structure consists of two sub-lattices A, B, as shown in Figure 2.4(a), and the lattice parameters can be written as [11]:

$$a_1 = \frac{a}{2}(3, \sqrt{3}), \;\; a_2 = \frac{a}{2}(3, -\sqrt{3}), \tag{2.20}$$

$$b_1 = \frac{2\pi}{3a}(1, \sqrt{3}), \;\; b_2 = \frac{2\pi}{3a}(1, -\sqrt{3}), \tag{2.21}$$

$$\delta_1 = \frac{a}{2}(1, \sqrt{3}), \;\; \delta_2 = \frac{a}{2}(1, -\sqrt{3}), \;\; \delta_3 = -a(1, 0). \tag{2.22}$$

where a = 0.142 nm is the carbon to carbon distance [11]. Dirac points K and K', as shown in Figure 2.4(b), are of particular importance for the physics of graphene, and their positions are given as [11]:

$$K = (\frac{2\pi}{3a}, \frac{2\pi}{3\sqrt{3}a}), \;\; K' = (\frac{2\pi}{3a}, -\frac{2\pi}{3\sqrt{3}a}). \tag{2.23}$$

Then, the tight-binding Hamiltonian for electrons in graphene can be expressed as [11]:

$$H = -t \sum_{(i.j),\sigma} (a^{\dagger}_{\sigma,i}\, b_{\sigma,j} + H.c.) - t' \sum_{((i.j)),\sigma} (a^{\dagger}_{\sigma,i}\, a_{\sigma,j} + b^{\dagger}_{\sigma,i}\, b_{\sigma,j} + H.c.), \tag{2.24}$$

where $a_{\sigma,i}$ annihilates and $a^{\dagger}_{\sigma,i}$ creates an electron on sub-lattice A (same definition for sub-lattice B). $t \approx 2.8$ eV is the nearest-neighbour hopping energy between different sub-lattices, and $t^{'}$ is the next nearest-neighbour hopping energy in the same sub-lattice [11]. The energy bands derived from this Hamiltonian can be expressed as [42]:

$$E_{\pm}(k) = \pm t\sqrt{3 + f(k)} - t' f(k), \tag{2.25}$$

$$f(k) = 2\,cos(\sqrt{3}k_y a) + 4\,cos(\frac{\sqrt{3}}{2}k_y a)\,cos(\frac{3}{2}k_x a). \tag{2.26}$$

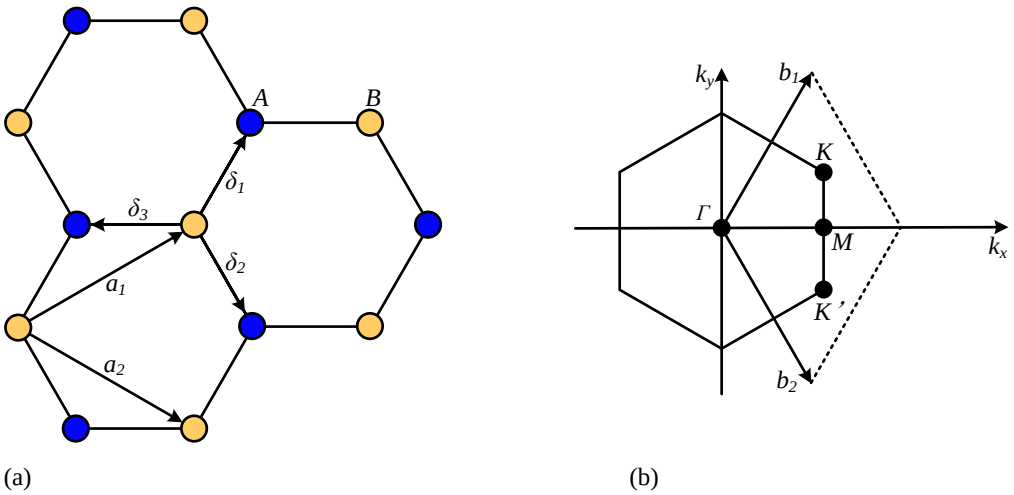

Figure 2.4: (a) Hexagonal lattice structure of graphene consisting of sub-lattices A, B. a_1, a_2 are the lattice unit vectors, and $\delta_{1,2,3}$ are the nearest-neighbour vectors. (b) Corresponding Brillouin zone of graphene. K and K' are Dirac points, and b_1, b_2 are the reciprocal lattice vectors. Figures from Ref. [11].

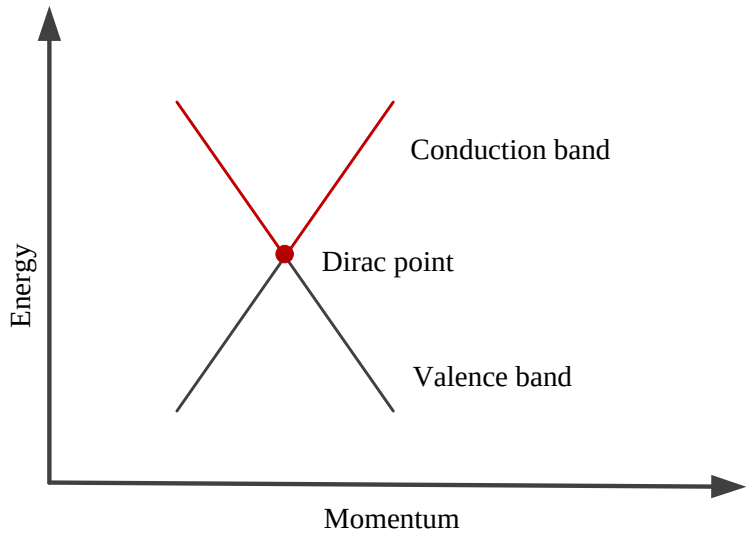

Figure 2.5: Schematic band structure of graphene.

The linear dispersion relation for both valence band and conduction band can be obtained by expanding Equation 2.25 and Equation 2.26 in the vicinity of K or K' points and is given as follows [11]:

$$E(\vec{k}) = \pm\hbar v_F|\vec{k}|, \tag{2.27}$$

$$v_F = \frac{\sqrt{3}}{2\hbar} t a_0 \approx 10^6 m/s, \tag{2.28}$$

where v_F is the Fermi velocity of monolayer graphene. Unlike three-dimensional materials, which have a parabolic band gap between the lower-energy valence band and the higher-energy conduction band, the energy band of 2D graphene has the form of smooth-sided cones, which meet at the Dirac points (K or K') as shown in Figure 2.5 [11]. This unique linear and gapless band structure gives rise to some remarkable properties. For example, graphene has a strong uniform absorption across a broadband wavelength range [43]. The transmittance of a freestanding monolayer graphene can be calculated by applying the Fresnel equations in the thin-film limit for a material with a fixed universal optical conductance, $G_0 = e^2/(4\hbar) \approx 6.08 \times 10^{-5}\Omega^{-1}$, as [44]:

$$T = (1 + 0.5\pi\alpha)^{-2} \approx 1 - \pi\alpha \approx 97.7\%. \tag{2.29}$$

Thus, the absorption can be expressed by a simple formula $\pi\alpha$, where the fine structure constant $\alpha = e^2/(4\pi\epsilon_0\hbar c) \approx 1/137$ [43]. It can be seen that the optical absorption of 2.3% is only determined by the universal physical constants $e, \hbar, c$ and is wavelength independent due to the zero bandgap structure of graphene [43]. The absorption of graphene also increases linearly with the number of layers [43]. Considering it only has one atomic layer, such absorption is quite dramatic. This flat, broadband and high quantum efficiency absorption make it an excellent choice of material to extend the operation bandwidth of integrated optical devices [45]. Thus, graphene is expected to respond to wide-band signals spanning microwave to ultraviolet, including the commonly used fibre-optic communication band at 1550 nm [8]. Graphene also has a tunable optical property, due to its density of states vanishing at the Dirac point. The Fermi energy can be tuned electrically or chemically, making it possible to engineer additional optoelectronic functionality into the graphene-based devices.

The broadband optical absorption feature has been utilised to develop a graphene-based fibre polariser which will be discussed in detail in Chapter 5. To simulate the mode effective index and the mode power attenuation for the graphene-based device, the refractive index of graphene has to be known. The complex refractive index of graphene n_g can be calculated from its permittivity ϵ, which can be obtained from the complex optical conductivity σ, consisting of intraband σ_{intra} and interband σ_{inter} contributions as has been discussed in Section 5.2 [46, 47],

$$\sigma(\omega) = \sigma_{intra}(\omega) + \sigma_{inter}(\omega) = \sigma_{intra}(\omega) + \sigma'_{inter}(\omega) + \sigma''_{inter}(\omega), \tag{2.30}$$

$$\sigma_{intra}(\omega) = \frac{e^2}{\pi\hbar^2(\tau_1 - i\omega)}, \tag{2.31}$$

$$\sigma'_{inter}(\omega) = \frac{e^2}{4\hbar}\left(1 + \frac{1}{\pi}\arctan\frac{\hbar\omega - 2\mu}{\hbar\tau_2} - \frac{1}{\pi}\arctan\frac{\hbar\omega + 2\mu}{\hbar\tau_2}\right), \tag{2.32}$$

$$\sigma''_{inter}(\omega) = -\frac{e^2}{8\pi\hbar}\ln\frac{(2\mu + \hbar\omega)^2 + \hbar^2\tau_2^2}{(2\mu - \hbar\omega)^2 + \hbar^2\tau_2^2}, \tag{2.33}$$

$$\epsilon(\omega) = 1 + \frac{i\sigma(\omega)}{\omega\epsilon_0 d_g}, \tag{2.34}$$

$$n_g(\omega) = n_{real}(\omega) + ik_{imag}(\omega) = \sqrt{\epsilon(\omega)}, \tag{2.35}$$

where e is the elementary charge, $\hbar$ is the reduced Planck constant, ω is the angular frequency of incident light, μ is the chemical potential of graphene, τ_1 and τ_2 are the relaxation rates for the interband and intraband transitions, ϵ_0 is the vacuum permittivity, and n_{real} and k_{imag} are the refractive index and extinction coefficient, respectively. $d_g = 0.7$ nm is an estimated thickness of the mono-layer graphene. Considering the initial doping, substrate induced doping, and the overlayer doping, mono-layer graphene grown by the CVD method in this work is estimated to have a chemical potential on the order of 0.1 eV [48]. By using equation 2.30 to 2.33, the optical conductivity of graphene at 1550 nm is plotted as a function of its chemical potential, shown in Figure 2.6, which indicates graphene has a negative imaginary part of the conductivity at 0.1 eV chemical potential. The imaginary part of the conductivity effects the polarisation-dependent absorption of 2D films [49]. When the imaginary part of its conductivity is negative, graphene (coated onto the surface of a fibre core) only absorbs light at the TM mode, does not affect the light propagation at the TE mode [8]. The refractive index and extinction coefficient of the graphene can also be calculated using Equation 2.34 and 2.35 at 0.1 eV chemical potential, as shown in Figure 2.7.

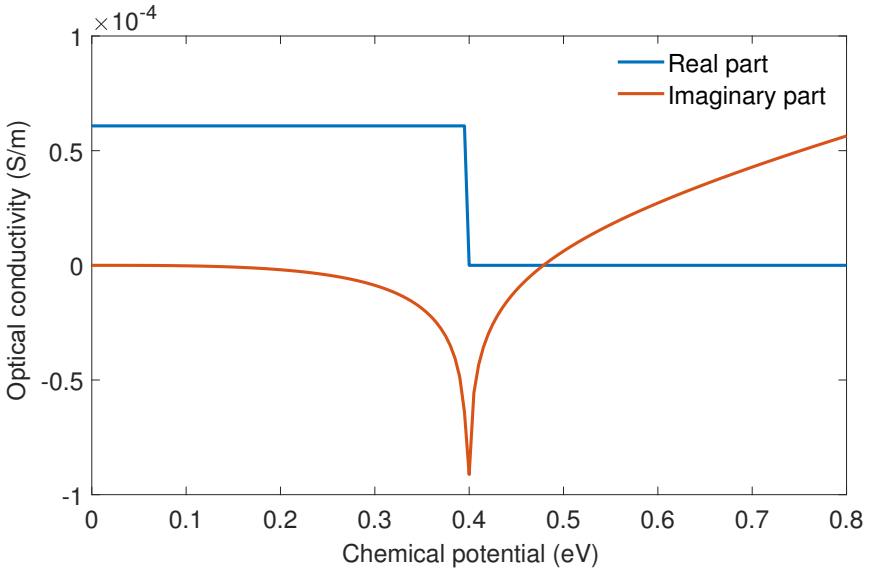

Figure 2.6: Conductivity of graphene at 1550 nm wavelength.

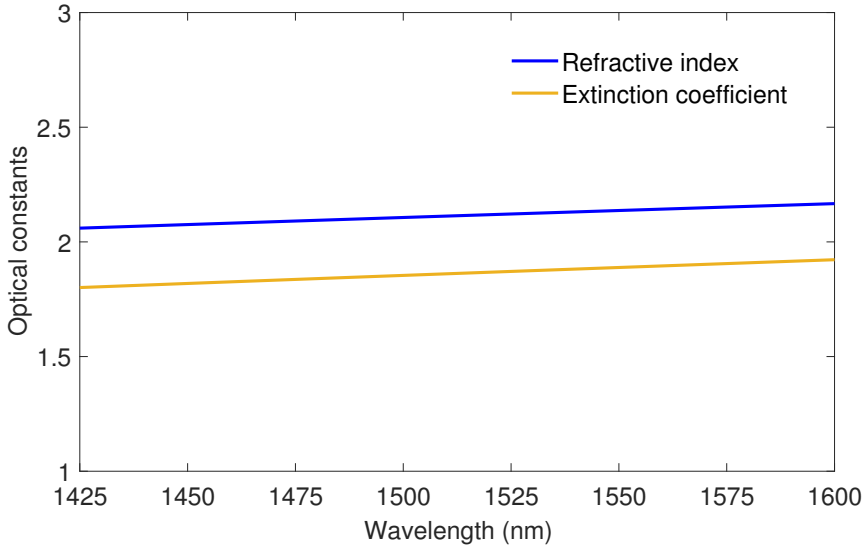

Figure 2.7: Refractive index and extinction coefficient of graphene at 0.1 eV chemical potential.

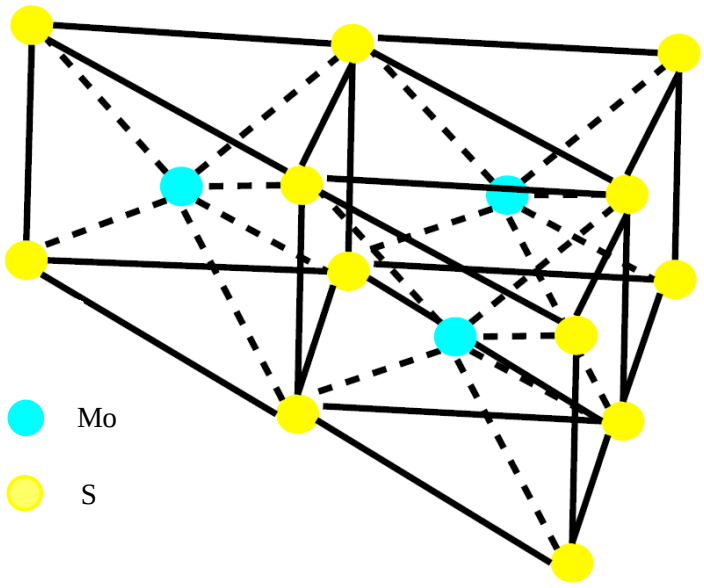

Figure 2.8: Lattice structure of MoS_2, consisting of two planes of S atoms and an intermediate plane of Mo atoms. Figures from Ref. [21].

2.3.2 Band Structure and Optical Absorption of MoS_2

The lattice structure of MoS_2 is shown in Figure 2.8. Unlike graphene, the structure consists of two hexagonal planes of S atoms and an intermediate hexagonal plane of Mo atoms [21]. Compared to graphene, a very important property of MoS_2 is that monolayer MoS_2 has a direct band gap, while bilayer and above have an indirect band gap. The schematic of direct and indirect band gap of MoS_2 is shown in Figure 2.9. The optical absorption of MoS_2 can be investigated by computing its complex permittivity, $\varepsilon(\omega) = \varepsilon_{real}(\omega) + i\varepsilon_{imag}(\omega)$, in which the imaginary part $\varepsilon_{imag}(\omega)$ indicates the optical absorption and can be written as [26]:

$$\begin{aligned}\varepsilon_{imag}(\omega) =& \frac{4\prod^2 e^2}{\Omega} \lim_{q\to 0} \frac{1}{q^2} \sum_{\rho,v,\vec{\kappa}} 2w_{\vec{\kappa}}\, \delta\left(\varepsilon_{\rho\vec{\kappa}} - \varepsilon_{v\vec{\kappa}} - \omega\right) \\ &\times \left\langle u_{\rho\,\vec{\kappa}+e_a\,\vec{q}} | u_{v\,\vec{\kappa}} \right\rangle \left\langle u_{\rho\,\vec{\kappa}+e_b\,\vec{q}} | u_{v\,\vec{\kappa}} \right\rangle^*,\end{aligned} \tag{2.36}$$

where ρ represents the conduction band states and v is the valence band states. $u_{\rho\,\vec{\kappa}}$ is the cell periodic part of the wavefunctions at κ point. $\varepsilon_{imag}(\omega)$ has two components ε_{zz} and $\frac{\varepsilon_{xx}+\varepsilon_{yy}}{2}$, corresponding to the polarisation of the electric field along and perpendicular to the hexagonal-system z-direction, respectively [26]. Then, the absorption coefficient of

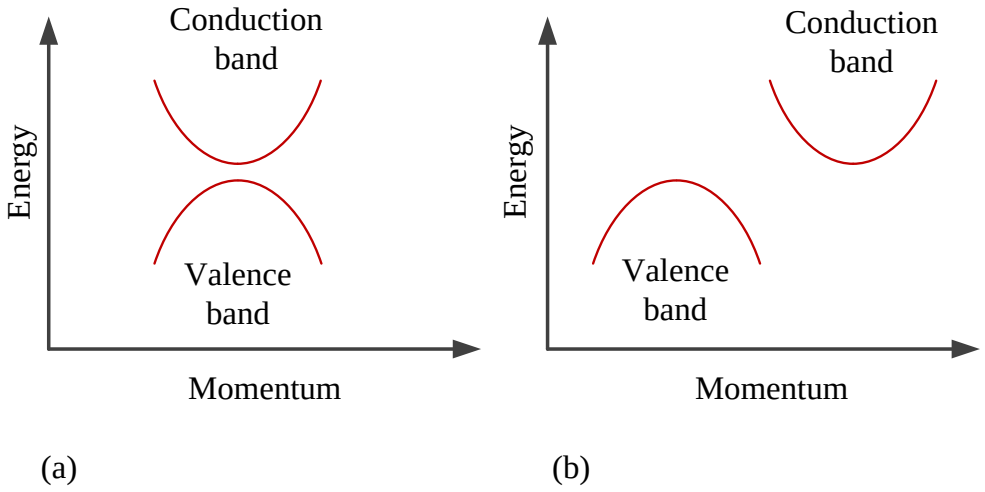

Figure 2.9: Schematic band structure of MoS_2 with direct band (a) and indirect band (b).

MoS_2 can be expressed as [26]:

$$\alpha = \frac{(\varepsilon_{xx} + \varepsilon_{yy})\omega}{2n(\omega)c}, \tag{2.37}$$

where $n(\omega)$ and c are the refractive index and the light velocity, respectively. The dynamic conductivity of MoS_2 can be calculated from its permittivity. Unlike graphene, MoS_2 has a positive imaginary part of the conductivity in the telecom region based on Ref. [50]. Thus, when coated onto the surface of a waveguide, MoS_2 only absorbs light at the TE mode, does not absorb the light at the TM mode [51], which is opposite to the feature of the graphene-based device [8]. This feature will be characterised in detail using optical experiments in Chapter 7.

2.3.3 Nonlinear Optical Properties of Graphene and MoS_2

The response of any dielectric to light becomes nonlinear for intense electromagnetic fields [52]. Since the origin of the nonlinear response is related to the motion of bound electrons under the influence of an applied field, the total polarisation $P(t)$ at time t induced by electric dipoles is non linear in the electric field $E(t)$ and can be expressed as [52]:

$$P(t) = \epsilon_0 \left(\chi^{(1)} \cdot E(t) + \chi^{(2)} : E^2(t) + \chi^{(3)} \vdots E^3(t) + \cdots\right), \tag{2.38}$$

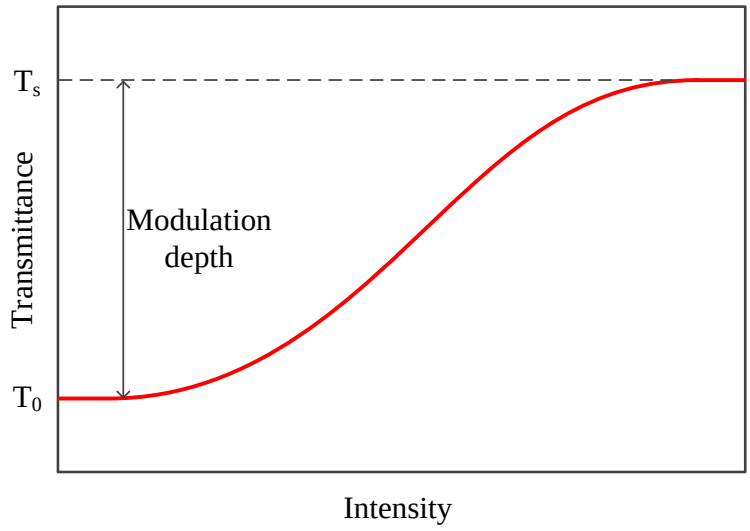

Figure 2.10: Schematic illustration of saturable absorption.

where ϵ_0 is the vacuum permittivity, $\chi^{(1)}$ is the linear susceptibility and $\chi^{(j)}$ is j^{th} order susceptibility. $\chi^{(2)}$ is the second order susceptibility and is responsible for nonlinear effects including second-harmonic generation, birefringent phase matching, and sum-frequency generation [52]. $\chi^{(3)}$ is the third order susceptibility including nonlinear effects such as, self-phase modulation, cross-phase modulation, four-wave mixing and saturable absorption [52]. The third order nonlinear susceptibility $\chi^{(3)}$ in graphene is 10^8 times larger than in insulating materials such as most glasses [53], while the nonlinear optical response of MoS_2 is even stronger than that of graphene [25]. Saturable absorption is a kind of nonlinear optical effect induced by the imaginary part of the complex third-order susceptibility $\chi^{(3)}$ [26]. The saturable absorption property of graphene and MoS_2 originates from its intensity-dependent absorption and the absorption coefficient α_{NL} can be written as [54]:

$$\alpha_{NL} = \frac{\alpha_s}{1 + I/I_s} + \alpha_{ns}, \tag{2.39}$$

where α_s is the saturable absorption coefficient, α_{ns} is the nonsaturable absorption coefficient, and I is the light intensity. I_s is the saturable light intensity, defined as the optical intensity required in a steady state to reduce the absorption to half of its maximum value [54]. Saturable absorption arises when electrons in lower energy states absorb the energy of photons and move to higher energy states. However, when the laser intensity is so strong that most of the higher electron energy states are occupied, absorption subsequently

saturates [54]. Saturable absorption causes a transmittance as shown in Figure 2.10, where there is lower transmittance at lower light intensities and higher at higher-intensity regions. The modulation depth Δ is defined as follows:

$$\Delta = \frac{T_S - T_0}{T_0}, \tag{2.40}$$

where T_s, T_0 are the maximum and minimum transmittance, respectively. Graphene and MoS_2 have been demonstrated to have excellent saturable absorption features due to their ultrafast response time, large modulation depth, and low saturation intensity [25, 54].

Chapter 3

Fabrication of Side-Polished Fibres

3.1 Introduction

The side-polished fibres are excellent platforms on which to exploit rich optical functionalities of 2D materials like graphene and MoS_2 for the development of optical devices. In this chapter, a fast, reliable, and affordable polishing method is described to fabricate side-polished fibres with low transmission loss that allows for strong evanescent field interaction. The polishing procedures, including polishing block design, choice of polishing particle size as well as characterisation of the surfaces and optical transmission measurements will be discussed in detail. The author designed and conducted all the polishing processes and the optical characterisations.

3.2 Design of Side-Polishing Blocks

There are several techniques for producing side-polished fibres, such as a wheel polishing method. A schematic setup for the wheel polishing is plotted in Figure 3.1. In this method, a fibre is stripped of its protective coating and suspended under slight tension over a rotating abrasive wheel [55]. Thus, this method doesn't need a block to hold the fibre during the polishing process [55, 56]. However, the polished fibre can be delicate and easily broken during the polishing process without a support block. Hence, most side polishing techniques require some sort of support block for the fibre [5,57]. A widely used quartz block design, shown in Figure 3.2(a), has a curved V-groove formed by acid etching. The fibre to be polished is fixed with epoxy into the groove of the quartz block and

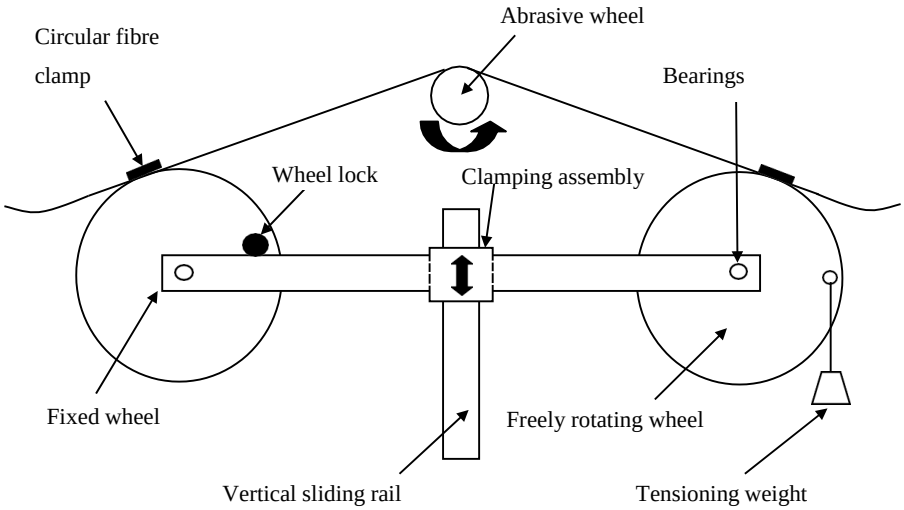

Figure 3.1: A schematic diagram of the bare fibre polishing method. (Reprinted from Ref. [55])

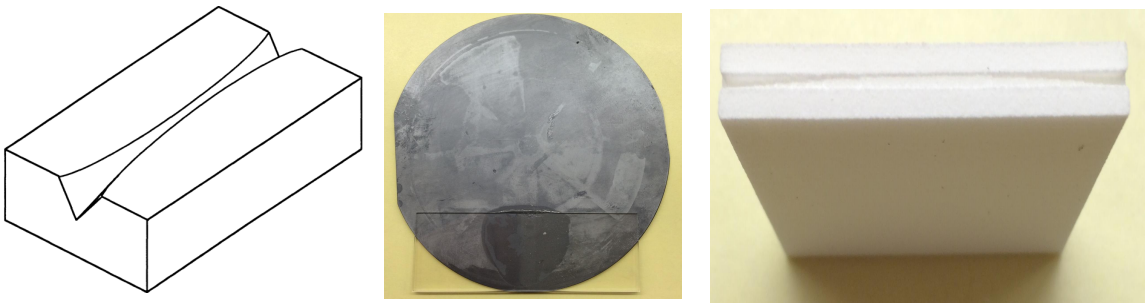

(a) (b) (c)

Figure 3.2: (a) Curved V-groove on a quartz block. (b) Hand-made wafer polishing block. (c) Nylon polishing block by 3D print.

polished as a unit in the same manner as the polishing of a conventional bulk-optic lens or prism [58]. Compared to bare fibre polishing, an advantage of this type of polishing is that the fibre is securely held in the block and it is easy to align and move the fibre relative to other surfaces. However, since the fibre and the quartz are polished as a unit, the amount of materials need to be removed is much larger than just polishing the fibre itself, and the quartz block can only be used once [58]. To find a fast, reliable, and affordable method to polish fibres, different block designs were explored in this work.

A hand-made wafer block, shown in Figure 3.2(b), was fabricated as an first attempt. The hand-made wafer block used glue to bond two glass slides and a wafer together to form a glass-wafer-glass sandwich structure. The sandwich structure forms a groove in

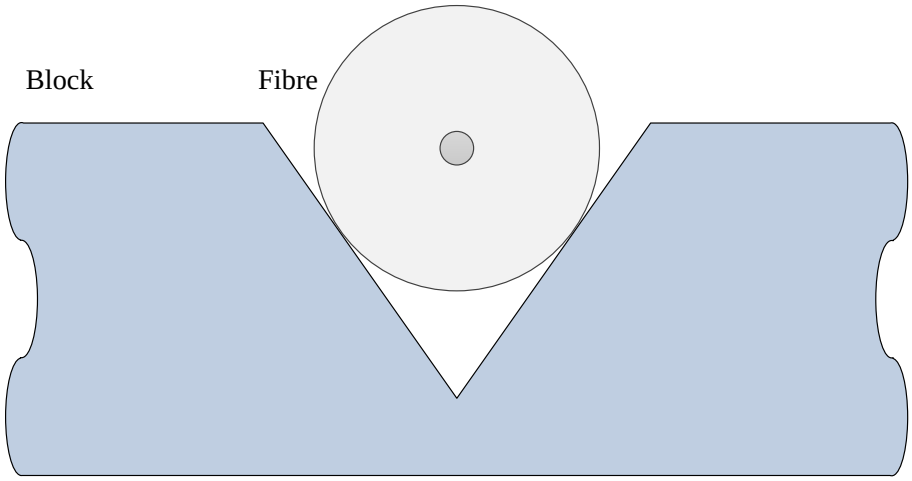

Figure 3.3: Cross-section of the V-groove and bonded fibre (not to scale).

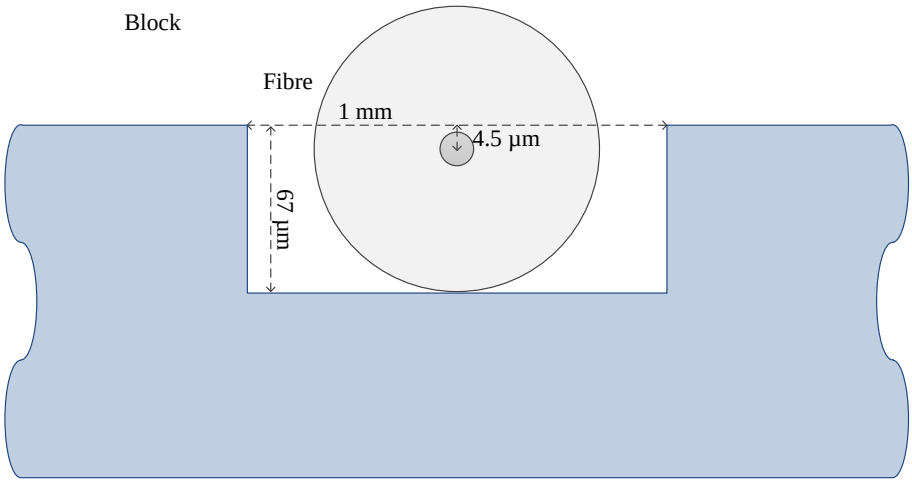

Figure 3.4: Cross-section of the U-groove and bonded fibre (not to scale).

the middle and a fibre was fixed in the groove during polishing. This block was easy to make and provided a well-defined radius, as well as a very smooth surface. However, the mechanical strength of the wafer and the glass slides combination was found to be not strong enough for the fibre polishing and the curve depth could not determined accurately. Then, 3D printing techniques were used to produce a nylon block with a curve on top, as shown in Figure 3.2(c). But the surface quality of the nylon block was found quite poor compared to the fibre polishing requirements, and nylon also had mechanical strength problems.

Aluminium was then considered to make the blocks, since it is easy to precision machine compared with silicon, glass or quartz. To give the best support during the fibre

polishing process, firstly, an aluminium block with a V-groove cut along the top of its cross-section, as shown in Figure 3.3, was designed. However, fabrication limitations made it very difficult to get a precise V-groove. To simplify the mechanical work, the V-groove was replaced with a U-groove, as shown in Figure 3.4. A high strength, resilient adhesive (Aremco Crystalbond 509) was used to bond the fibre in the U-groove. Since standard Corning SMF-28 step-index single-mode fibres with 125 μm diameter claddings are used for the fibre polishing, the U-groove depth was set to be 67 μm so that the polished surface was $\sim$ 4.5 μm away from the fibre centre, which is slightly larger than the fibre core radius (4.1 μm). Thus, when the polishing is complete, some residual cladding will be left, helping to reduce the transmission losses of the polished fibres, since the path of the propagating light remains untouched. Due to the fabrication limitations, the width of the U-groove was set to be 1 mm. The fibre didn't move during the polishing processes due to tightly bonding of the adhesive. The adiabatic transition principle [59] was used in the block design, which means the local mode varies slowly throughout the transition part so that all of the power remains in the fundamental mode. Thus, the depth of the U-groove end at both sides was set to be 400 μm to make sure the bending angle θ $\sim$2° to form an adiabatic transition from the full circular geometry of the fibre to the D-shaped uniform polished region, as shown in Figure 3.5. Also, this small bending angle prevents the fibre from breaking at the connecting points during the polishing processes. The fundamental mode propagates adiabatically through the transition part with minimal coupling to other modes, reducing the transition losses of the polished fibres. The centre polishing region and the two transition regions were set to be 1 cm long each to form a relatively long interaction region without breaking the adiabatic transition principle. A Solidworks design used for the block machining is shown in Figure 3.6.

3.3 Side-Polishing Processes

To start the fibre side-polishing, a 3 cm long section of the fibre was stripped of its buffer jacket and bonded into the U-groove of the aluminium block with adhesives, as shown in Figure 3.7. The crystalbond 509 was used as the adhesive due to its high viscosity (6000 cps) and its dissolution in acetone, which is particularly important for cleaning processes. The fibre polishing processes was composed of three steps: rough polishing, intermedi-

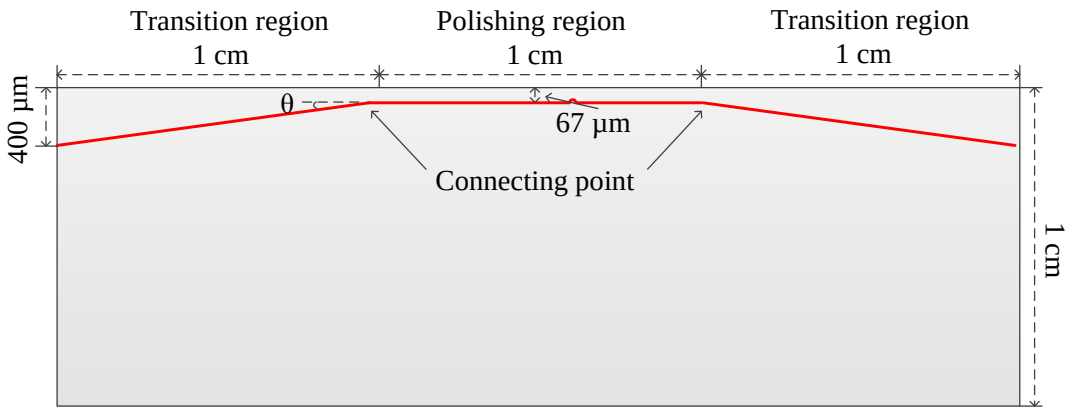

Figure 3.5: Side view of the U-groove block. Red line indicates the groove geometry.

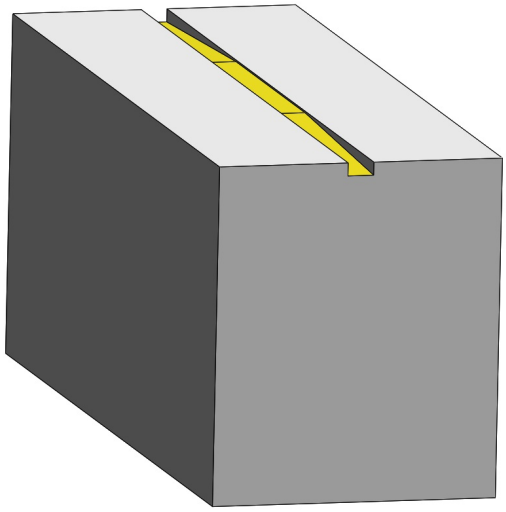

Figure 3.6: Solidworks design of the aluminium block.

ate polishing and fine polishing, using aluminium oxide polishing paper (UltraTec) with reducing abrasive particle sizes. The bulk of the top section of the fibre cladding was removed using polishing paper of 3 μm particle size at the rough polishing and 1 μm polishing paper at the intermediate polishing. The fine polishing step gave a smooth polished surface using a 0.3 μm polishing paper. After each polishing step, the fibre/block combinations were carefully cleaned with isopropanol and optical tissues to prevent large particles contaminating the next polishing step. Distilled water was also used to lubricate the aluminium oxide particles and reduce possible scratches.

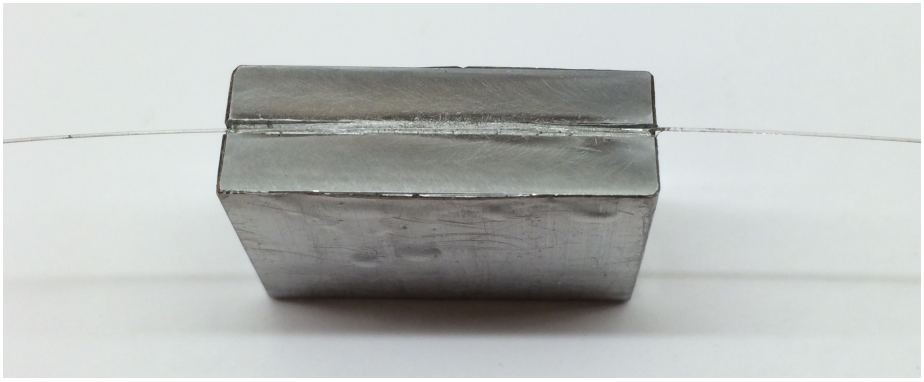

Figure 3.7: Aluminium polishing block and bonded fibre.

3.3.1 Brittle and Ductile Polishing

The process of fibre cladding removal by abrasive can be divided into two steps, a brittle grinding step and a ductile fine-polishing step, depending on the abrasive particle size [60]. The brittle grinding step happens when a sufficiently large abrasive particle size is used to have a large material removal rate, but the abrasive particles move and cut through the fibre leaving a series of pits and scratches. From optical examinations of the polished surface at the rough polishing stage, shown in Figure 3.8(a), grinding-induced pits and scratches are obvious when the 3 μm aluminium oxide film is used, indicating a brittle grinding step. For silica, ductile fine-polishing happens when the abrasive particle size is less than 1 μm [61]. Therefore, there is a sharp delineation between grinding and polishing that occurs at approx 1 μm particles [62]. In Figure 3.8(b), which shows an optical image of the polished surface after using 1 μm aluminium oxide paper, there are almost no pits left, indicating a ductile polishing step. But since the 1 μm is at the edge of the ductile step, both brittle grinding and ductile fine-polishing take place, so that there are still some scratches left. The final 0.3 μm aluminium oxide paper was used to remove almost all the scratches to get a fine polishing surface, shown in Figure 3.8(c). In this stage with the fine abrasive, only ductile deformation occurs, resulting in almost no scratches but also a very slow removal rate. Overall, polishing with coarser abrasives results in a higher material removal but also induces more surface and sub-surface damage, which has to be removed in the following polishing processes with finer abrasives [63]. My study shows that at least the last 5 μm of material must be removed using the 0.3 μm paper to ensure all brittle fracture pits and scratches are removed before getting to the required polishing depth.

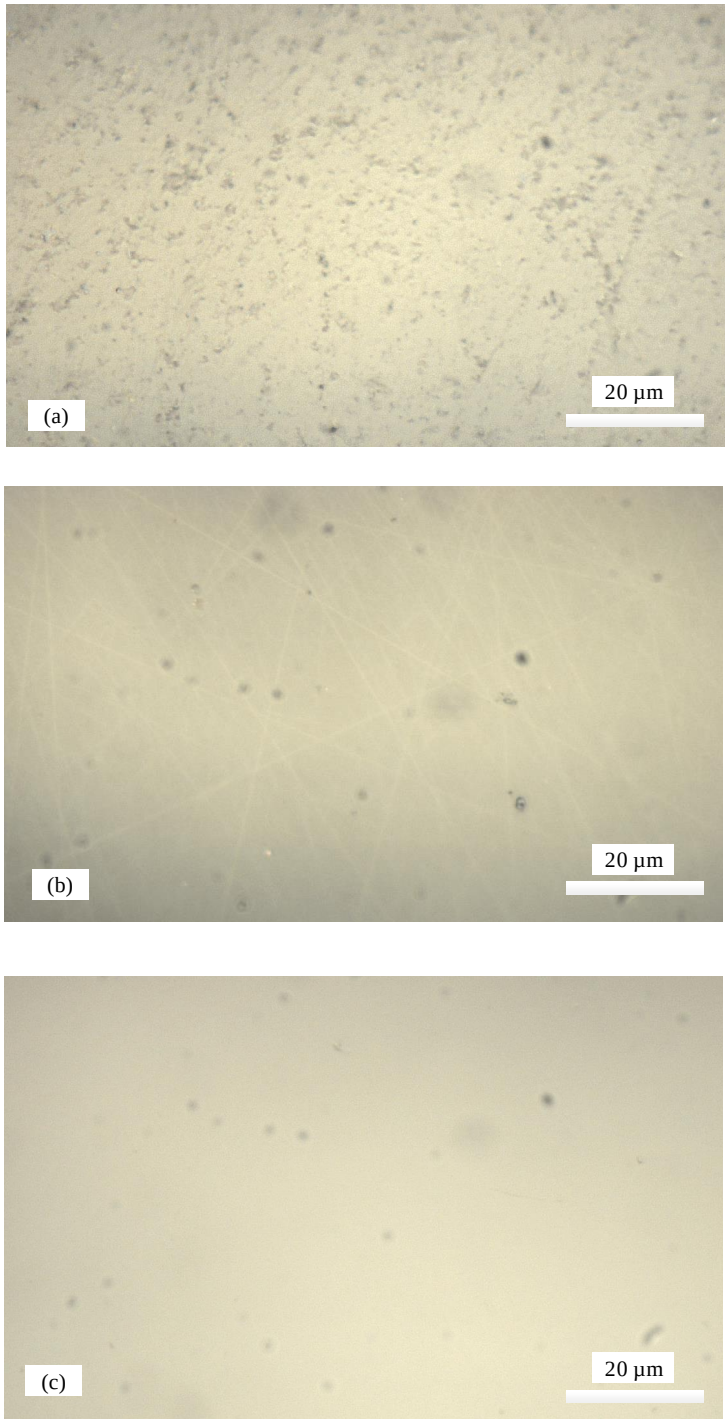

Figure 3.8: Optical microscopes of the polished surfaces, polished with (a) 3 μm aluminium oxide (lots of pits and scratches left), (b) 1 μm aluminium oxide (only scratches left), and (c) 0.3 μm aluminium oxide (almost no pits or scratches left). Black dots in (b) and (c) are from the microscope objective.

3.3.2 Determination of Polishing Depth

To reduce the possibility of polishing too much of the cladding, the polishing depth should be monitored. During the polishing processes, the width of the exposed optical fibre cladding ellipse, as shown in Figure 3.9, was checked regularly using an optical microscope. Then, the polishing depth d can be estimated using Equation 3.1 based on the ellipse width y and the radius r of the fibre.

$$d = r - x = r - \sqrt{r^2 - y^2/4}. \tag{3.1}$$

When the estimated polishing surface was close to the fibre core, an in-line measurement was used to check the potential evanescent field interaction strength. In the in-line measurement, laser light was launched into one end of the fibre and transmission of the light was monitored via a power meter at the other end. Then, a liquid (Cargille Labs 18091, 1.464 index at 589.3 nm) with its refractive index higher than the fibre cladding and core was dropped on the polished surface. As the polishing depth increases, more and more of the evanescent field of the guided-mode became accessible for the high-index liquid and escapes from the fibre core, resulting in a larger transmission loss. However, the in-line measurement method is only suitable for the final stage of the polishing processes since the transmission loss does not change much when the polishing surface is far from the core ($>$10 μm).

The target distance between the core and the final polished surface is chosen to permit access to more than 30 dB of the light propagating through the core. An optical image of a ready-polished fibre surface is shown in Figure 3.10. Since the ellipse width is 124.6 μm, the polishing depth can be calculated to be $\sim$57.5 μm using Equation 3.1. Thus, the cladding to core distance is estimated to be $\sim$1 μm. By using the in-line measurement, a transmission loss change of 30 dB was measured in this fibre, giving a potential interaction strength with an equivalent value, meaning the target cladding to core distance is around 1 μm.

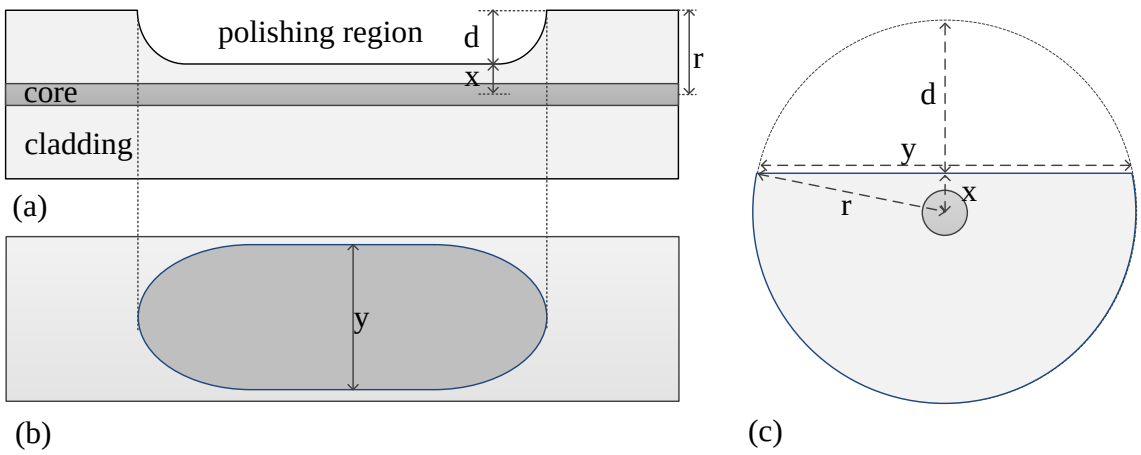

Figure 3.9: Side-polished fibre schematic: (a) side view, (b) top view, and (c) cross section.

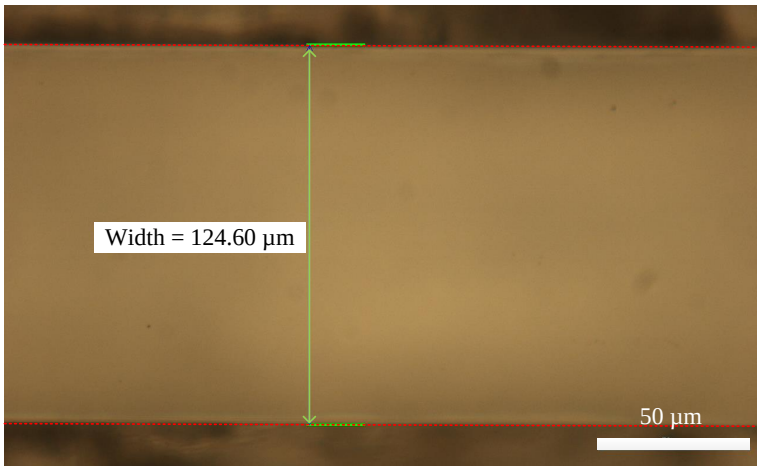

Figure 3.10: Polished surface width measured by a microscope.

3.4 Characterisation of Polished Surfaces

The quality of the polished surface is critical since surface abnormalities such as scratches scatter light from the fibre, which will increase the transmission losses. Figure 3.11(a) shows a fibre with scratches on its polishing surface, and scattering losses occur when a red light was launched into the fibre, as shown in Figure 3.11(b). To quantify the surface quality of the polished fibres, an interference microscope (ZEMETRICS ZeScope) was used to measure the surface roughness of the polished region. Interference microscopy relies on the phenomenon of interference fringe generation following amplitude division and recombination of light from a white light source [64, 65]. It is a commonly used tool in semiconductor and microelectronics manufacturing, where it affords nanometer

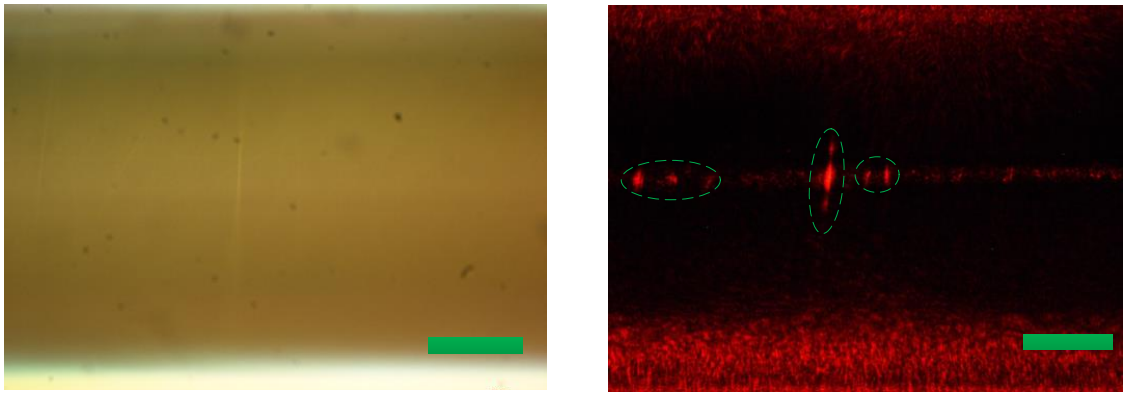

(a) (b)

Figure 3.11: Optical images of the polished fibre surface (a) before and (b) after launching a red light source, to illustrate the scattering losses caused by scratches (indicated by green dashed lines). Scale bars: 20 μm.

Measurement area	1	2	3	4	5	6	average
1^{st} fibre roughness average(nm)	8.1144	6.4835	6.8660	6.5600	6.6241	6.4379	6.8476
2^{nd} fibre roughness average(nm)	11.5845	11.4916	11.5254	11.451	11.1236	11.4580	11.4390

Table 3.1: Surface measurements at different areas of two side-polished fibres.

dimensional precision in height measurement, over wide fields of view [66]. The measurement results of two polished fibres are shown in Figure 3.12 and Table 3.1, confirming the nanometre-level roughness of polished fibre surface. Scanning electron micrography (SEM) was also used to check the surface roughness. SEM is a type of electron microscope, which is capable of imaging sub-nanometer features of a sample by scanning the surface with a focused beam of electrons [67]. Figure 3.13 shows the SEM images at different regions of the polished fibre, further confirming its ultra-smooth surface.

3.4.1 Surface Flatness

To check the surface flatness, a characterisation was undertaken by applying an experimental setup shown in Figure 3.14. A green laser light (532 nm) was passed through an iris diaphragm and focused on the polished region by a microscope objective lens. The

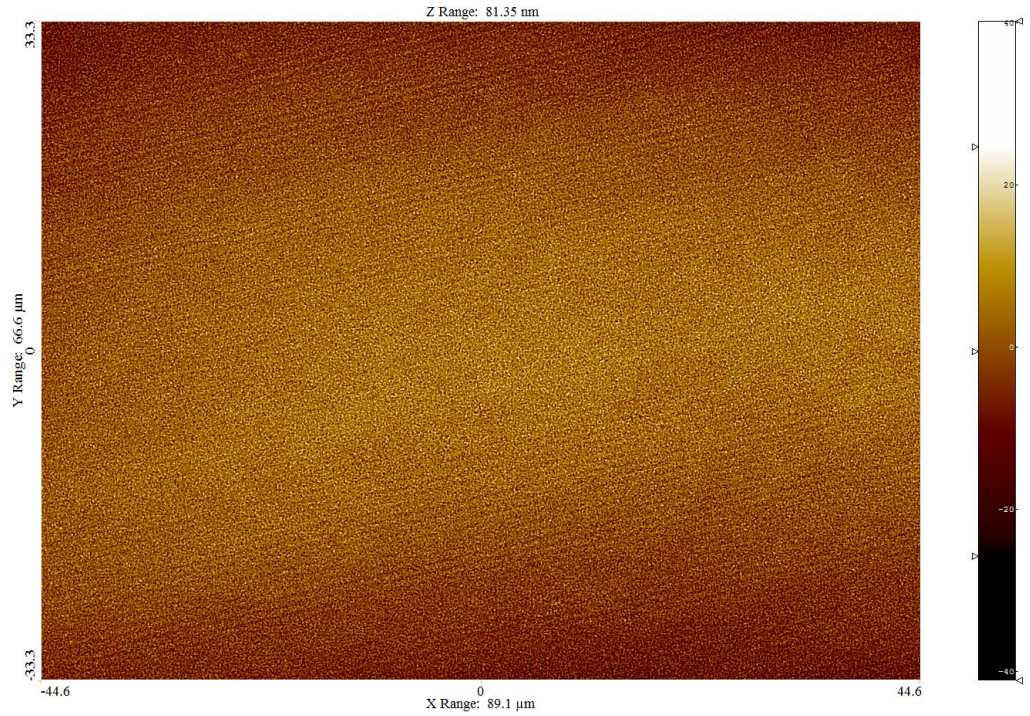

(a)

(b)

Figure 3.12: ZeScope images of the polished surfaces. (a) Measurement area 4 from the first fibre and (b) measurement area 6 from the second fibre, corresponding to Table 3.1.

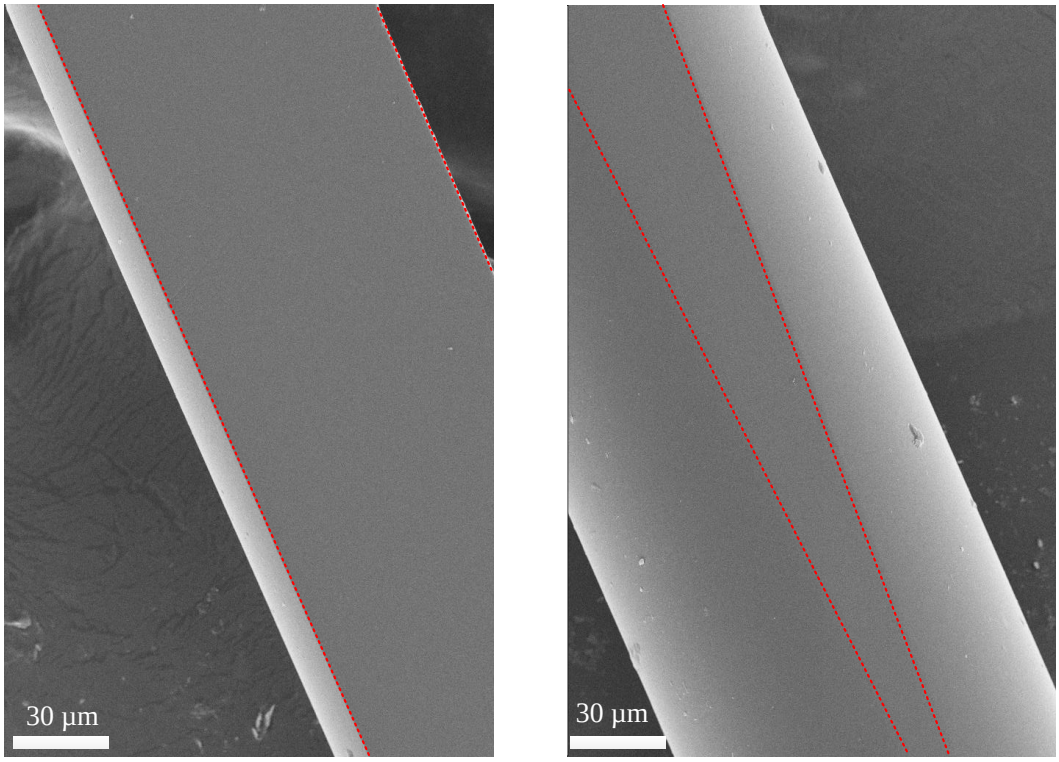

(a) (b)

Figure 3.13: SEM images of the polished fibre, showing ultra-smooth polished surface. (a) Uniform polished region. (b) Transition region. The polished areas are indicated by red dash lines.

reflection of the green light should follow the same path of the incident beam if the surface is flat. If there is any tilt in the surface, the reflected light will not overlap precisely with the incident beam path and will be blocked by the iris diaphragm. In the experiment, the distance X between the input spot centre and the reflection spot centre at the iris diaphragm was found to be less than 1 mm. Since the magnification of the microscope objective is 20 times, the maximum tilt angle θ of the surface was calculated to be only 0.7° using Equation 3.2, where $Y = 4$ mm is the working distance of the microscope objective.

$$\theta = arctan\frac{X}{20\,Y}. \tag{3.2}$$

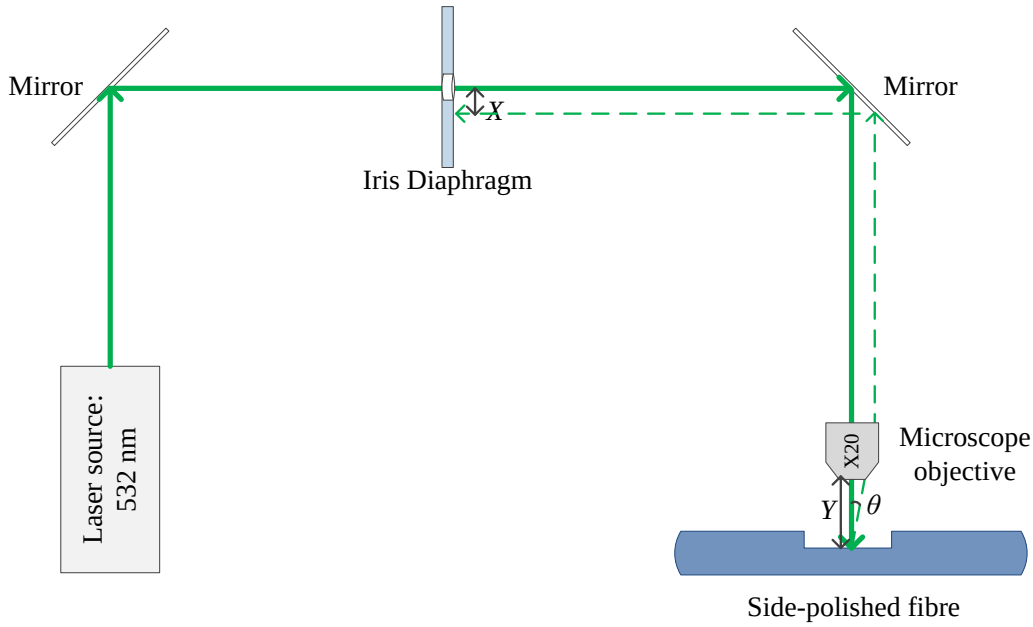

Figure 3.14: Experiment set-up to check the surface flatness of polished regions (solid green line: incident light, dashed green line: reflection light). Working distance $Y = 4$ mm

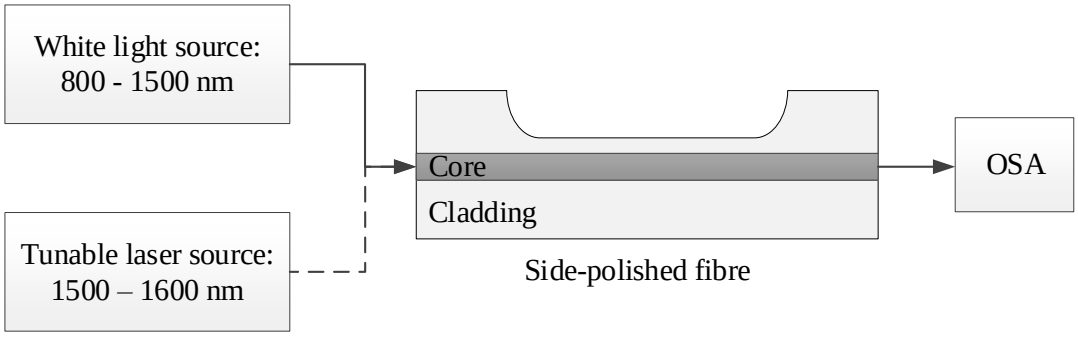

Figure 3.15: Experiment set-up to check the optical transmission of side-polished fibres.

3.5 Optical Characterisation

To characterise the optical transmission of the side-polished fibres, an experimental setup shown in Figure 3.15 was utilised. Firstly, a white light source (800 - 1500 nm) was used as the input source to check the spectral response of the transmission loss affected by the index matching liquid. The optical spectrum of the output light were detected by an optical spectrum analyser (OSA). Figure 3.16 shows the transmission loss spectrum with and without the high index matching liquid from 800 nm to 1500 nm. The top red line in Figure 3.16 shows that the loss of the side-polished fibre is around 0.5 dB across most of the wavelength region, confirming the ultra-low loss feature of the fibre. When adding the index matching liquid, the loss dramatically increases to more than 20 dB across the full wavelength range, indicating the potential for broadband, high-strength light-matter interactions. Furthermore, the loss increase is much larger at long wavelengths (1200 - 1500 nm) than at short wavelengths (800 - 1200 nm). This is believed to be due to the tighter mode confinement for the shorter wavelengths. The same experiment was also undertaken to check the transmission loss at a longer wavelength range using a tunable laser (Yenista Tunics, 1500 - 1600 nm). Figure 3.17 shows that, from 1500 nm to 1600 nm, the transmission loss is still around 0.5 dB without index matching liquid and will increases to more than 30 dB at all wavelength range with index matching liquid dropped onto the polished region. These experimental results show that the resulting polished fibres have negligible transmission loss across a very broad wavelength range (from 800 nm to 1600 nm), though it is possible to access most of the core guided light through their exposed surface. By using the same tunable laser, an experiment was also performed on the bare side-polished fibre to determine the extent of the polarising effect of the D-shaped structure. As shown in Figure 3.18, when polished to a distance of 1 μm from the core, the transmission loss of the bare fibre has less than 0.2 dB difference between the TE and TM modes.

3.6 Conclusion

A single-mode optical fibre mounted in a block was side-polished to create a planar platform that allows access to the evanescent field escaping from the fibre core. After trying different blocks, an aluminium block with a U-groove was chosen for use due to me-

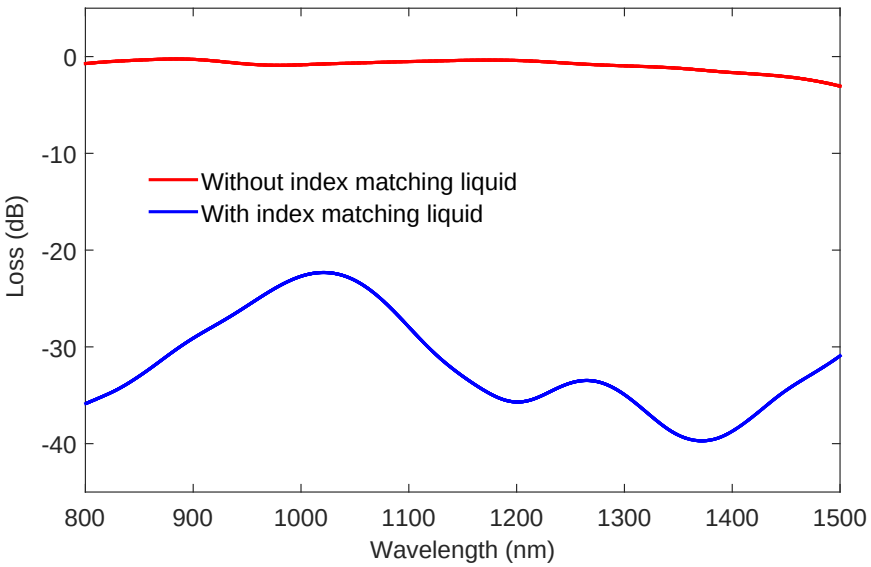

Figure 3.16: Spectral response of the transmission loss between 800 nm and 1500 nm with and without index matching liquid using a white light source.

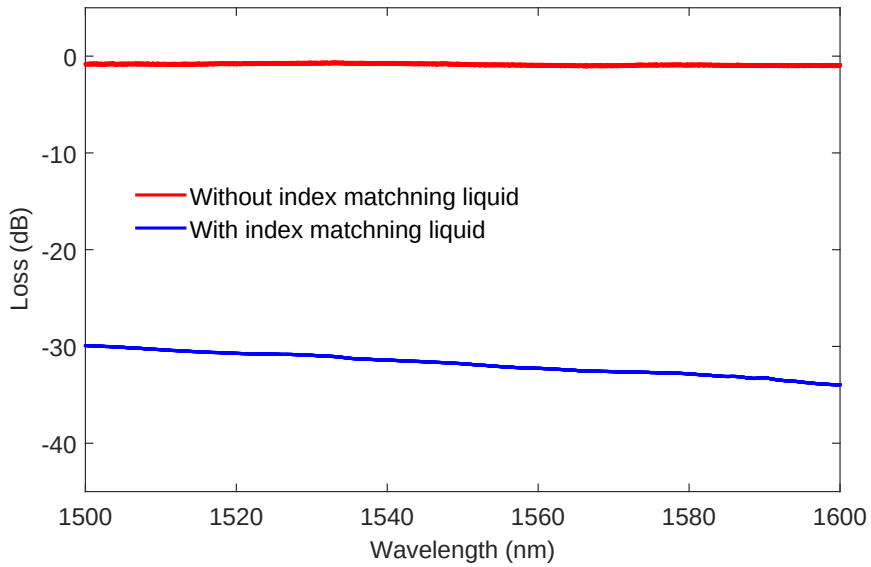

Figure 3.17: Spectral response of the transmission loss between 1500 nm and 1600 nm with and without index matching liquid using a tunable laser source.

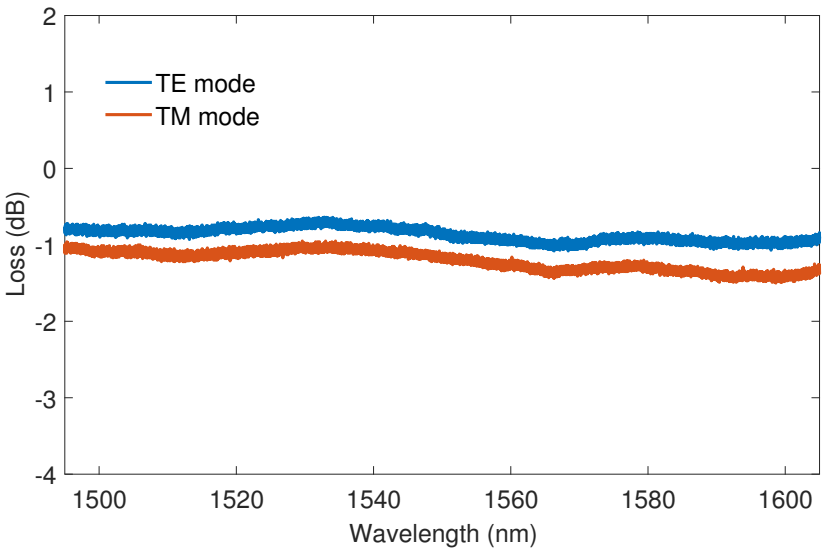

Figure 3.18: Transmission loss of a bare side-polished fibre at different polarisation states of input light.

chanical availability. Characterisation shows that the polishing surface is ultra-smooth and flat. Due to the unbroken propagating path and the adiabatic transition design, the fibre has a very low transmission loss across a broadband wavelength range, which was proven by optical measurement results. The fibre transmission changes significantly when dropping index-matching liquid on the polished surface, showing its potential for strong light-matter interactions. Also, by simply changing the polishing block design to vary the polished fibres, optical devices based on this platform may have many key benefits such as controllable interaction lengths and interaction strengths.

Chapter 4

Optical Device Fabrication based on 2D Materials and Side-Polished Fibres

4.1 Introduction

Chapter 3 describes a method for producing side-polished fibres which allows strong evanescent field interaction while maintaining ultra-low transmission loss. This chapter will discuss the fabrication of integrated optical devices based on 2D materials and the polished fibre platform, including growth and characterisation of graphene and MoS_2, as well as transferring these 2D materials onto the side-polished fibres. A schematic representation of the integrated fibre device is illustrated in Figure 4.1, where the device is formed by transferring polymer-coated 2D materials onto the side-polished fibre windows. The polymer overlayer was used to enhance the light-material interaction, which will be discussed in detail in Chapter 5. Characterisation of the 2D materials will be also discussed in this chapter as these properties are very important to the performance of the optical fibre devices, including the number of layers, crystal structure, and the density of defects in the material. The growth and characterisation of 2D materials was developed and performed by Dr. Chung Che Huang. The 2D material transfer method was mainly developed by Dr. Chung Che Huang. The author undertaken all the fabrication processes and optimised the MoS_2 transfer method.

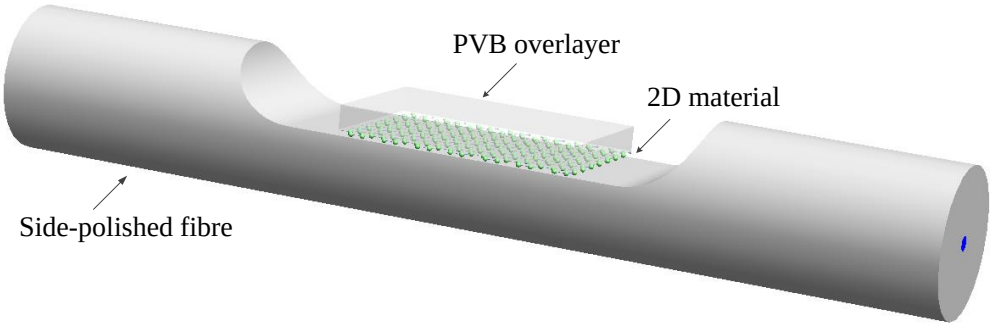

Figure 4.1: Schematic illustration of the 2D material-fibre sandwich structure.

4.2 Growth of 2D Materials

4.2.1 CVD Method

Monolayer or few-layer 2D materials with high quality are essential for efficient device performance. Several methods exist for the growth of 2D materials, such as micromechanical exfoliation, hydrothermal synthesis, electrochemical synthesis, and CVD methods [19, 68–70]. Due to the fact that it is cheap, efficient, and scalable, the CVD method was used for graphene and MoS_2 growth in this work [71]. CVD involves flowing a precursor gas or gases into a chamber containing a substrate to be coated [72]. Then, a thin film is deposited on the surface of the substrate via a chemical reaction [72]. CVD has been widely used to grow or deposit thin films, amorphous or crystalline, from solid, liquid or gaseous precursors of many materials [73]. Most importantly, using the CVD method, it is possible to get long lengths ($\sim$1 cm) of 2D materials with same thickness, which are required for the device fabrication in this work.

4.2.2 Graphene Growth

A schematic of the CVD system used for the fabrication of graphene is shown in Figure 4.2 [70]. The substrate used for the graphene fabrication was copper (Cu) foil (99.8% purity from Alfa Aesar). Before growing the graphene, a 25 μm thick Cu foil substrate was cleaned with acetone, isopropanol and then by acetic acid to remove the native oxide. The cleaned Cu foil was dried with nitrogen gas and then loaded into the CVD system. The CVD reaction chamber (50 mm OD quartz tube) was evacuated to 2 mBar, and then backfilled to ambient pressure with 6% H_2/Ar gas. After that, the temperature was increased

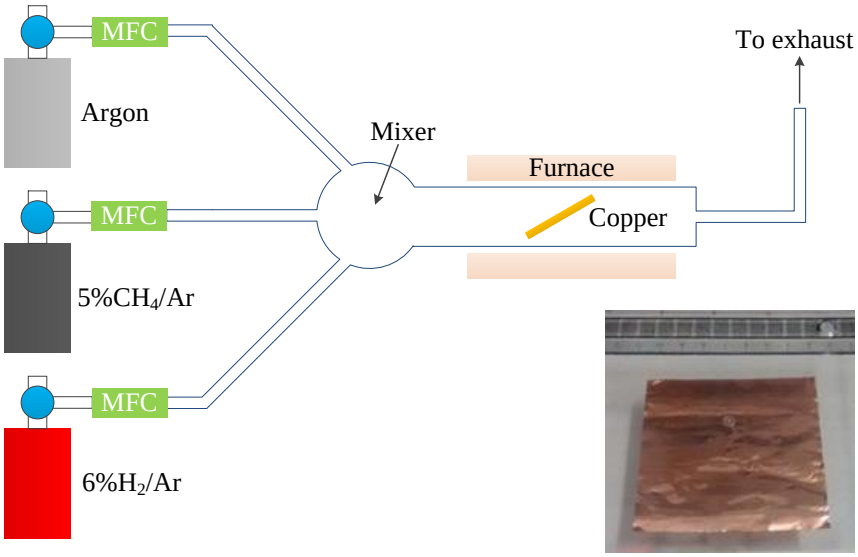

Figure 4.2: Experimental configuration of the CVD method to grow the graphene film (MFC: mass flow controller). Inset: an image of CVD-grown graphene on a Cu foil with a size of 80 mm $\times$ 90 mm.

to 1000 °C with H_2/Ar gas flow of 100 sccm and the chamber pressure maintained at 20 mBar. The Cu foil was annealed at these conditions for 30 min. The graphene growth was performed by flowing 5% CH_4/Ar at 100 sccm together with H_2/Ar at 210 sccm for 20 min. Finally, the CH_4/Ar flow was turned off to finish the graphene deposition and the Cu foil was cooled down naturally.

4.2.3 MoS_2 Growth

The CVD method was also used for growth of the MoS_2 films. Firstly, a 280 nm thick SiO_2 film was deposited onto a Si sample to be used as the MoS_2 growth substrate. A schematic of the CVD configuration for the MoS_2 growth is shown in Figure 4.3. The deposition process is described in detail in Ref [70]. Briefly, a $MoCl_5$ precursor, with a purity of 99.6% (Alfa Aesar), was kept at room temperature, and $MoCl_5$ vapour was delivered by an argon carrier gas through a mass flow controller (MFC) to the quartz CVD reaction tube. The reactive gas, H_2S, generated in situ by the reaction of 18% HCl and FeS (99% pure from Strem), was delivered through a second MFC. The H_2S-argon mixed gases were purified by passing through an in-line dryer before entering the CVD reactor. The argon gas flow rates for delivering the $MoCl_5$ precursor and the H_2S gas were typically set at 100 sccm and 200 sccm, respectively, corresponding to a deposition rate for the MoS thin

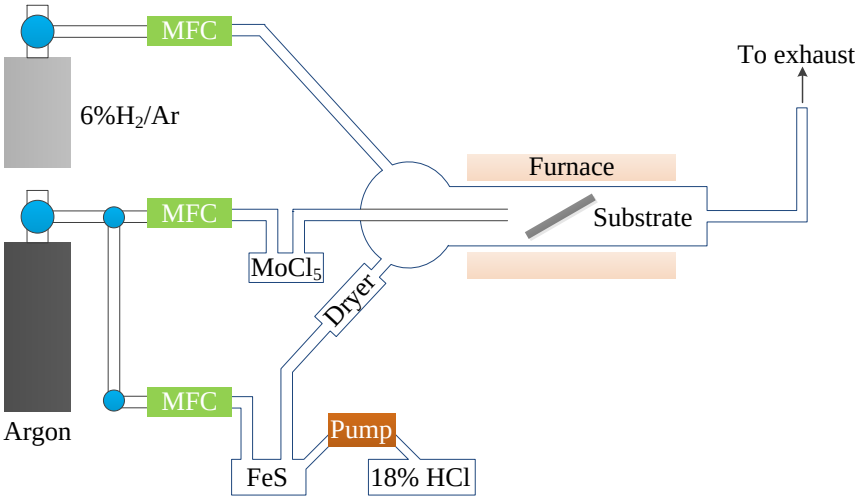

Figure 4.3: CVD configuration for MoS_2 growth (MFC: mass flow controller). [70]

film of 0.2 nm min^{-1}. When the desirable MoS_2 thickness was achieved, the same cooling process was performed after turning off the gas flows.

4.3 Characterisation of 2D Materials

4.3.1 Raman Spectroscopy

Raman spectroscopy has played an important role in the characterization of 2D materials and has become a powerful tool for understanding their structures [74–76]. It has plenty of advantages as it is fast, accurate, reliable, non-destructure and does not require direct-contact. Raman spectroscopy is the inelastic scattering of light, associated with the emission or absorption of phonons [77]. The technique involves launching a laser beam onto a sample and detecting the scattered light. Most of the scattered light has the same frequency as the laser source, which is called Rayleigh scattering [78]. A very small amount of the scattered light is shifted in energy from the laser frequency due to interactions between the incident light and the vibrational energy levels of the molecules in the sample, which is called Raman scattering [78]. By knowing the energy shift of the scattered light relative to the incident light, the Raman spectrum can be obtained in wave-numbers (cm^{-1}), which is useful for the identification and quantization of an unknown material [79]. Specifically, Raman frequencies give information about the composition of unknown materials;

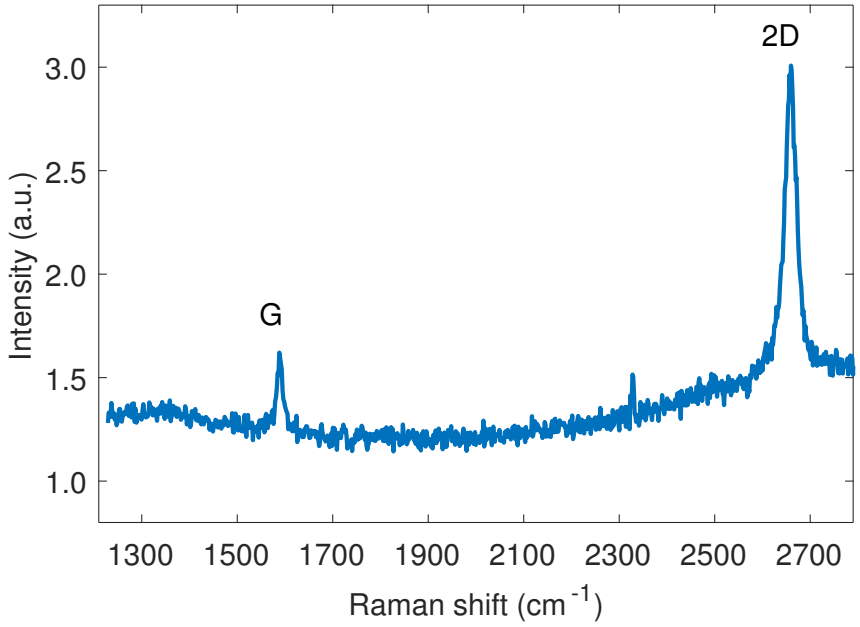

Figure 4.4: Raman spectrum of a typical graphene sheet, with 2D:G ratio of 4:1 and a 2D peak FWHM of 25 cm^{-1}.

the width of the Raman peaks gives information about the quality of the material, such as the amount of deformation; and the intensity of the Raman peaks provides an indication of the amount of material, such as the layer thickness [78].

4.3.2 Graphene Characterisation

A typical CVD-grown graphene film used in this work has an dimension of 80 mm $\times$ 90 mm, as shown in Figure 4.2 inset. In our work, a Renishaw Raman microscope equipped with a charge-coupled device (CCD) camera and a 633 nm laser was used to characterise the Raman spectra of the 2D material films. The laser beam has a spot size of $\sim$1 μm on the sample. For the graphene film, the Raman spectrum was measured from 1250 cm^{-1} to 2850 cm^{-1} with a resolution of 0.1 cm^{-1}, as shown in Figure 4.4. The Raman features of mono-layer graphene are the G peak at $\sim$1580 cm^{-1} and a symmetric 2D peak at $\sim$2700 cm^{-1}, which has full-width at half maximum (FWHM) of $\sim$25 cm^{-1}. The negligible D peak, normally seen in the spectrum near $\sim$1350 cm^{-1}, indicates that high quality (i.e., low defect level) graphene has been produced. Because the appearance of the D peak indicates disorder in the carbon lattice, such as the presence of domain boundaries, lattice defects or distortion [80]. In addition to the width of the 2D peak, it is also known that

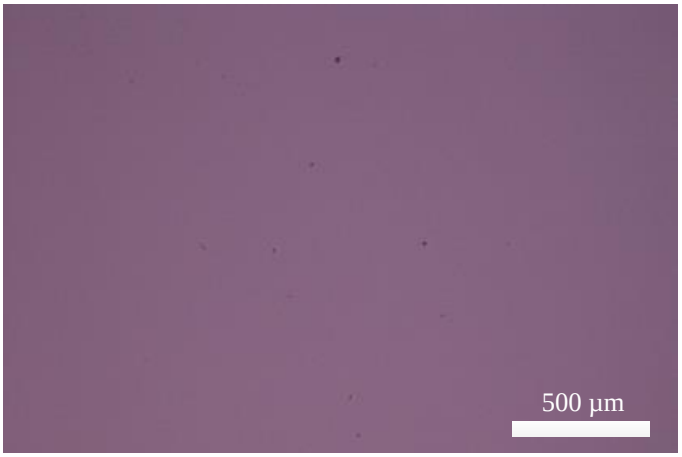

Figure 4.5: Optical microscope image of a typical MoS_2 sample growing on a SiO_2/Si substrate. The MoS_2 layer covers the entire image.

the ratio of the intensities of the 2D and G peak (I^{2D}/I^G) can be used to determine the number of graphene layers. The typical I^{2D}/I^G ratio for single layer and bilayer exfoliated graphene are 2-3 and slightly less than 1, respectively. For the CVD-grown graphene film used in this work, the I^{2D}/I^G has a ratio greater than 4, which indicates that a high-quality mono-layer graphene film has been produced on the Cu foil substrate.

4.3.3 MoS_2 Characterisation

Figure 4.5 presents an optical microscope image of the CVD-grown MoS_2 on a SiO_2/Si substrate, showing a large continuous MoS_2 film which covers the entire image. To further check the MoS_2 sheet, Raman spectroscopy was also undertaken. Like graphene, single-layer and few-layer MoS_2 exhibit different Raman spectra. The Raman spectrum of bulk MoS_2 has two prominent peaks: an in-plane (E_{2g}) mode located around 383 cm^{-1} and an out-of-plane (A_{1g}) mode located at 408 cm^{-1} [81]. The in-plane mode results from the vibration of the two S atoms with respect to the Mo atom, while the out-of-plane mode is associated with the S atoms vibrating out-of-plane [82]. By using the same Raman microscope as in Section 4.3.2, the Raman spectrum of the MoS_2 film was measured from 280 cm^{-1} to 520 cm^{-1} with a resolution of 0.1 cm^{-1}, shown in Figure 4.6. The 382 cm^{-1} E_{2g} in-plane mode and 407 cm^{-1} A_{1g} out-of-plane mode indicates this is a bulk MoS_2 film. Additional characterization was conducted to determine the thickness of the MoS_2 more accurately. Before taking SEM images, the sample was coated with a $\sim$200

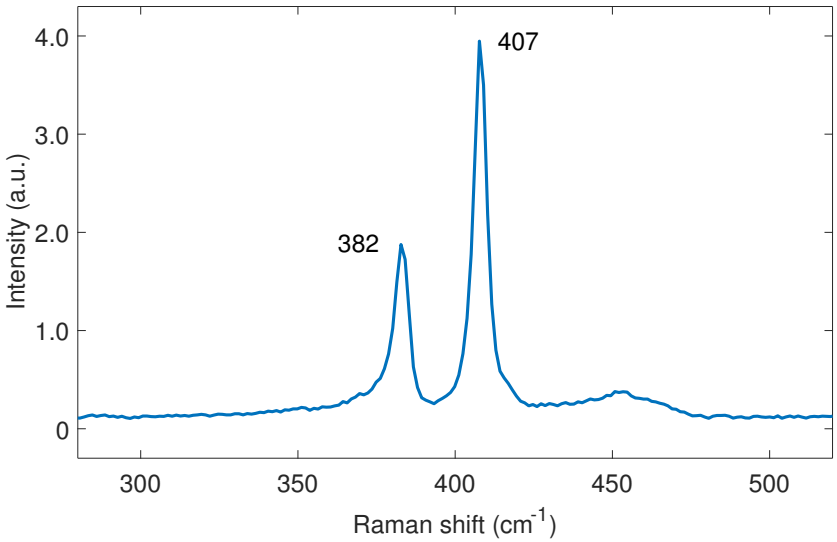

Figure 4.6: Raman spectrum of a typical MoS_2 sheet

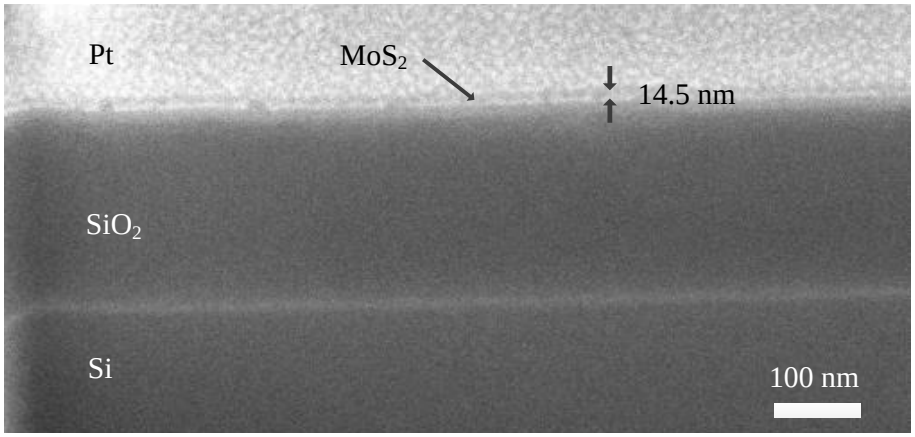

Figure 4.7: SEM image of the MoS_2 layer to verify its thickness.

nm thick Pt layer and milled using a focused ion beam (Helios NanoLab 600). Figure 4.7 depicts a SEM image of the cross-section in the striking area. The SEM image reveals that a 14.5 nm MoS_2 thin film has been uniformly deposited on the substrate. Considering the thickness of a monolayer of MoS_2 is 0.6 nm $\sim$ 0.7 nm [83], the layer number of the MoS_2 used in this work is determined to be $\sim$21. The optical constants of the MoS_2 layer among near-infrared region were not as well studied as these of graphene. Thus, a spectroscopic ellipsometry method [84] was used to characterise the wavelength dependent refractive index and extinction coefficient of the MoS_2 layer used in this work by Dr Ioannis Zeimpekis, as shown in Figure 4.8. In the spectroscopic ellipsometry method, the optical constants was determined by analysing the change in the polarisation state of the

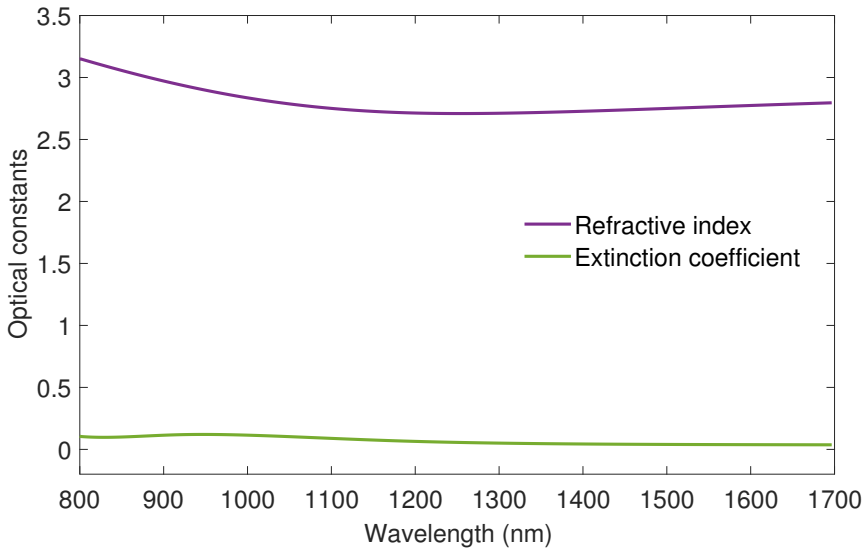

Figure 4.8: Refractive index and extinction coefficient of the MoS_2 layer used in this work.

reflected light from the layer surface and developing an optical dispersion model of the layer [84].

4.4 Graphene-based Device Fabrication

4.4.1 PVB Coating

Before fabricating any graphene-based devices, the Cu substrate must be removed. Thus, it is necessary to transfer the graphene onto an alternative substrate for handling. Although a variety of methods exist [85], [86], so far the polymer-based transfer technique [87] is most widely used as it is simple and reliable. In this approach, the polymer acts as a temporary rigid support during etching of the metal to prevent folding or tearing of the graphene [87]. In this work, polyvinyl butyral (PVB) is used as the supporting and protective layer. PVB is a non-toxic, odourless, and environmentally friendly polymer, which has been widely used in applications that require strong binding, optical clarity, adhesion to different surfaces [88]. PVB is also well suited for integration with the silica fibres as it has a low optical loss over most of the broad transmission window of silica fibres. PVB also serves to increase the light-graphene interaction, which will be explained in more detail in Chapter 5. The simulations in Chapter 5 also show that a value of around 1 μm is an ideal thickness for the PVB layer. A KLA Tencor P-16 stylus profiler was used

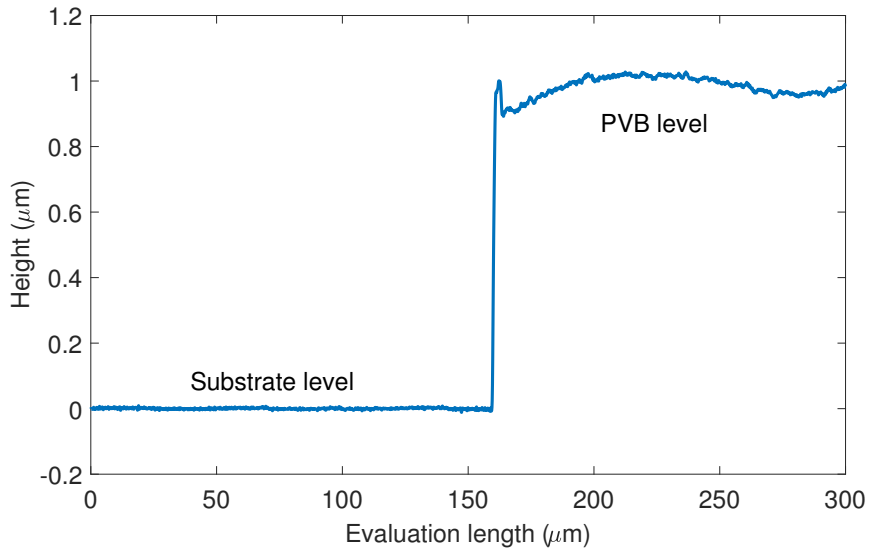

Figure 4.9: Thickness evaluation of the PVB film using a stylus profiler.

to check the PVB layer thickness. After trying different PVB concentrations, 5% PVB in ethanol solution was found to give a film with its thickness most close to the 1 μm. As shown in Figure 4.9, the thickness of the PVB used in this work is around the optimum 1 μm. After dropping the resist onto the graphene sheet, the spin coater rotated initially at 500 rpm for 10 seconds to diffuse the resist over the entire graphene surface and then at 3000 rpm for 50 seconds to form a layer around 1 μm thickness. After spin coating the PVB layer, the sample was baked on a hotplate at 85 °C for 5 minutes to improve adhesion between the graphene film and the PVB layer.

4.4.2 Cu Removal

Since graphene is grown on both sides of the Cu foil during the CVD, plasma etching was used after coating the PVB layer to remove the backside graphene and to expose the Cu surface. During the plasma etching, the backside of the Cu foil was placed upward and put into a plasma chamber (OPT Plasmalab 80) for 2 minutes at oxygen atmosphere with 100 W operation power. After the oxygen plasma treatment, the Cu substrate was etched away in an ammonium persulfate solution, leaving only the PVB-coated graphene sheet. Compared to commonly used iron chloride, ammonium persulfate has a much higher etching rate and leaves less residual metal particles. A 2 cm^2 in area and 25 μm thick Cu foil could be etched within an hour using ammonium persulfate solution, while more than 4 hours were needed for iron chloride.

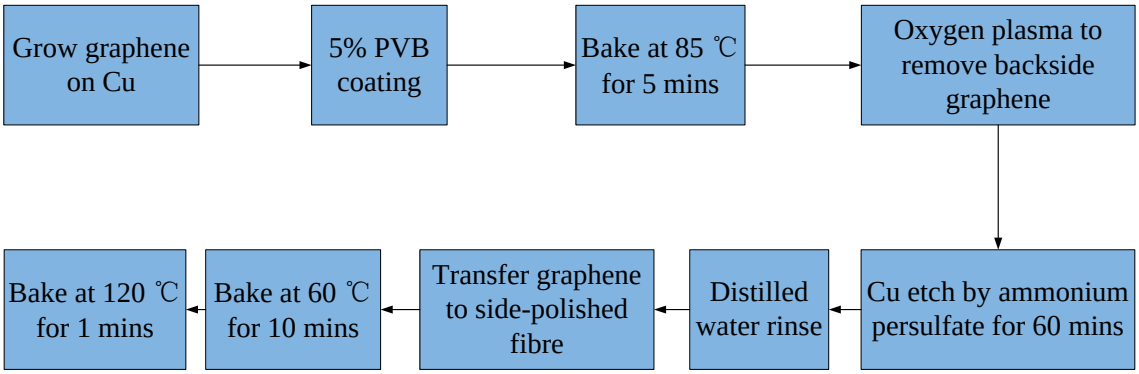

Figure 4.10: Graphene transfer process flow including: CVD-growth, PVB-coating, Plasma etching, substrate dissolving, distilled water rinse and finally graphene transferring.

4.4.3 Graphene Transfer

After the substrate has been dissolved, the PVB-coated graphene sheet was rinsed in distilled water and floated on the water surface. The fibre was then immersed into the water and lifted under the floating graphene film to transfer it onto the planar polished surface. Subsequently, the graphene-coated fibre was baked at 60 °C in an oven for 10 minutes to thoroughly evaporate the residual water. This low temperature avoids damaging the PVB film during the long time baking. Finally, the device was baked at 120 °C for 1 minute to improve the adhesion between the graphene film and the fibre by softening the PVB film. The schematic process to fabricate a graphene-based device based on a side-polished fibre is summarised in Figure 4.10.

4.5 MoS_2-based Device Fabrication

4.5.1 MoS_2/Substrate Delamination

Before transferring, a PVB layer with a 1 μm thickness was spin-coated over the MoS_2 thin film. Then, instead of using a traditional chemical etching method, the PVB-coated MoS_2 was separated from the SiO_2/Si substrate using an ultrasonic-based etching-free method [89]. The PVB/MoS_2/substrate stack was first immersed into a beaker of water kept in an ultrasonic cleaner. After a few minutes, the edge of the PVB/MoS_2 film starts to detach from the substrate, eventually causing the PVB/MoS_2 stack to float on the water

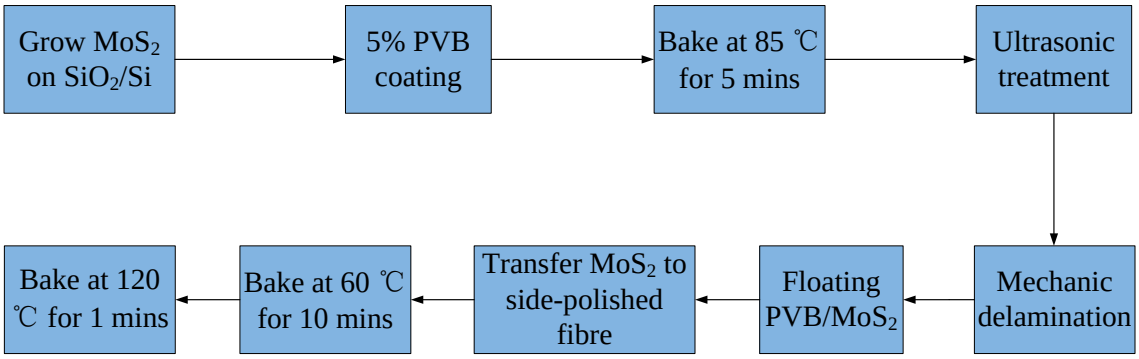

Figure 4.11: MoS_2 transfer process flow including: CVD-growth, PVB-coating, ultrasonic treatment, DI rinse and finally MoS_2 transferring.

surface. In the ultrasonic process, bubbling-induced force steadily delaminates the PVB-coated MoS_2 film from the SiO_2/Si substrate [89]. This etching-free method avoids traditional treatments involving hydrofluoric acid that would be required to remove the SiO_2/Si substrate, which is harsher than the Cu etching treatments using ammonium persulfate or iron chloride [89].

4.5.2 MoS_2 Transfer

After substrate delaminating, the PVB-coated MoS_2 sheet was rinsed in distilled water and floated on the water surface. The fibre was then immersed into the water and lifted under the floating MoS_2 film to transfer it onto the planar polished surface. Finally, the PVB-coated MoS_2 was baked at 60 °C in an oven for 10 minutes, and then at 120 °C for 1 minute to thoroughly evaporate the residual water and improve the adhesive between the MoS_2 film and the fibre. The schematic procedure to fabricate the MoS_2-based device based on a side-polished fibre is summarised in Figure 4.11.

4.6 Conclusion

This chapter described the growth of the 2D materials and the fabrication of the optical devices. Although a variety of methods exist for the growth of 2D materials, a CVD method was chosen to achieve the best device performance. Raman spectroscopy was used to confirm the monolayer feature of the graphene sheet. By combing Raman spectroscopy and SEM analysis, the thickness of the multilayer MoS_2 sheet was determined. After dis-

solving or delaminating the substrates, 2D materials were transferred to the planar surface window of the side-polished fibres using water-based methods.

Chapter 5

Graphene-based Fibre Polariser with PVB-Enhanced Light Interaction

5.1 Introduction

Polarisers are a category of devices used to obtain waves whose electric field vectors are restricted to a single direction [90]. Optical polarisers and polarisation devices have been widely used in both optical communications systems and polarisation-dependent optical sensors. Conventional polarisers are divided into absorptive, birefringent, thin-film, and subwavelength grating polarisers, depending on their physical functions [90]. Many of these conventional polarisers use bulk optical configurations, which are difficult to align and interface with fibre networks [91]. Thus, efficient, low loss, all-fibre-based polarisation components are highly desirable for seamless integration within existing systems. One method for constructing a fibre polariser is to use an optical fibre with a portion of its cladding removed and replaced with a thin-film overlay. Materials that have been used for this purpose include metal films [92], birefringent crystals [5] and liquid crystals [93]. However, these devices typically have a relatively narrow operation bandwidth, and/or high losses, which limit their application potential. In terms of extending the operation bandwidth, graphene is an excellent choice of material due to its unique band structure.

In this chapter, a novel approach is presented to producing a low loss, high extinction ratio graphene-based polariser with an enhanced light-graphene interaction. Firstly, the device design and simulations to investigate the PVB-enhanced light-matter interaction are discussed. Then, optical experiments are presented to show the device performance at

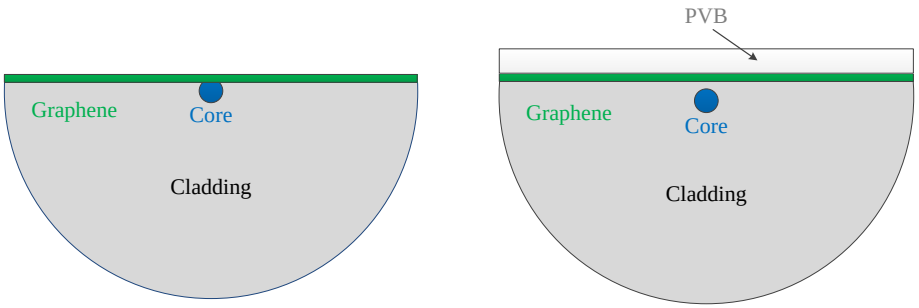

(a) (b)

Figure 5.1: (a) Cross-section of a graphene-based fibre polariser with side-polishing into the fibre core, as per [8]. (b) Cross-section of the fibre polariser used in this study with a residual cladding between the core and the graphene layer.

different wavelengths. The author designed and conducted all the simulations and experiments in this chapter. Dr. Li Shen helped in the measurement at 2000 nm.

5.2 Device Design

Several graphene-based optical polarisers have already been proposed and demonstrated [8,94,95]. In order to achieve a sufficient material interaction, previous work had placed a graphene sheet in contact with the fibre core as illustrated in Figure 5.1(a) [8]. This device had an extinction ratio of 19 dB, but also suffered from impractically high losses ($\sim$20 dB at 1550 nm) as the guided mode leaked out of the core. Other devices, such as the planar waveguide-based graphene polariser proposed in [95], have also exhibited large losses, in this case $\sim$20 dB at 1310 nm [95]. These results make it obvious that an alternative approach is required to obtain both the high performance and low device losses required for fibre-based systems.

In this chapter, a graphene-based fibre polariser is presented based on the side-polished fibre platform developed in Chapter 3. As has been discussed, the interaction window of the side-polished fibre is polished close to, but not into the core, thus suppressing the transmission losses. However, a drawback of this design is that the field of the core guided mode will have a low intensity at the surface of the window, resulting in a weak interaction with the mono-layer graphene film. To address this issue, a PVB over-layer was introduced. The longitudinal cross-section of the device is illustrated in Figure 5.1(b), which clearly shows

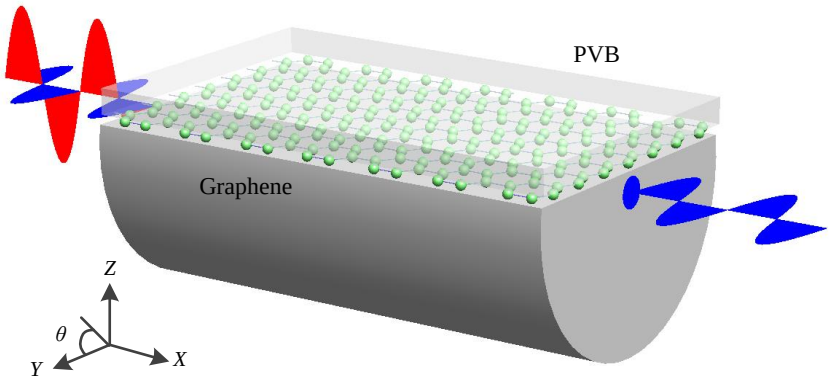

Figure 5.2: Schematic model of the graphene polariser, showing polarisation-dependent absorption. Polarisation angle θ is defined as $\theta = 0^\circ$ and 180° for TE mode (blue light wave), $\theta = 90^\circ$ and 270° for TM mode (red light wave).

the three-layer structure. The refractive index of the PVB over-layer ($\sim$1.48 as shown in Figure 5.3) is slightly higher than that of the silica fibre (core $\sim$1.45 and cladding $\sim$1.444 at 1550 nm) and so draws the evanescent tail of the propagating mode out of the core to enhance the light-graphene interaction without causing additional loss. The PVB-induced mode variation during transmission is illustrated in Figure 5.4. Importantly, as PVB exhibits low optical losses over most of the transmission window of the silica fibre platform, with appropriate design these multi-layer devices could be made to operate from visible wavelengths up to the edge of the mid-infrared. In Section 5.3, finite element modelling of the device mode properties will be conducted to quantify the level of enhancement with and without the PVB over-layer.

The mechanism of the graphene-based fibre polariser is based on differential attenuation of the TE and TM modes along the graphene sheet. The absorption of graphene arises from two distinct types of contributions, those from intraband and interband transitions [96,97]. Either of two contributions can dominate the absorption of graphene depending largely on the chemical potential [96,97]. This is because the conductivity of graphene can be tuned as a function of its chemical potential [46, 47]. As have been discussed in Chapter 2, mono-layer graphene used in this work has a chemical potential on the order of 0.1 eV. The conductivity of graphene has a negative imaginary component for 0.1 eV chemical potential. Ref. [98] shows that the interband transition dominates the absorption when the imaginary part of optical conductivity is negative. Thus, the TM mode of the

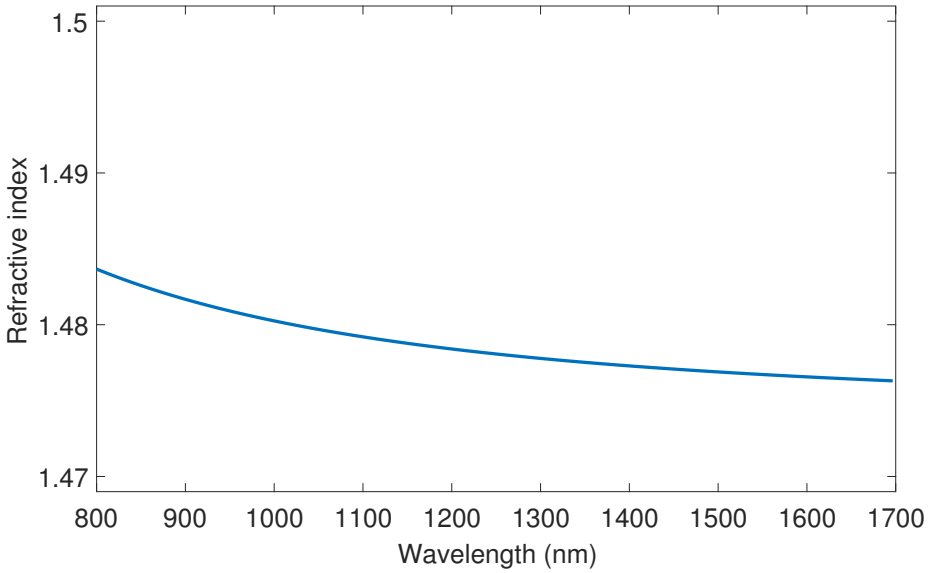

Figure 5.3: Refractive index of the PVB layer used in this work.

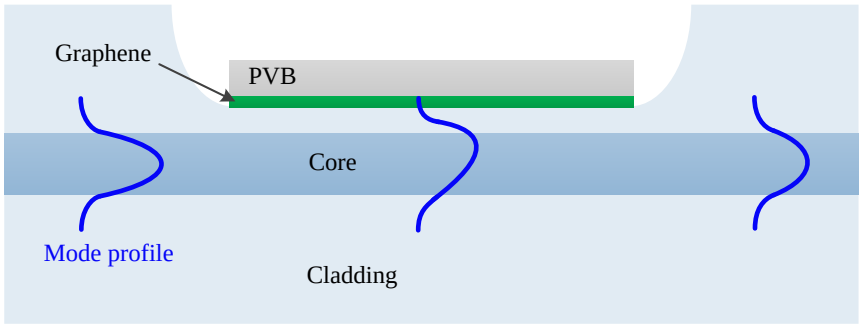

Figure 5.4: A schematic of the longitudinal cross-section of the device, solid blue lines indicate the propagating electromagnetic field.

fibre is expected to be preferentially absorbed by the graphene sheet based on Ref. [8], which can be used as a TE-pass polariser. A 3D schematic view of the resulting device is presented in Figure 5.2, which shows absorption of the TM mode and transmission of the TE mode.

5.3 Numerical Simulation of PVB Enhancement

In order to determine the effect that the PVB layer has on the transmission properties of the device, a numerical study was undertaken using a finite element method (FEM). A RF module in COMSOL Multiphysics was used with a scattering boundary condition to

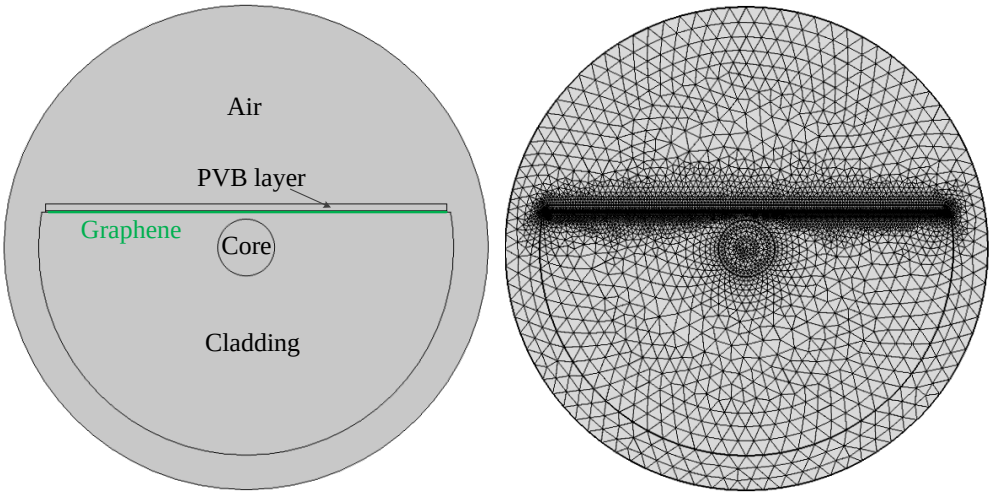

Figure 5.5: (a) Simulation cross-section of the PVB-coated graphene device. (b) Cross-section of the finite elements in COMSOL Multiphysics.

avoid any reflection. By dividing the simulation domain into smaller subdomains forming a mesh as shown in Figure 5.5 (a) and (b), the electric field distribution of the simulation area was calculated solving Equation 5.1. Then, it is possible to estimate the absorption of the two orthogonal polarisation modes through the imaginary component of the mode effective refractive indexes N_{eff} that is given in the simulation results. Thus, the extinction ratio ER at different wavelengths can be calculated by using the following equations:

$$N_{eff} = N_{real}(\lambda) + iK_{imag}(\lambda), \tag{5.1}$$

$$Loss(\lambda) = L * \alpha(\lambda) = \frac{4\pi K_{imag} L}{\lambda c}, \tag{5.2}$$

$$ER(\lambda) = Loss_{TE}(\lambda) - Loss_{TM}(\lambda). \tag{5.3}$$

where, E is the electric field and ϵ_r denotes the relative material-dependent permittivity. $k_0 = \omega c^{-1}$ is the wave number of the mode field. $N_{real}(\lambda)$ and $K_{imag}(\lambda)$ are the real and imaginary parts of the mode effective refractive index, respectively. L is the length of the device, $\alpha(\lambda)$ is absorption coefficient and c is the speed of light. Since ϵ_r is material-dependent, the electric field distribution is dependent on the refractive index of the materials. The refractive index of the materials across the wavelength range of interest, including fibre core, cladding and graphene, has been given in Chapter 2.

As a starting point for the simulation, the parameters corresponding to those in Figure 5.6 are given in Table 5.1. As have been discussed in Section 5.2, the refractive index of PVB is slightly larger than that of the silica fibre, so draws the evanescent tail of the

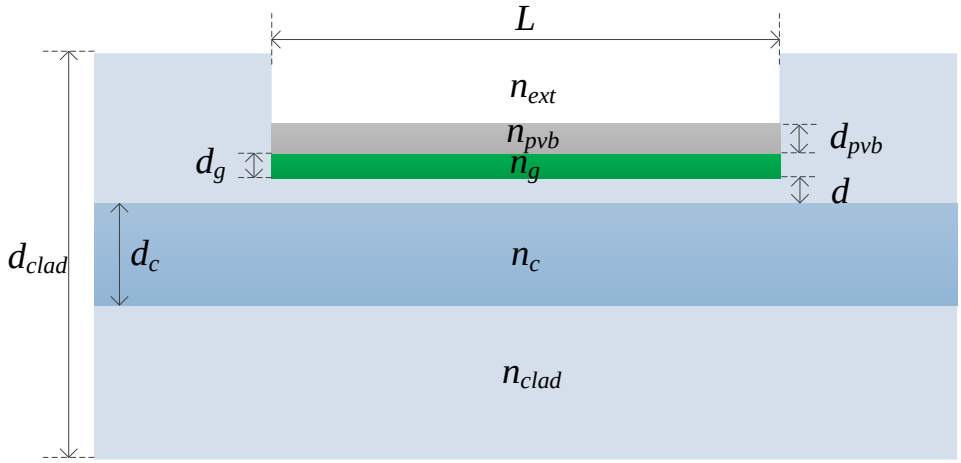

Figure 5.6: FEM simulation geometry.

Table 5.1: FEM simulation parameters.

Wavelength	Fibre core index n_c	Fibre cladding index n_{clad}
1550 nm	Equation 2.4	Equation 2.4
Graphene index n_g	PVB index n_{pvb}	Air index n_{ext}
Equation 2.35	1.48	1
PVB thickness d_{pvb}	Graphene thickness d_g	Polishing region length L
1 μm	1 nm	1 cm
Residual cladding thickness d	Fibre core diameter d_c	Fibre cladding diameter d_{clad}
1 μm	8.2 μm	125 μm

propagating mode out of the fibre core. Figure 5.7(a) and (b) show the electromagnetic field distributions of the fundamental TM and TE modes at the uniform polished sections of the fibre when coated with a 1 μm thick PVB layer on top of the graphene. For comparison, Figure 5.7(c) and (d) show the same modes calculated without the PVB layer. These figures clearly illustrate the increased light-matter interaction at the polished fibre surface when the high index layer is included. Further verification is provided by Figure 5.8, which shows the intensity distribution across the positions indicated by the dashed lines in Figure 5.7. From this figure, an increase of $\sim$10 dB of modal interaction is estimated at the polished surface, which can be attributed to the PVB over-layer. To investigate the influence the PVB layer thickness has on this interaction, Figure 5.9 plots the calculated extinction ratio as a function of wavelength when the PVB thickness varies from 0.6 μm to

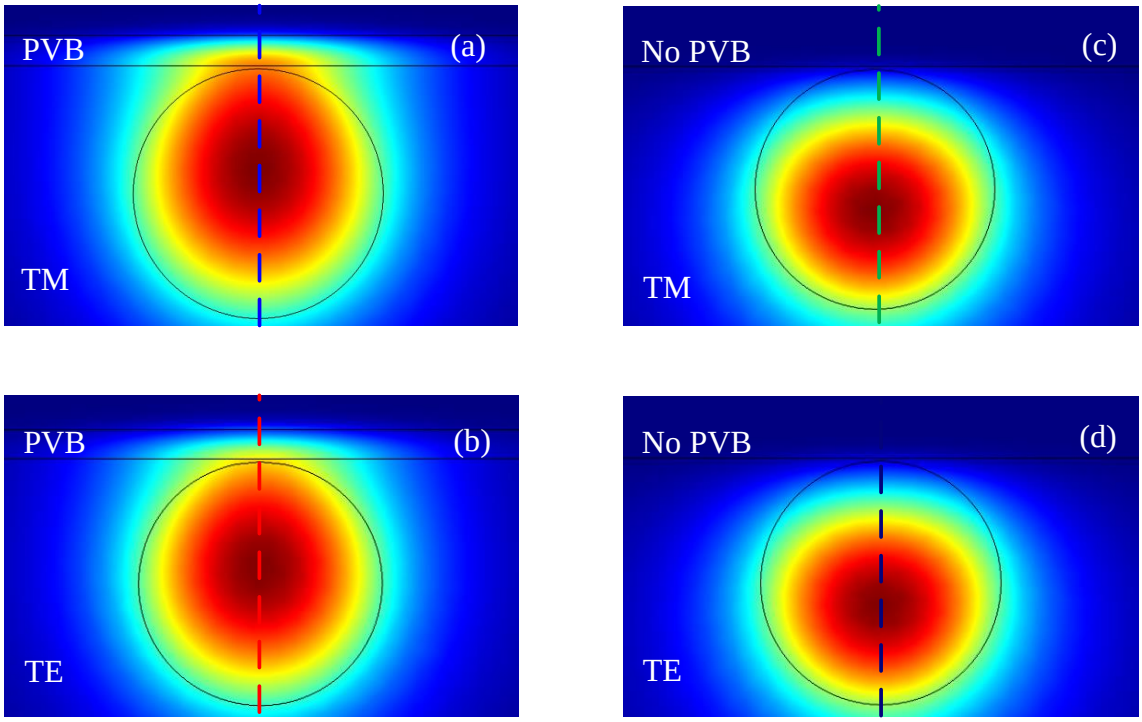

Figure 5.7: Numerical finite element simulations of modes within the uniform polished sections at 1550 nm. Electric field distributions for (a) TM and (b) TE modes of a side-polished optical fibre with PVB-coated graphene layer, and for (c) TM and (d) TE modes of the same fibre but with graphene only at the polished surface.

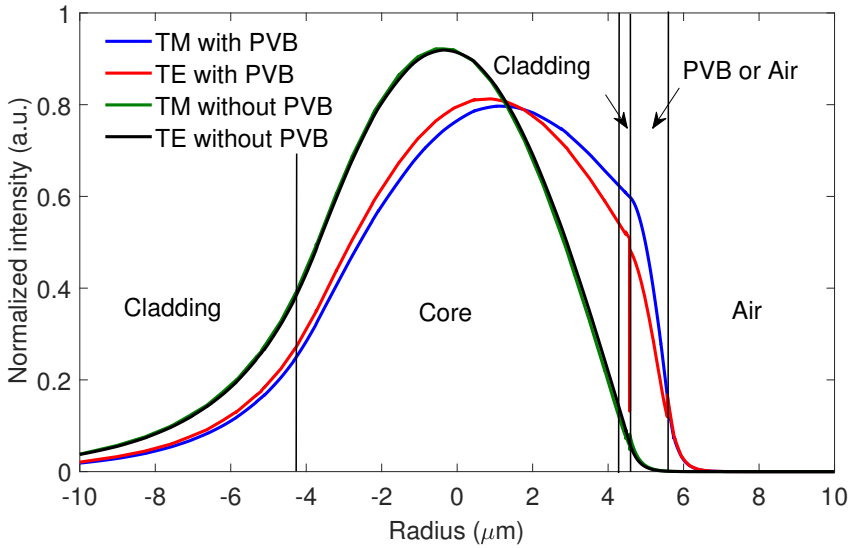

Figure 5.8: Normalized cross-sectional line scan along dashed lines indicated in Figure 5.7.

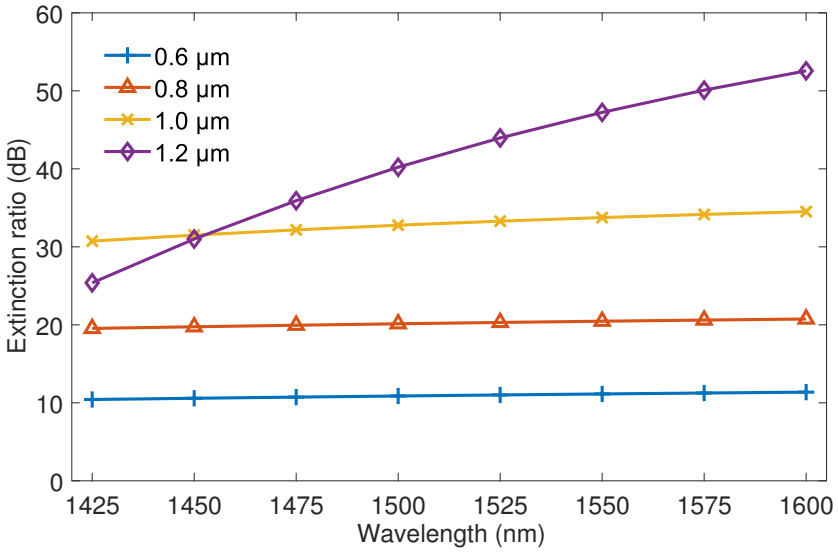

Figure 5.9: Numerical simulation results showing the extinction ratio as a function of wavelength for different thicknesses of the PVB layer.

1.2 μm in 0.2 μm steps. In general, a thicker PVB layer results in a larger extinction ratio across the wavelength range shown here. This is because the refractive index of the PVB is larger than that of the fibre core. However, when the thickness reaches a value of 1.2 μm, the core guided mode becomes leaky for both polarisations. At shorter wavelengths, this effect is more distinct due to smaller mode areas and results in a large reduction of the extinction ratio. Thus, a 1 μm thick PVB layer was deemed to be the optimum choice for this work. It is worth pointing out that because the PVB is only 1 μm thick, the propagating mode in this device is still bound to the core, i.e., the PVB layer does not induce any radiation loss.

5.4 Experiment Setup

To characterize the optical transmission properties of the graphene-based fibre polariser, an experiment was conducted using the configuration shown in Figure 5.10. A tunable continuous wave (CW) laser (Yenista Tunics T100s; working wavelength: 1425 to 1600 nm; output power: 1 mW, corresponding to 0 dBm) was used as the input source so that the optical transmission could be measured across a broad wavelength range. Low power lasers were used to avoid any possible nonlinear effects that may interfere with the measurement of the polarising properties of graphene [8]. The laser was free-space launched

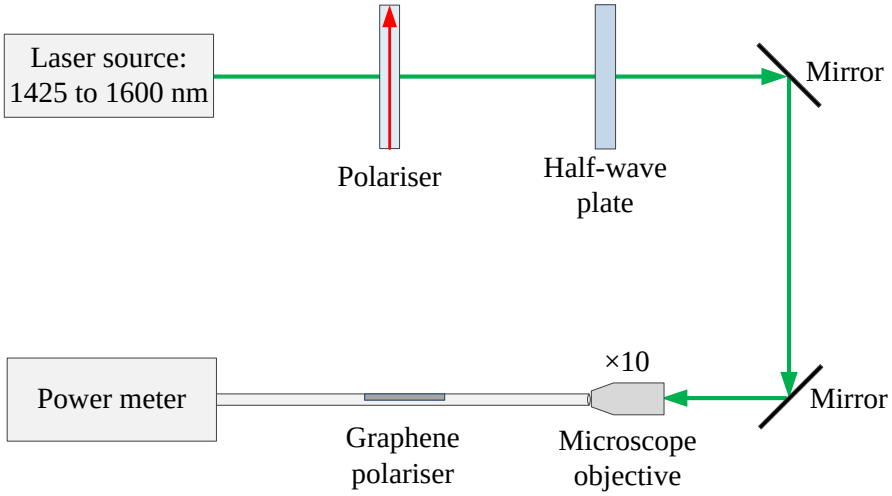

Figure 5.10: Experimental configuration used for the polarisation measurements excited by near-infrared light. Output power value corresponds to the distance between the data point and the centre.

into the fibre device using a 10× magnification microscopic objective lens with ∼2 dB of coupling loss. Prior to this, polarisation control was used to ensure the fidelity of the linear polarisation state. A half-wave plate (Thorlabs AHWP05M-1600; working wavelength: 1100 to 2000 nm) was used to rotate the polarisation axis of the input light continuously. Since polarisation non-maintaining fibres were used in this study, the fibre lengths were kept short and the device was maintained as straight as possible to prevent unwanted polarisation degradation and additional birefringence. The output power was then monitored via a power meter (Thorlabs PM 100D) for different polarisation angles and wavelengths.

5.5 Experiment Results

Investigations of the transmission properties of the graphene-based fibre device began by comparing the losses of the TM and TE modes. The input power was set to 0 dBm and the polarisation axis of the incident laser was tuned continuously by rotating the half-wave plate. The power meter showed immediate, significant variation when the polarisation axis of the incident laser was changed. The half-wave plate was rotated in steps of 5° to change the polarisation axis of the laser in steps of 10°, since the angle between the output polarisation and the input polarisation will be twice the angle between the input polarisation and the axis of the half-wave plate. The polarisation angle, defined as the

Table 5.2: Measurement of other four graphene-based fibre devices.

Device	Loss at 1550 nm	Extinction ratio at 1550 nm
Device one	1 dB	33 dB
Device two	1.5 dB	29 dB
Device three	1.3 dB	23 dB
Device four	0.3 dB	12 dB

angle between E field and the fibre polishing surface, is set to 0° and 180° for the TE modes and 90° and 270° for the TM modes.

An example polar plot of the transmitted power as a function of polarisation angle is shown in Figure 5.11, for the wavelength of 1550 nm. The output power values in Figure 5.11 are corresponding to the distances between the data points and the centre. It is clear that for the angles of 0° and 180°, when the TE mode was aligned to interact with the graphene, the transmission was maximized to around -3 dB and when the polarisation was rotated to 90° and 270° the transmission dropped to -37 dB, evidence of the TE pass nature of our device. This large attenuation difference between the TM and TE modes provides a good indication of the high purity of our graphene sheet and the strong light-matter interaction that has been achieved. Considering the -3 dB maximum output power and the -2 dB coupling loss, the device loss at 1550 nm is $\sim$1 dB. To further determine the magnitude of the enhancement of the light-graphene interaction due to the PVB, the experiment was repeated on a device with a graphene only layer. In this experiment the extinction ratio was just 3 dB, thus the PVB layer increased the interaction by more that 30 dB, in agreement with the simulation results in Figure 5.8. To check the reproducibility of the graphene-based polarisers, the transmission loss and the extinction ratio of four other devices were measured using the same setup, as shown in Table 5.2. The first three devices produced very similar responses to the original structure. The low extinction ratio (also low loss) of the device four is believed due to the large distance (more than 2 μm) between the polished surface and the fibre core.

Additional polarisation measurements were also undertaken across the full wavelength range of our tunable laser source (1425 to 1600 nm), as shown in Figure 5.12. By subtracting the TE output power from the TM output power at each wavelength, the extinction ratio can be calculated and does not drop below 26 dB across the full wavelength range.

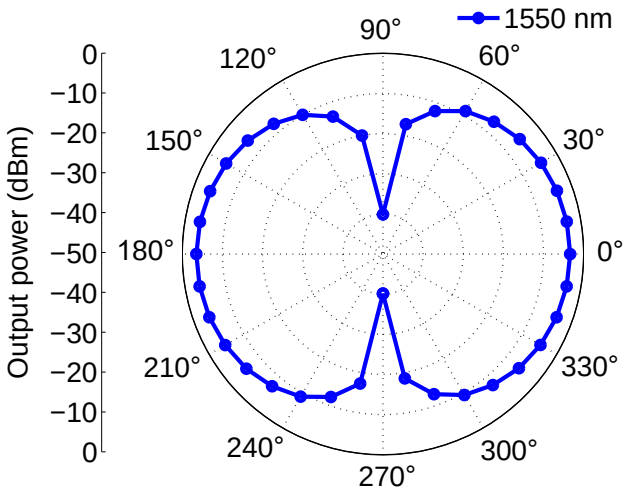

Figure 5.11: Polar plot of the output power measured at 1550 nm when the input power is 0 dBm. Output power value corresponds to the radius of the data point.

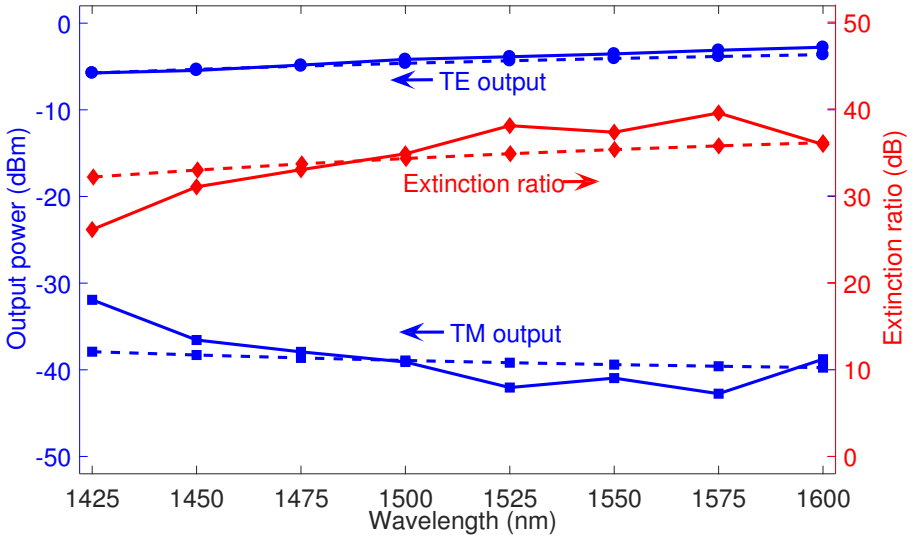

Figure 5.12: Solid lines: experimental output powers for TE and TM modes and corresponding extinction ratios. Dash lines: predicted extinctions obtained from simulations in Section 5.3.

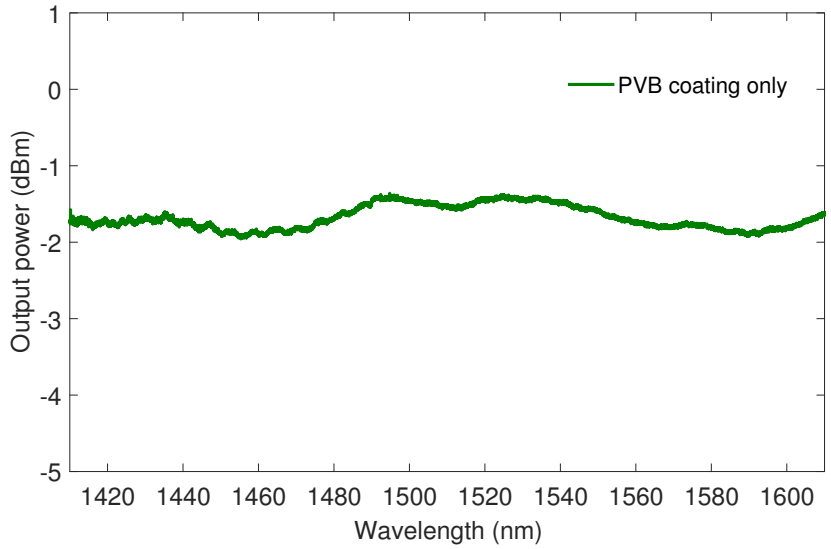

Figure 5.13: Experimental output power of a PVB-only coated side-polished fibre.

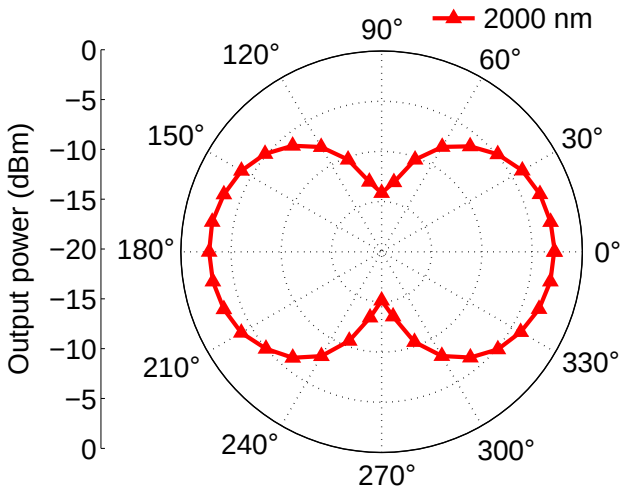

Figure 5.14: Polar plot of the output power measured at 2000 nm when input power is 0 dBm. Output power value corresponds to the radius of the data point.

These results also agree well with the theoretical simulation results calculated over this range (dash lines in Figure 5.12, conducted using the same simulation method as discussed in Section 5.3), providing clear evidence of the broadband nature of our device and the significant improvement in the performance over previously reported results [8,94,95]. Moreover, the polarisation extinction ratio increases with larger incident wavelengths. This is because absorption of the TM light increases with increasing wavelength, which can be explained by the higher proportion of the evanescent field at the graphene interface. A control experiment was also performed on a PVB-only coated side-polished fibre to determine the effect of the PVB coating. Figure 5.13 shows the output power of a PVB-only coated side-polished fibre, meaning that the large absorption of the PVB-coated graphene device is due to the graphene layer not the PVB layer. No obvious difference was found for the output of the PVB-only coated side-polished fibre at different polarisation states.

To provide further evidence of the broadband nature of the device, the measurements were extended to an operating wavelength of 2000 nm. A Cr^{2+}:ZnSe laser diode (IPG Model SFTL-Cr-ZnSe-2300-1000) was used to generate a CW signal and its polarisation measurement was conducted using the same setup shown in Figure 5.10. The polar plot in Figure 5.14 shows the result of this experiment with a maximum value of -3.5 dB and a minimum of -16.5 dB detected at the output of our device when input is fixed at 0 dBm. Comparing this to the results at 1550 nm, the lower extinction ratio of 13 dB is attributed to the limited polarisation maintenance of the standard SMF at this longer wavelength. Nevertheless, these results represent the highest extinction ratio measured at 2000 nm for a graphene-based fibre polariser.

Finally, it is also worth noting that as well as enhancing the light-graphene interaction, the PVB film also acts as a protective over-layer to improve the long-term stability of these devices, and no degradation has been observed when monitoring their performance over a 12-month period.

5.6 Conclusion

In this chapter, a graphene-based side-polished fibre polariser has been designed and experimentally demonstrated. By coating a high index PVB over-layer onto the graphene film, both the simulation and experimental results show that the light-matter interaction

between the graphene film and the core-guided mode is enhanced. Characterization of the graphene-based fibre polariser shows a high extinction ratio of $\sim$37.5 dB and a low device loss of $\sim$1 dB. To my knowledge, this device offers an order of magnitude improvement in performance over any previously reported fibre-based graphene polarisers, while at the same time reducing the device loss by more than two orders of magnitude. Furthermore, an extinction ratio greater than 26 dB was recorded across the wavelength range 1425-1600 nm, in good agreement with the numerical investigations. An additional value of 13 dB extinction ratio was achieved at 2000 nm, which confirms the broadband nature of our device. As the reduced extinction at 2000 nm is most likely due to the limited polarisation maintenance of the SMF at this wavelength, more optimal fibre designs are expected to enable device operation across the fibre's entire single-mode transmission window.

Chapter 6

All-Optical Graphene-based Fibre Modulator

6.1 Introduction

As have been discussed in Chapter 5, graphene is expected to respond to wide-band signals spanning microwave to ultraviolet, which have been utilized to develop a low loss, high extinction ratio graphene-based polariser. In this chapter, graphene's optical properties are future explored based on the same optical fibre platform. Of graphene's exceptional features, its dynamic conductivity and low effective carrier mass are of particular interest for optoelectronic applications, as they underpin the material's broadband nonlinear optical absorption and ultra-fast carrier mobility, respectively. An alternative approach that offers a straightforward route to ultra-fast modulation is to exploit the strong saturation of graphene's absorption due to Pauli blocking, whereby the generated carriers fill up the valence bands preventing any further transitions.

An optical modulator is a device that is used to modulate light propagating either in free space or in an optical waveguide. Thus, such devices have been widely used in many optical communication-based applications [99]. Optical modulation controls the intensity, phase, or polarisation of light by an electric field or another beam of light, corresponding to electro-optic or all-optical modulation, respectively [100]. The electro-optic approach is mostly used in current optical modulators. However, conventional electro-optic modulators usually suffer from narrow modulation bandwidth and high optical propagation loss [101]. Thus, all-optical modulation that makes use of the excellent properties of 2D

materials, including graphene, TMDCs, and black phosphorus, has attracted increased attention in recent years due to the possibility of developing more compact, broadband, and high modulation rate devices [21, 99, 102].

This chapter will start with a brief introduction of the all-optical modulation mechanism. Then, a nonlinear measurement will be used to illustrate the strong saturable absorption of graphene. Finally, a pump-probe experiment will be used to demonstrate the strong all-optical modulation in the graphene-based device. The author designed and conducted all the experiments in this chapter. Dr. Li Shen helped in the pump-probe measurement.

6.2 All-Optical Modulation

All-optical modulation is carried out entirely within the optical domain by using a switching light beam (e.g., ultrafast pulses) to control the propagation of another light beam (i.e., signal), without the need for conversion of an optical signal to an electrical signal [103]. Most all-optical modulation devices make use of the third-order nonlinear optical response of a material [104], including saturable absorption [105–107] or the optical Kerr effect [104, 108, 109]. Saturable absorption is a process that originates from valence band depletion, conduction band filling, and ultra-fast intraband carrier relaxation, whereby the generated carriers fill up the valence bands preventing any further transitions [105]. Thus, it is due to the material's intensity-dependent optical absorption and the absorption will reduce with increasing input optical power. As discussed in Section 2.3.3, graphene is an excellent material to explore all-optical modulation because of its strong saturation absorption due to Pauli blocking and high electron mobility. An excellent example of this is a saturable absorption-based all-optical modulator that was recently demonstrated by employing a pump-probe scheme in a graphene-coated microfibre device [106]. However, although this result represented a nice first demonstration, the interaction between the evanescent field of the tapered fibre and the graphene coating was quite modest, limiting the modulation depth. Thus this experiment highlights the importance of achieving a strong light-matter overlap to realize high performance optoelectronic devices using 2D material systems [15, 110]. Addressing this issue is becoming an increasingly important and timely topic of research, with several approaches already being pursued [110, 111].

6.3 Saturable Absorption Measurement

To characterize the nonlinear saturable absorption of graphene, a high power transmission experiment was undertaken on the graphene-based fibre device. As have been discussed in Section 5.5, the TM mode has the weakest output power while the TE mode gives the strongest output power, due to minimal interaction between graphene and the TE mode. Thus, saturable absorption will only occur for the TM mode.

6.3.1 Experiment Setup

The setup for the high power transmission experiment is shown in Figure 6.1. A high power fibre laser (Onefive Origami 15) was used to generate pulses operating at 1540 nm, with a duration of 750 fs (FWHM) and a repetition rate of 40 MHz. Polarisation control was used to change the input polarisation state to TM or TE mode and a variable attenuator was connected to the output of the pulsed laser to adjust the input power level. The signal was free-space launched into a 50/50 coupler using a 10× magnification microscope objective lens, where 50% of the power was coupled through the graphene-based fibre device and monitored by a power meter 1 (Thorlabs PM 100D), and 50% of the power was coupled to another power meter 2 (some model) as a reference power, as shown in Figure 6.1. The output powers, with and without the graphene device, were measured simultaneously for different input power levels. Since non-polarisation-maintaining fibres were used, the fibre lengths were kept short to prevent polarisation degradation and maximize the polarisation-dependent light interaction with the graphene. The transmission of the TE and TM modes were monitored as a function of input power levels by a similar procedure, which is adjusting the variable attenuator to tune the output of the laser from zero to its maximum, and recording the two power meter readings simultaneously.

6.3.2 Experiment Results

The transmission of the TE and TM modes were monitored as a function of input powers. Data recorded from the power meter 2 was taken as the input power level. Then, the transmission of the graphene device could be calculated based on the reading of the power meter 1, which measures the output power. Figure 6.2 shows the transmittance of the TE

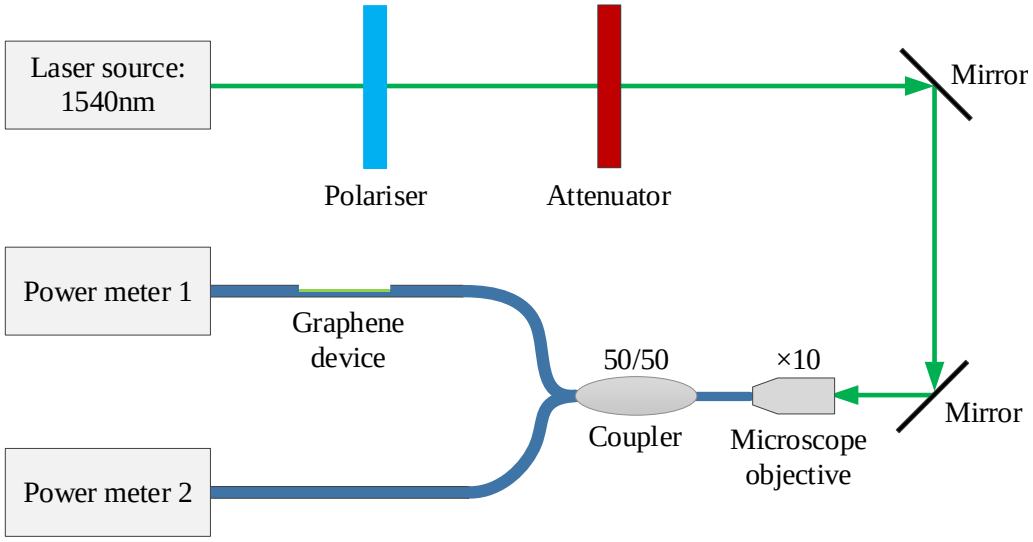

Figure 6.1: Experimental configuration for the high power transmission measurements.

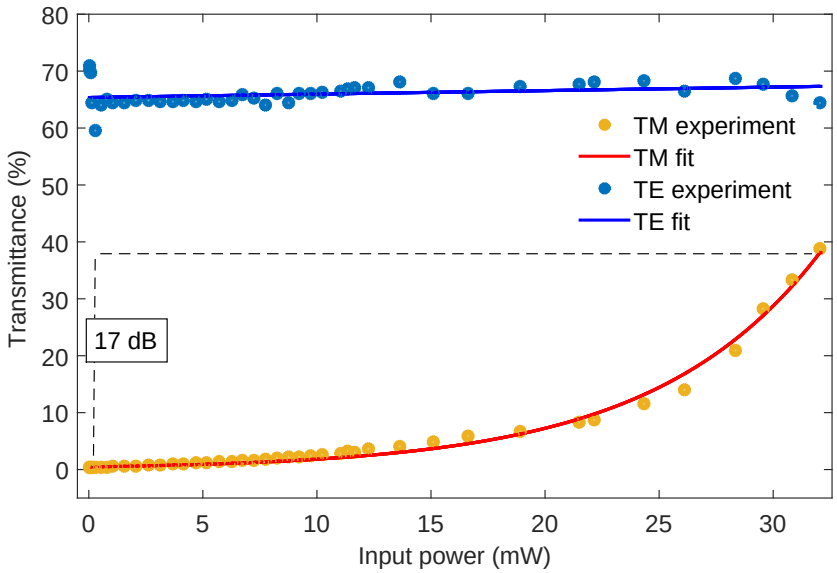

Figure 6.2: Non-linear absorption saturation. Transmittance measurements of graphene coated fibre device as a function of average power P_{ave}.

and TM modes as a function of increasing average power P_{ave} coupled into the device. This clearly shows that up to P_{ave} $\sim$10 mW the absorption of the TM mode is linear. However, for higher input powers the absorption becomes nonlinear and the transmitted light starts to increase exponentially, eventually reaching a transmittance of 60 % for P_{ave} $\sim$32 mW. At this highest power, the transmission of the TM mode has increased by $\sim$17 dB compared to the transmission at the lowest power. In contrast, the transmission of the TE mode remains linear when the input power is increased up to the maximum available power. This is due to the minimal interaction between the TE mode and the graphene sheet, as described in Chapter 5. From these results, the maximum extinction ratio for all-optical modulation using this device can be deduced to be 17 dB, which is estimated by the maximum change in the transmission of TM mode. However, it is anticipated that this could be improved with stronger optical pumping since the TM mode absorption has not saturated at the largest available power of our experiment.

6.4 Pump-Probe Measurement

The strong nonlinear absorption effect of graphene can be readily employed for all-optical modulation. In order to determine the temporal dynamics of the saturable absorption, a simple pump-probe modulation scheme was employed to explore the ultrafast carrier mobility and the all-optical modulation feature of graphene. Two light beams were split off from a single beam of laser to generate a pump beam and a probe beam in the experiment. The pump beam with a high optical intensity excites carriers in the graphene, which modify the absorption probed by a subsequent probe pulse [100, 112]. The probe beam with a much lower optical intensity does not significantly affect the graphene. By measuring the transmittance of the probe signal as a function of the delay between the pump and probe pulses, it is possible to observe the relaxation time of the graphene [112].

6.4.1 Experiment Setup

In the pump-probe experiment, the pump and probe beams were controlled to overlap in the sample. Since the intensity of the probe is much weaker than the pump, the nonlinear effect induced by the probe can be ignored. The pump-probe set-up is illustrated in Figure 6.3. In the experiment, the high power 1540 nm pulse laser, same as in Section 6.3.1, was

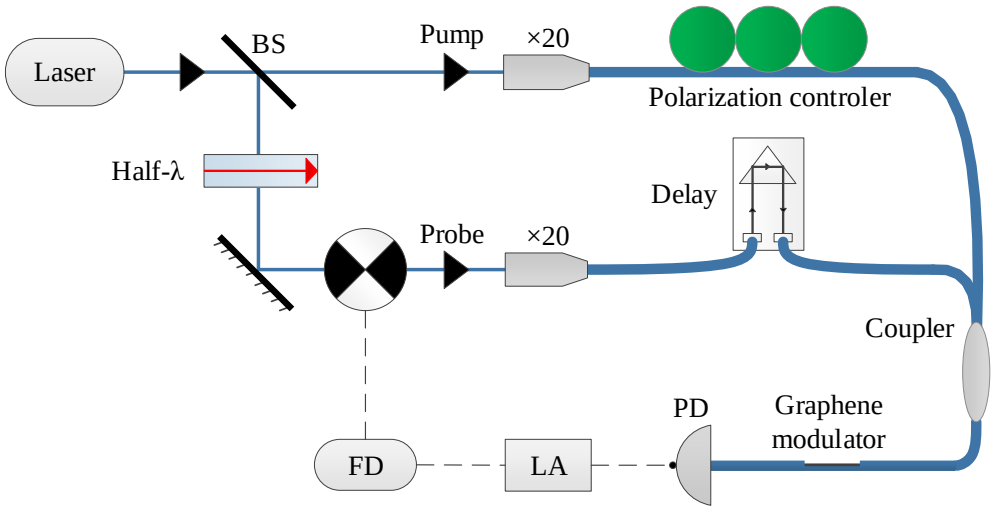

Figure 6.3: A schematic illustration of the experimental set-up used for pump-probe modulation. BS: beam splitter; FD: frequency driver; LA: lock-in amplifier; PD: photo-diode.

split by a beam splitter (BS) into a high power pump (P_{ave} ∼20 mW, corresponding to a peak power of P_p ∼720 W) and a weak probe component (P_{ave} ∼130 μW, P_p ∼4 W). The probe was modulated at 100 Hz using an optical chopper connected to a lock-in amplifier (LA). A frequency driver (FD) sent control sequences to the optical chopper and trigger signal to the LA with the same frequency. Both pump and probe signals were detected by a photo-diode (PD) and sent to the LA by the PD. The trigger signal serves as the reference for the LA which extracts the probe signal from the pump signal and background noise. Thus, the two signals at the same wavelength can be discriminated. A zero-order half-wave plate and a polarisation controller were inserted in the optical paths to ensure that both the probe and pump were aligned to couple into the TM surface wave to maximize the light-graphene interaction. A variable time delay (Santec ODL-340 module) was inserted into the probe path to generate a 10 ps adjustable delay between the probe and pump pulses and to control the overlap between the two pulses. The pump and probe pulses were then recombined using a fused tapered coupler before being connected to the input arm of the device under test.

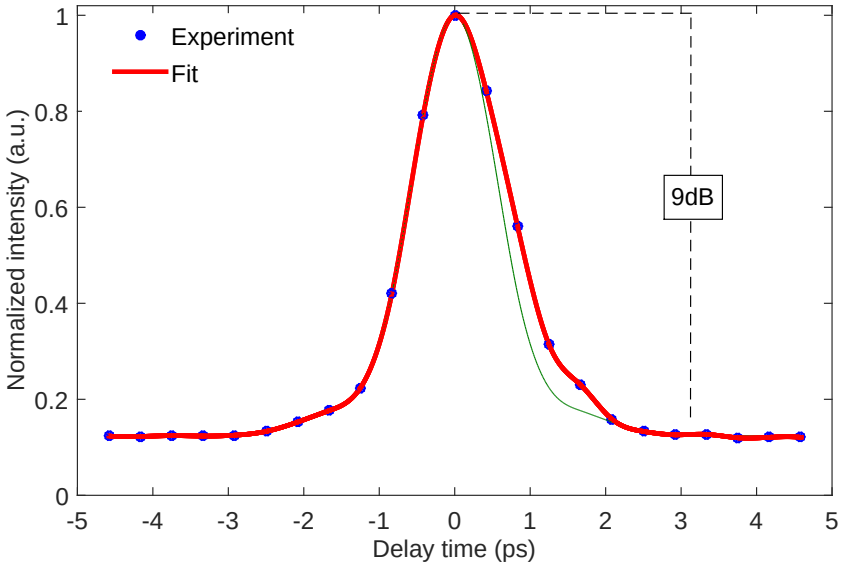

Figure 6.4: Measured nonlinear absorption of the weak probe pulse (blue dots). Fitted curve (red line). The green line is mirroring of the rising edge of the pulse and is included to highlight the slower falling edge which is due to the carrier recovery in the graphene sheet.

6.4.2 Experiment Results

The normalized transmission of the signal pulse as a function of the pump-probe delay time T is given in Figure 6.4. It clearly shows that the power of the transmitted probe signal is maximum at the zero delay time. As the delay overlap is tuned, the normalized probe intensity is increased up to a maximum value, corresponding to a 9 dB increase. The operation bandwidth of the graphene device can be calculated to be 0.5 THz based on the 2 ps modulation time scale. Overlaying the measured response with that of the pump itself (green line in Figure 6.4), it is clear that the rise time is simply governed by the pump duration, however the fall time is slightly longer, which can be attributed to the intrinsic carrier recovery processes in graphene. The carrier dynamics were estimated by considering the symmetry of the pump pulse and deconvolving it from the modulated response. The relaxation times were then estimated by analytical fits to the data using decaying exponential Equation 6.1. By adjusting the parameters τ_1 and τ_2 in the Equation 6.1, a best match between the fitting and the data is achieved and plotted in Figure 6.5. Thus, these relaxation processes occur on two different time scales, which are estimated from the best fitting to be an initial fast relaxation time τ_1 $\sim$0.1 ps and a slower relaxation time τ_2 $\sim$0.4 ps, in good agreement with previous reports [113].

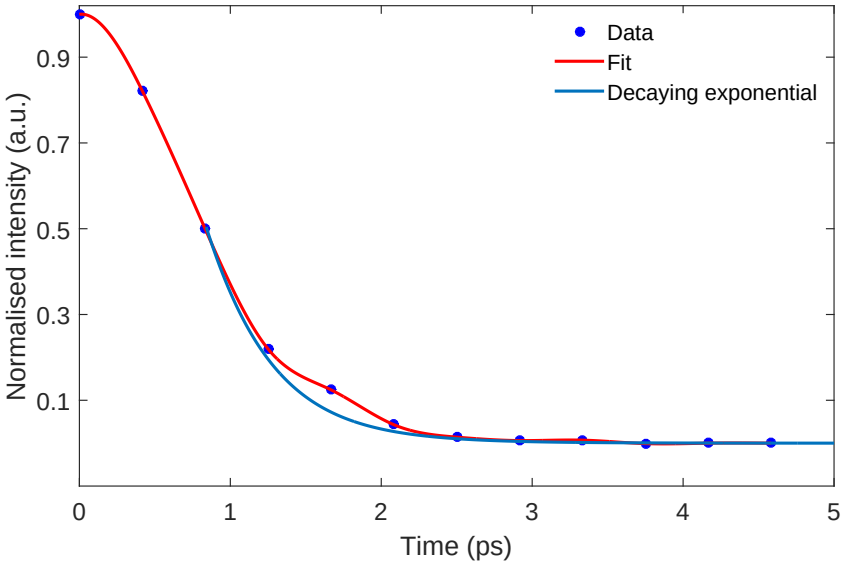

Figure 6.5: Analytical fits to the data using decaying exponentials.

$$f = exp(-\frac{T}{\tau_1}) + exp(-\frac{T}{\tau_2}) + sech(T - T * 2.4)^2. \tag{6.1}$$

6.4.3 Figure of Merit

When compared to previous devices, the method developed in this work shows an enhanced interaction with the graphene sheet to produce a significant increase in modulation depth, while at the same time suppressing the insertion loss. This is best illustrated by applying the FOM, defined as Equation 6.2 [114]. The FOM provides a means to compare the maximum achievable performance between different devices. FOMs are calculated for the previous graphene-based modulators and are presented in Table 6.1. The variations of FOM are fairly wide, ranging from 0.19 to 9. Our device have a $FOM = 9$, almost double that of the previous best efforts ($FOM = 4.8$ in Ref. [114]).

$$FOM = \frac{Extinction\ ratio}{Insertion\ loss}. \tag{6.2}$$

Table 6.1: Comparison of FOM for different graphene-based modulation devices.

Platform	Material	Wavelength	Extinction ratio	Loss	FOM	Ref
Current work	graphene	1550 nm	9 dB	1 dB	9	[115]
Fibre	graphene	1550 nm	16 dB	3.3 dB	4.8	[114]
SOI	graphene	1537 nm	6.5 dB	4 dB	1.625	[111]
Waveguide	graphene	1550 nm	15 dB	12 dB	1.25	[116]
Waveguide	graphene	1550 nm	2.9 dB	2.5dB	1.16	[117]
Fibre	graphene	1550 nm	0.11 dB	0.45 dB	0.24	[118]
Fibre	graphene	1500 nm	2.1 dB	11 dB	0.19	[106]

6.5 Conclusion

In this chapter, a graphene-based all-optical modulator has been designed and experimentally demonstrated using the approaches developed in Chapter 3 and Chapter 4. Compared with conventional modulators, the graphene-based modulator has advantageous properties such as more compact size, broadband operation wavelength, and lower optical propagation losses. Nonlinear absorption measurements of the device show the transmission of the TM mode increases by $\sim$17 dB when the input power changes from the lowest to the highest level. All-optical modulation was characterised by a pump-probe experiment to get an extinction ratio as high as 9 dB and operation bandwidth of 0.5 THz. The method results in an enhanced interaction with the graphene sheet to produce a significant increase in modulation depth, while at the same time ensuring a large decrease in insertion loss. This approach presents a significant improvement in performance in all key measures to simultaneously obtain low transmission loss, high speed, and high modulation depth.

Chapter 7

Resonance-Enhanced Optical Nonlinearities in a MoS_2-Coated Fibre

7.1 Introduction

MoS_2 has become a noteworthy complimentary material to graphene sharing many of its excellent properties, like high photosensitivity [119]. MoS_2 also offers properties that are unattainable in graphene. Few-layer MoS_2 has an electronic band structure that is dependent on the number of layers and is, therefore, a very promising material for opto-electronics, photonics and lasing applications [21]. The layer thickness can also be used to control the size of the nonlinear coefficients which is useful for applications involving high intensity light.

This chapter investigates few-layer MoS_2 materials for use in nonlinear optical applications in the telecoms region. It will start with a brief description of the MoS_2-coated fibre design. Then, the linear and nonlinear absorption measurements will be discussed. The results show the nonlinear response of the MoS_2-coated fibre could be significantly enhanced via resonant coupling to the thin film material, allowing for the observation of spectral broadening and enhanced all-optical modulation. The interaction of light with low-dimensional materials is notoriously difficult and until now, the level of modulation depth of varying geometries, has been limited to several dB [27, 28]. Compared to these previous devices, this approach presents a significant improvement in the MoS_2-light interaction efficiency, resulting a much larger modulation depth. Thus this work paves the way to the development of practical 2D material-based nonlinear photonic devices for telecoms

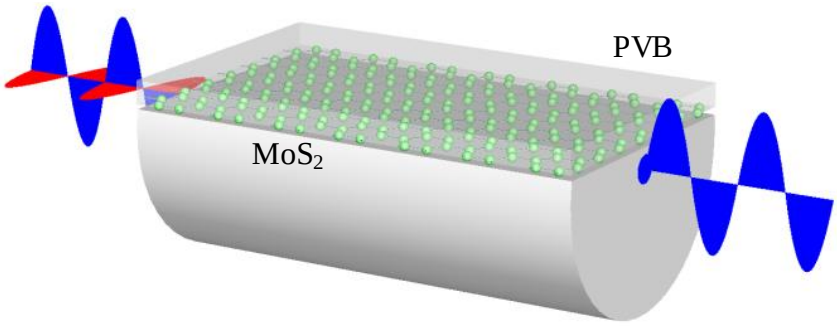

Figure 7.1: Schematic model of the PVB-coated MoS_2 device based on a side polished optical fibre.

applications. The author designed and conducted all the experiments in this chapter. Dr. Antoine Runge helped in the transmittance measurement.

7.2 Device Design

A schematic representation of the MoS_2-coated side-polished fibre device is illustrated in Figure 7.1. A side polished fibre similar to that discussed in Chapter 3 was used as the device fabrication platform. The interaction window of the polished fibre is $\sim$ 1 cm and a cladding buffer of 1 μm was retained across the polishing region while still permitting access to more than 30 dB of the light. The polishing process was optimized to ensure that the polished surface was parallel to the fibre core along its entire window. A CVD-grown MoS_2 film was coated with a 1 μm PVB layer and then transferred onto the polished window using the method discussed in Chapter 4. The high index PVB layer coated on top of the MoS_2 film was used to improve coupling to the 2D films. The thickness of the MoS_2 film is $\sim$14.5 nm, as shown in Figure 4.7 and the estimated number of the MoS_2 layers is $\sim$ 21 due to $0.6 - 0.7$ nm MoS_2 monolayer thickness [83]. This thickness is comparable to what has been used in earlier MoS_2-based devices [51]. Cross-sectional measurements conducted on several samples prepared via this route indicate that the thickness variation of these MoS_2 layers is on the order of a few nanometers. It is worth noting that the absorption spectrum measured in [120], for a film of similar thickness ($\sim$15 nm), reveals two direct-gap transitions, confirming that the samples band structure is still in the few-layer regime.

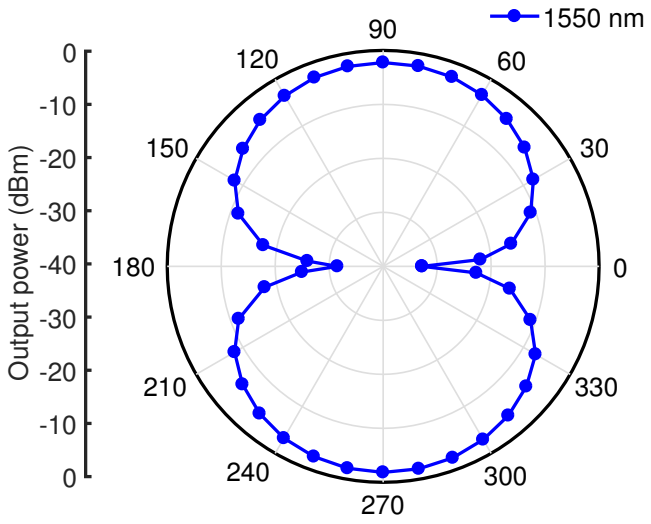

Figure 7.2: Polar plot of the output power measured at 1550 nm when the input power is 0 dBm. Output power value corresponds to the radius of the data point.

7.3 Experiments

7.3.1 Linear Measurements

As discussed in Chapter 2, like graphene, MoS_2 also has a polarisation-dependent absorption. However, it only absorbs light at the TE mode, does not affect the light at the TM mode, which is opposite to the feature of graphene. The stronger absorption of TE light is due to the positive value of the imaginary part of the dynamic conductivity of MoS_2, in agreement with previous reports [49, 51]. To compare its polarisation-dependent absorption with that of the graphene-based device, the linear transmission properties of the MoS_2-coated fibre device were characterised using the same setup as used in Chapter 5 (shown in Figure 5.10). A polarised CW source was used to probe the polarisation-dependent transmission of the device. The CW laser was kept at 1 mW to avoid any possible nonlinear effects and was free-space launched into the fibre device using a microscopic objective lens with $\sim$2 dB of coupling loss. The polarisation axis of the incident laser was tuned continuously by rotating a half-wave plate. The half-wave plate was rotated in steps of 5° to change the polarisation axis of the laser in steps of 10°. Additional measurements at 4°, 176°, 184° and 356° were taken due to the sharp change of the output power around 0° and 180°. An example polar plot of the transmitted power as a function of polarisation angle

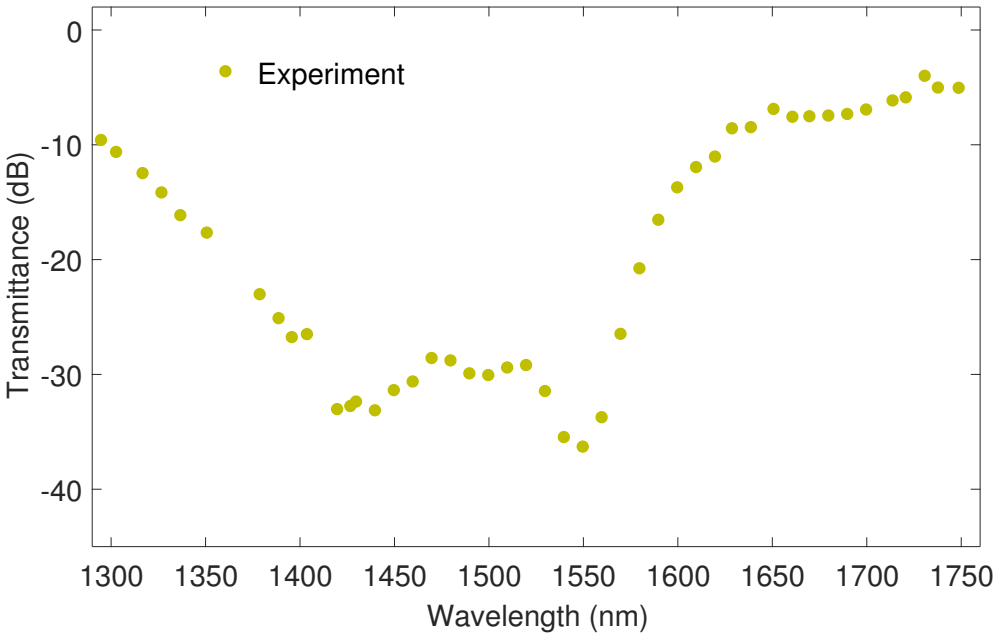

Figure 7.3: Measured transmittance spectrum of the MoS_2 device.

at 1550 nm is shown in Figure 7.2. It was found that the TE mode (0° and 180°) interacted more strongly with the MoS_2 layer (same as previously reported in [51]), giving an output power of around -33 dB. The output power for the TM mode coupling (90° and 270°) was around 2.5 dB, with almost no interaction between the mode and the MoS_2. Considering the 2 dB coupling loss, the high transmittance of the TM mode also proves that there is minimal insertion loss of the side-polished fibre itself.

Several other laser sources (Yenista Tunics T100S-E, T100S-SC, T100S-CLU; working wavelength coving 1300 to 1750 nm) were also used so that the absorption spectrum could be measured across a broad wavelength range. In these measurements, the polarisation was fixed so that the TE mode interacted with the over-layer materials. The wavelength was then tuned to obtain the transmission spectrum of the TE mode shown in Figure 7.3. The strong wavelength dependent interaction of the TE mode, with a -30 dB transmittance from 1410 nm to 1570 nm, suggests that there is resonant coupling between the fibre mode and the MoS_2 layer. This is in contrast with the previous measurements in graphene-based devices which exhibited a flat absorption behaviour (shown in Figure 5.12).

To further demonstrate the resonant coupling, a numerical study was undertaken using the FEM method discussed in Chapter 5. The simulation setup and most parameters are same as these in Figure 5.6 and Table 5.1. Only the refractive index of the MoS_2 is from

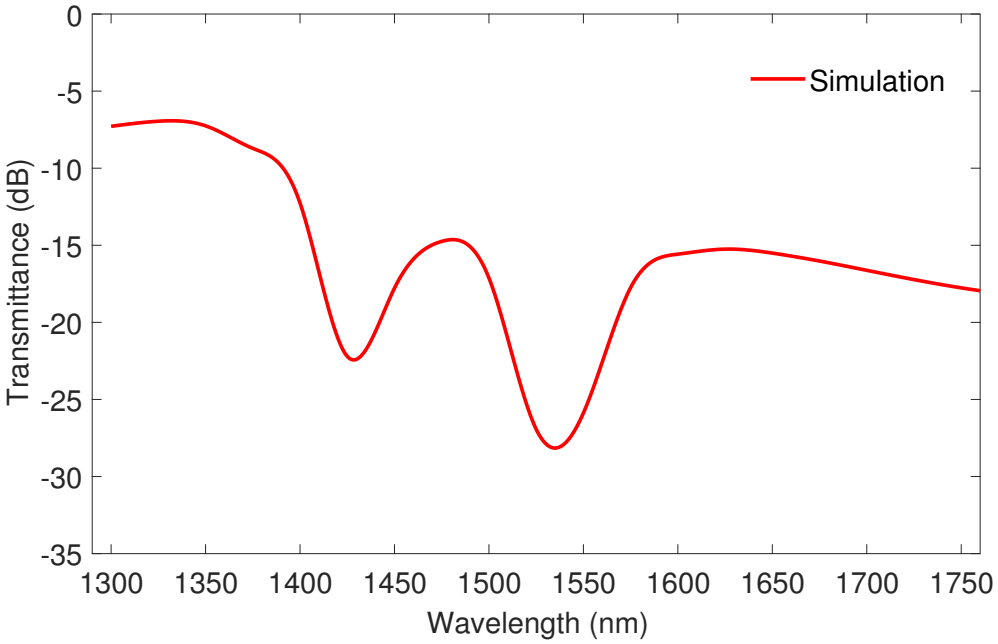

Figure 7.4: Simulated transmittance spectrum of the MoS_2 device.

Figure 4.8. The simulated transmittance of the TE mode is calculated using Equation 5.1 and 5.2 based on the effective refractive index given in the simulation results. Experiment results in Figure 7.3 indicates there are two resonant couplings peaks at around 1420 nm and 1540 nm. In order to match the double dip structure of the experimental curve, a slight variation in the film thickness across the 1 cm long MoS_2 sample was considered. The simulated transmittance of the TE mode shown in Figure 7.4 is merged from two simulation results at different thickness of the MoS_2 layer. The resonant couplings peaks at 1420 nm corresponds to a 10 μm MoS_2 layer thickness while the 1540 nm peak corresponds to a 13 μm thickness. The qualitative agreement with the experimental results indicates that there is indeed resonant coupling between the fibre mode and the MoS_2 layer, which could be optimized for access to different wavelength regions. Since the resonant peak is closely related to the thickness of the MoS_2 layer, the nonlinear enhancement could also be broadened to cover the entire telecoms band by using a MoS_2 film with a varying thickness. Also, additional simulations have shown that the resonant coupling is not related to the thickness of the PVB layer.

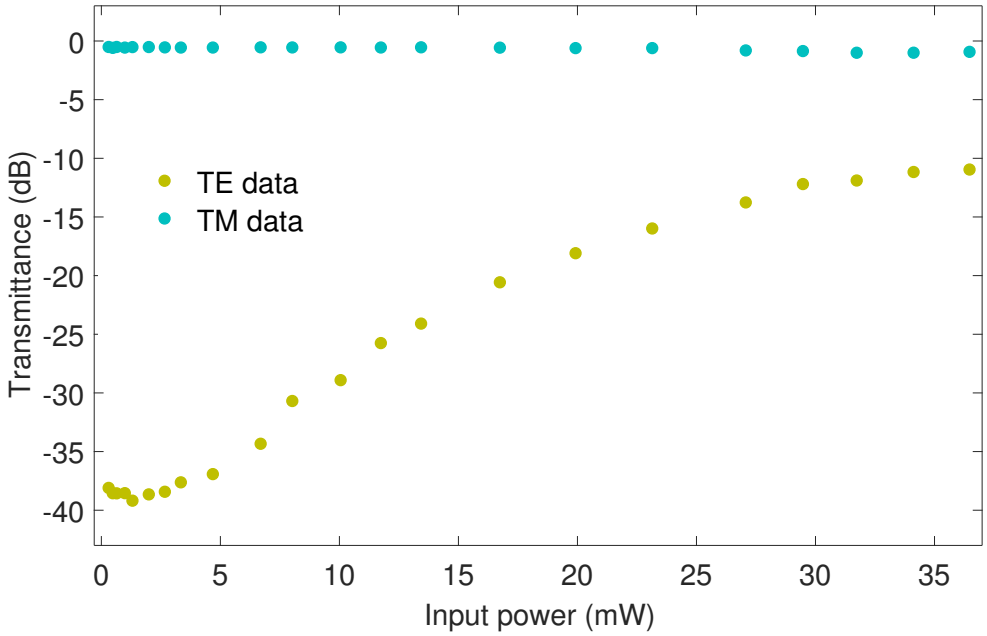

Figure 7.5: Non-linear saturable absorption curve at 1540 nm. Transmittance measurements of MoS_2 coated fibre device as a function of input average power P_{ave}.

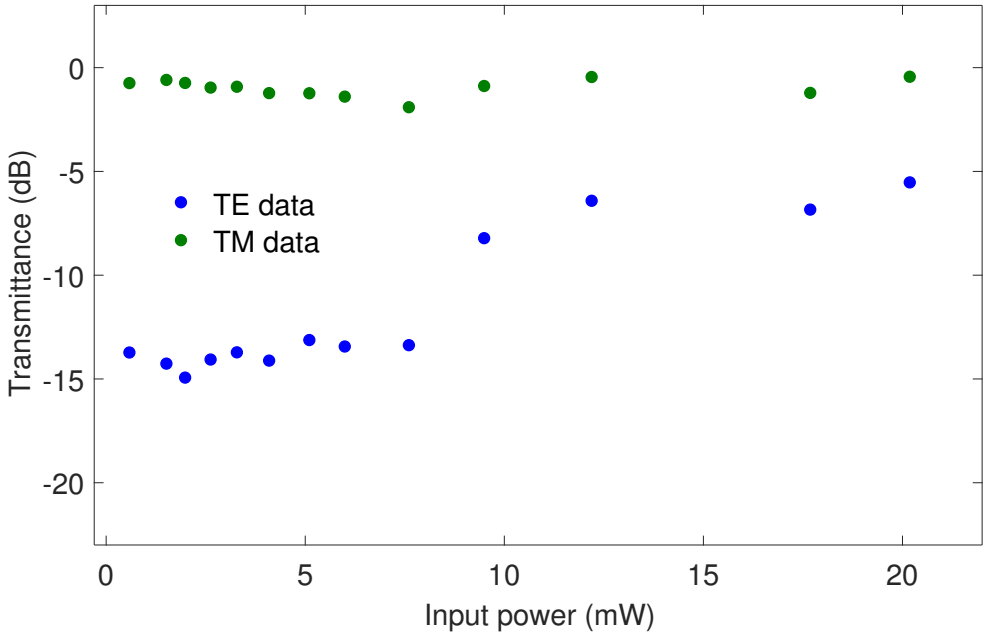

Figure 7.6: Non-linear saturable absorption curve at 1300 nm. Transmittance measurements of MoS_2 coated fibre device as a function of input average power P_{ave}.

7.3.2 Nonlinear Measurements

The resonant coupling between the polymer-coated-MoS_2 multi-layer and the core-guided mode strongly enhances light-MoS_2 interaction and nonlinear behaviours of the device. In order to investigate the nonlinear transmission characteristics when on resonance, the device was pumped with a low-noise femtosecond laser (Onefive Origami 15) using a same setup as used in the nonlinear measurements of the graphene-coated fibre (Figure 6.1). The centre wavelength of the laser is at 1540 nm, which is within the resonant wavelength range of the MoS_2 device. The output power of the laser was controlled using a variable optical attenuator and its polarization state was varied using a polarization controller. Figure 7.5 shows the transmittance of the TE and TM modes as a function of increasing average power, showing a clear onset of nonlinear saturable absorption of the TE mode. Specifically, up to $P_{ave} \sim 3\,\text{mW}$ the transmittance of the TE mode stays around $-38\,\text{dB}$. However, for higher input powers the absorption becomes nonlinear and the transmitted light starts to increase rapidly, eventually reaching a saturable transmittance of $-11\,\text{dB}$ for $P_{ave} \sim 36\,\text{mW}$, meaning a 27 dB change of the TE mode transmittance. In contrast, the transmission of the TM mode remains linear and changes less than 0.5 dB as there is minimal interaction between the TM mode and the MoS_2 sheet. The 27 dB change of the TE mode transmittance demonstrates a strong saturable absorption feature of the MoS_2 device at the resonance wavelength, which was not achieved in previous MoS_2-based devices (less than 3 dB transmittance change [121–124]). The saturable absorption of the MoS_2 device was also checked at non-resonance wavelength using the same setup. The transmittance of the TE and TM modes as a function of increasing average power at 1300 nm is shown in Figure 7.6. The maximum input power was around 20 mW due to the laser limitation. Since 1300 nm is out of the resonant wavelength region and the mode is smaller at 1300 nm, the TE mode transmittance change is much less compared to the results at 1540 nm, which further confirmed the resonance-enhanced non-linearities of the MoS_2 device.

7.3.3 Self-Phase Modulation Measurements

The nonlinear spectral properties of the device were examined using the same experimental set-up that was used for the saturable absorption characterisation. In this case the output

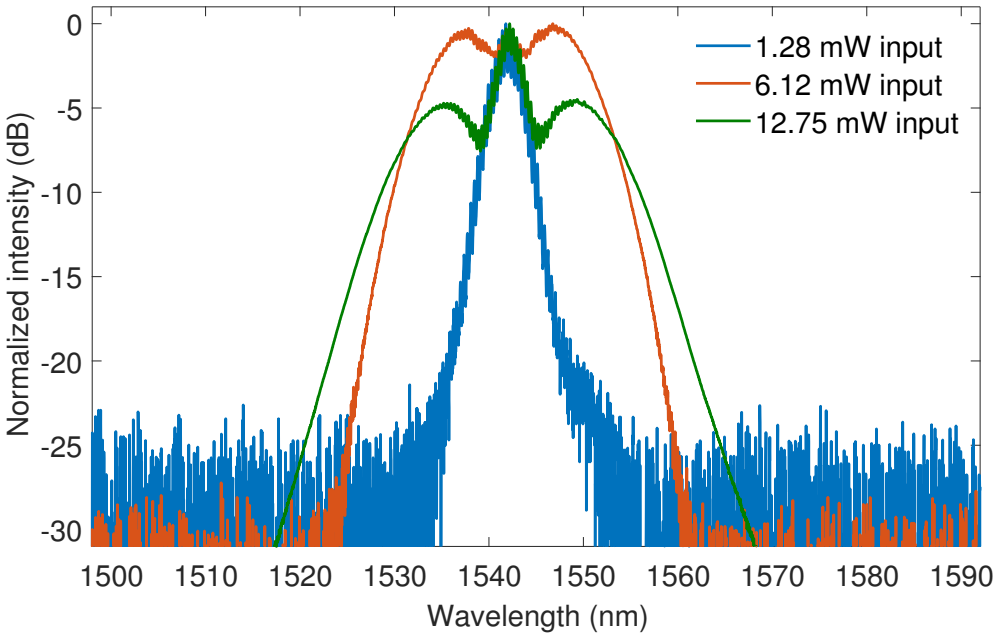

Figure 7.7: Output spectral response of the MoS_2 fibre device at different input average power.

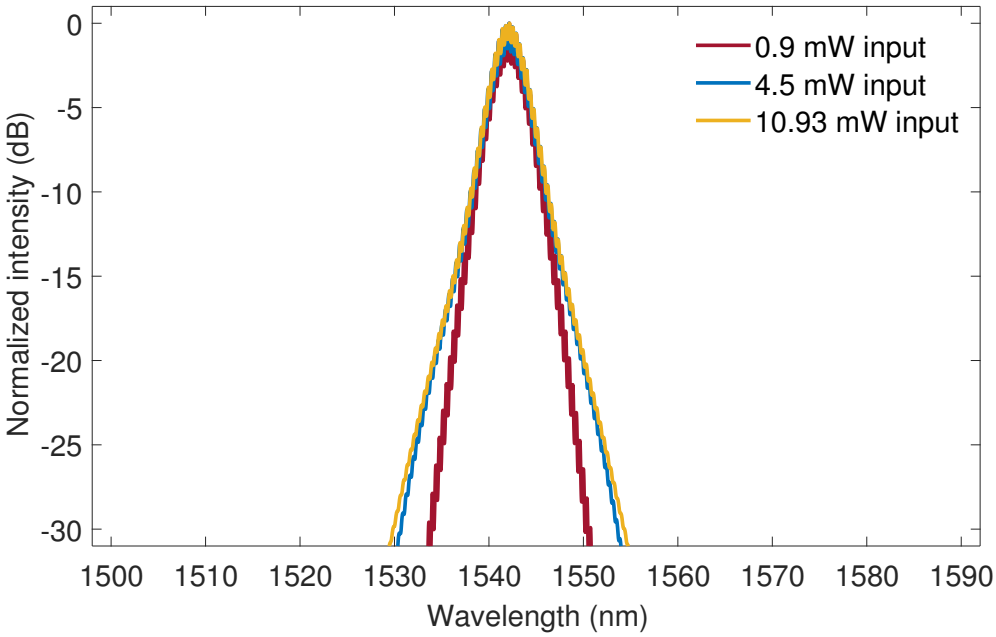

Figure 7.8: Output spectral response of the PVB-only coated fibre at different input average power.

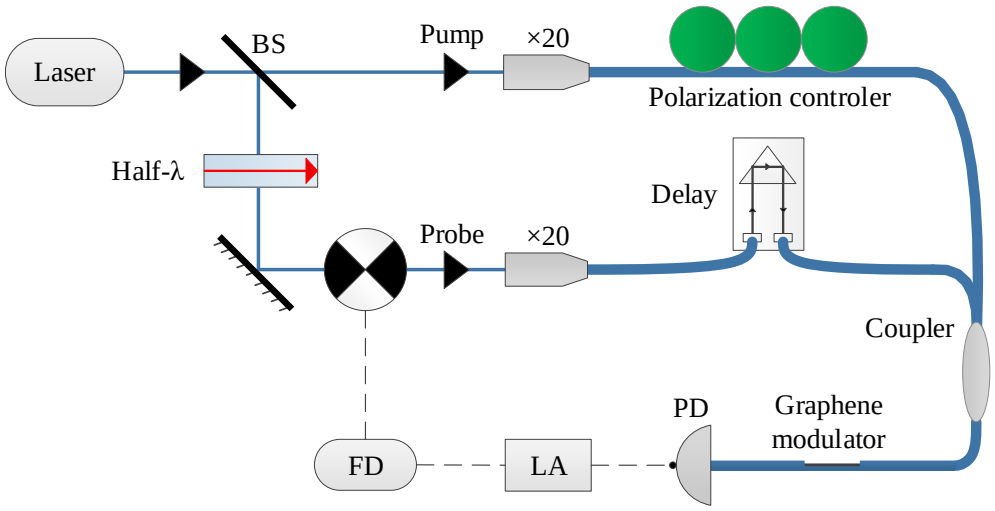

Figure 7.9: A schematic illustration of the experimental set-up used for pump-probe modulation. BS: beam splitter; FD: frequency driver; LA: lock-in amplifier; PD: photo-diode.

of the device was connected to an OSA and the output spectrum was recorded at different input powers. When the TE mode was coupled into the MoS_2, self-phase modulation-based spectral broadening occurred as the input power was increased. As shown in Figure 7.7, the output spectrum changes from 12 nm to 39 nm at -20 dB intensity level when the input power increases from 1.28 mW to 12.75 mW. This level of broadening (2.35 nm/mW) is remarkable considering the incredibly small volume of MoS_2 that the light is interacting with. In order to quantify the role of the highly nonlinear MoS_2 film, the size of the effective nonlinear coefficient (γ) in this section of the fibre is determined by fitting the spectral broadening with the nonlinear Schrodinger equation [125]. From this modeling, γ in the device is estimated to be around 1000 times larger than standard SMF, and about 30 times larger than highly nonlinear fibers such as small core microstructured designs [126,127]. A control experiment was also taken on a PVB-only-coated side-polished fibre. As shown in Figure 7.8, no obvious spectral broadening was observed when the TE mode input power increases from 0.9 mW to 10.93 mW. Additionally, when the TM mode was coupled into the MoS_2 fibre device and the PVB-only-coated fibre, no spectral broadening was observed.

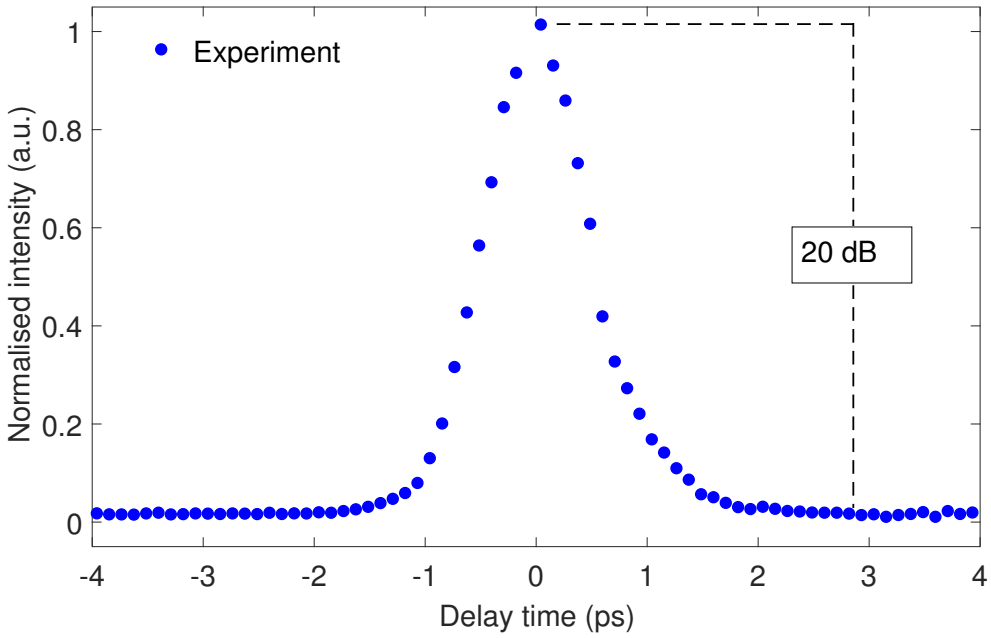

Figure 7.10: Measured nonlinear absorption of the weak probe pulse (blue dots).

7.3.4 All-Optical Modulation Measurements

The resonance-enhanced saturable absorption feature of MoS_2 indicates a potential to achieve an all-optical modulation with even higher modulation ratio compared to the graphene-based device. Thus, a further experiment was undertaken to test the suitability of the MoS_2 material for the development of high-speed all-optical modulators, similar to what has been achieved in graphene at Chapter 6. In this experiment, a time-resolved optical pump-probe technique was used to determine the fast temporal resolution of all-optical modulation in the PVB-coated-MoS_2 fibre device, using the set-up shown in Figure 7.9. The output beam of the fibre laser was split into a high power pump ($P_{ave} \sim 35.3$ mW, corresponding to a peak power of $P_p \sim 1105$ W) and a weak probe component ($P_{ave} \sim 711\ \mu$W, $P_p \sim 22$ W). The probe was modulated at 100 Hz using an optical chopper connected to a lock-in amplifier to discriminate between the two signals. Polarisation controllers were used to ensure that both the pump and probe were aligned to the TE mode so that they efficiently coupled into the MoS_2 layer. A 10 ps adjustable delay line was inserted into the path of the probe to control the temporal overlap of the two pulses. Figure 7.10 shows that the power of the transmitted probe signal can be modulated over a time-scale of 2 ps as the pump-probe overlap is tuned. A 20 dB modulation depth was achieved by comparing the maximum and minimum intensity of the probe single. Compared to the graphene-based

device, the higher modulation depth measured in the MoS_2 fibre device is believed due to the resonance-enhanced light-matter interaction within the telecoms band.

7.4 Summary

In conclusion, a MoS_2-based all-optical modulator with a high extinction ratio of 20 dB and a low loss of 0.5 dB has been designed and experimentally demonstrated in the telecoms band. The strong wavelength-dependent interaction measured in this device and the simulation results provide evidence of the resonance-enhanced light-matter interaction. Spectral broadening was also observed in the MoS_2 sheet, providing additional evidence of the strong light-matter interaction. When compared to the graphene-based device, a significant increase in modulation depth was realised due to the resonance-enhanced interaction. With further optimisation of the device design and the MoS_2 layer, this device may have potential to be used in wide-ranging nonlinear optical applications.

Chapter 8

Tunable Multi-Core to Single-Mode Fibre Coupler

8.1 Introduction

SDM systems based on MCFs have attracted much attention over the last years due to the high potential to overcome the capacity limit of a current optical communication system [128]. Although many important MCF devices have been demonstrated, including multi-core erbium doped fibre amplifiers [129], MCFs with reduced cross-talk [130], and spatial division multiplexers [131, 132], several of the key elements required to build a complete MCF network are still missing. In particular, one of the most ubiquitous components in fibre systems is the passive optical coupler, which is used to combine, split or monitor light within the system.

Single mode fibres polished by the novel side-polishing technique have been used as platforms to explore optical functionalities of 2D materials from Chapter 4 to Chapter 7. With access to the evanescent field escaping from the fibre core, these side-polished fibres can be also used in optical fibre couplers. To demonstrate the versatility of the polished fibre platform, in this chapter the side-polishing technique is extended to the multi-core optical fibre to demonstrate the first MCF to SMF coupler.

An optical fibre coupler is a device that is capable of dividing a single input into two or more outputs and combining two or more inputs into a single output [133]. Optical couplers can be used for combining, splitting or monitoring light within a fibre system

[134]. A typical four-port fibre coupler consists of two fibres that have been combined together for a small interaction region via fusing, etching, or polishing. Thus, a four-port coupler has three distinct regions: two input arms, an interaction region, and two output arms. In the interaction region, these two fibres are brought close enough so that the mode of one fibre can overlap with the mode of the other, allowing the transmission of light between the two fibres [133]. Today, the most common types of optical fibre couplers are fabricated using the fused biconical-tapering method, or, more specifically for MCFs, photonic lantern technologies, which is a technique that requires the several fibres to be held in contact whilst being drawn in a heat-source [135, 136]. However, when applied to MCFs, both of these methods result in simultaneous coupling to multiple cores, so that it is not possible to independently control the relative coupling [137]. The alternative is to make use of a side-polishing technique, where part of the cladding is removed from the MCF to allow access to the evanescent field of the desired core mode. Using this method it is straightforward to fabricate a four port coupler by placing two side-polished fibres in contact. Compared to their tapered counterparts, side-polished fibre couplers offer a number of advantages as they are mechanically robust, can be designed to operate over a broad wavelength region (several hundreds of nanometers), and can be continuously tuned by simply adjusting the evanescent field overlap [6].

In this chapter, a full characterisation of the coupler, including transmission losses and the tunability of the coupling ratio, will be discussed. Experimental results show that the coupler enables the splitting of light from a single core of the 7-core MCF, without disrupting the signal propagation in the remaining fibre cores. The coupler also exhibits a low insertion loss and a tunable coupling ratio over the entire telecommunications band. The author designed and conducted all the experiments in this chapter. Dr. Sonali Dasgupta conducted the coupling simulation with the assistance of the author.

8.2 Device Design and Fabrication

The MCF used in this work was designed so that the individual cores support single-mode operation across the telecoms band. As shown in Figure 8.1, the MCF consists of seven 8 μm diameter cores that are arranged in a hexagonal array with a 50 μm core-to-core pitch to limit crosstalk [138]. The resulting outer diameter of the MCF is 198 μm. The refrac-

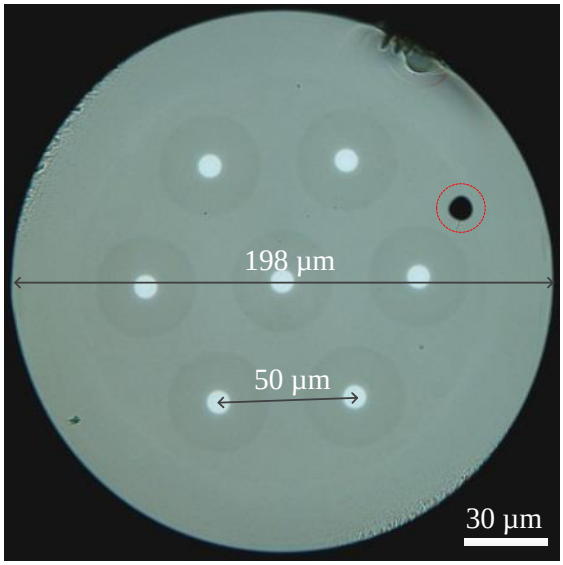

Figure 8.1: Microscope image of an unpolished MCF cross-section. Red circle: a marker for identification.

tive index contrast of the core/cladding is 0.36 % for both the MCF and the SMF. Prior to polishing, the MCF was stripped of its acrylic coating and mounted in a aluminium polishing block (same as used in Chapter 3) that helps to maintain its mechanical stability, both during and after the processing. To ensure that the polishing plane of the MCF allowed access to just one core, a red light source was coupled into the fibre during the mounting process and the orientation checked by monitoring the output pattern. A portion of the MCF cladding material was then removed from the mounted fibre using the technique described in Chapter 3. The distance between the MCF core and the polished surface was chosen to permit access to more than 30 dB of the light propagating through the target core without introducing additional loss. The coupling length of $\sim$1 cm was chosen to allow for controllable and efficient coupling between the two fibres, though the polishing process can be easily adapted for either longer or shorter lengths.

Figure 8.2(a) shows a cross-sectional image of a polished MCF that has been optimized for coupling to and from a single core. The coupler was then formed by mating the respective polishing blocks, thus bringing the relevant cores into the proximity required to achieve evanescent coupling. Coupling is realised throughout the interaction region by the interference of the two relevant modes and optical power is transferred between the two fibre cores. Figure 8.2(b) shows a schematic image of the coupler cross-section illustrating the geometry and orientation of the polished fibres. To specify the performance of an

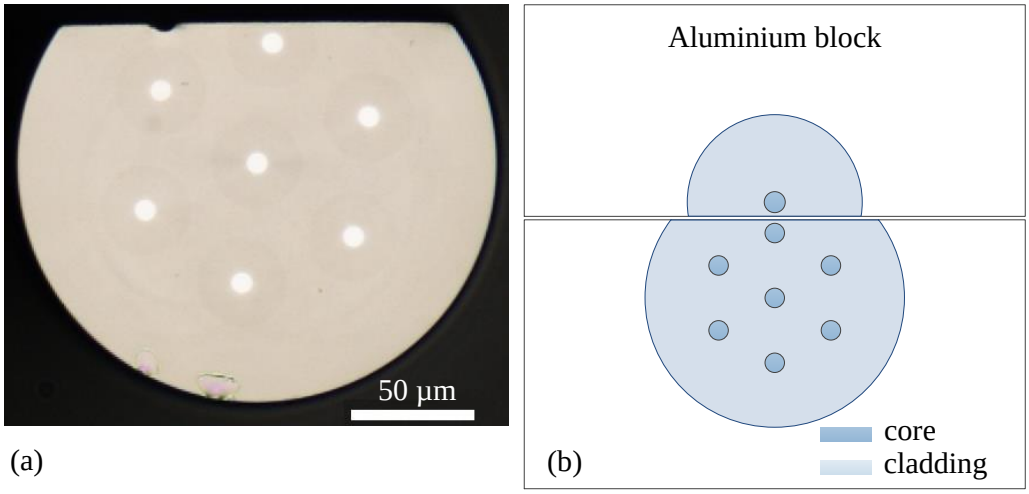

Figure 8.2: (a) Microscope image of the polished MCF cross-section. The dip on the top surface is due to the marker for identification (see Figure 8.1). (b) Schematic of the mated coupling blocks.

optical coupler, the coupling ratio CR, which indicates the splitting percentage of optical power between the output ports, is calculated using the following equation [3]:

$$CR = \frac{P_1}{P_1 + P_2} \tag{8.1}$$

where P_1 is the measured coupled power at the first output and P_2 is measured remaining power at the second output.

To prove that only the power in the target core is affected while the signal propagation in the remaining fibre cores was not disrupted, microscope images of a polished MCF cross-section are compared before and after dropping a high refractive index liquid onto the polished region above the target core. As shown in Figure 8.3 (a) and (b), only the marked target core has a power transmission drop while the other cores are not affected.

8.3 Experiment Setup

Positioning of the polished fibres and optimization of the coupling was achieved by holding the polished SMF block in a fixed assembly and mounting the second MCF block in a kinematic mount with sub-micron positioning accuracy, as shown in Figure 8.4. The kinematic mount was also used to adjust the position of the fibres with respect to each other so

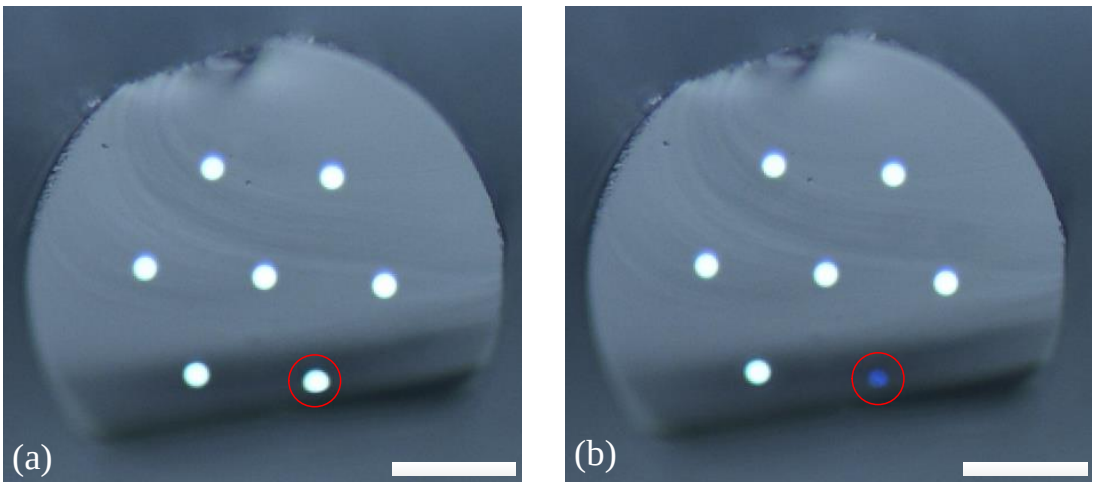

Figure 8.3: Microscope images of a polished MCF cross-section before (a) and after (b) dropping a high refractive index liquid on the polished surface. The target core is marked by a red circle. Scale bar: 50 μm.

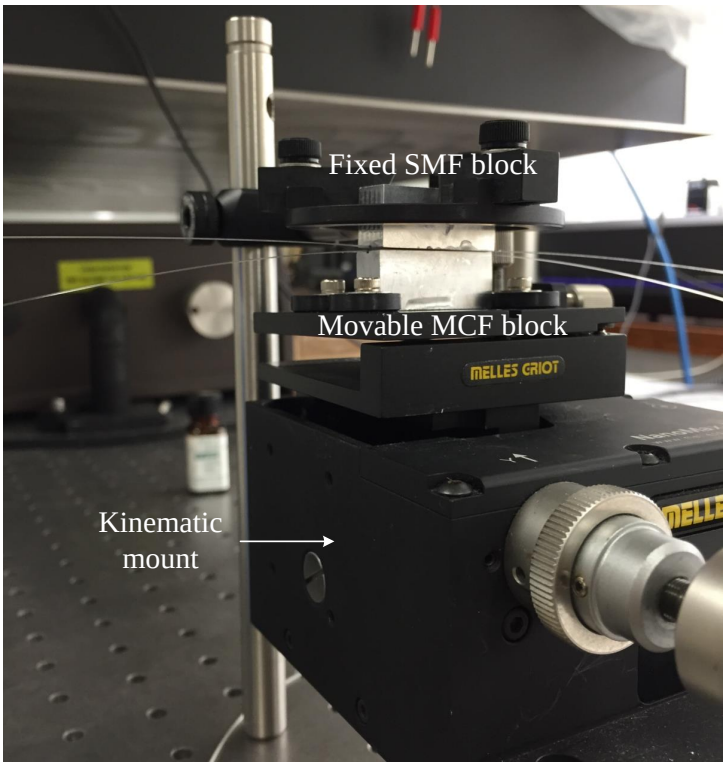

Figure 8.4: Experiment image of the kinematic mount fitted with MCF and SMF blocks.

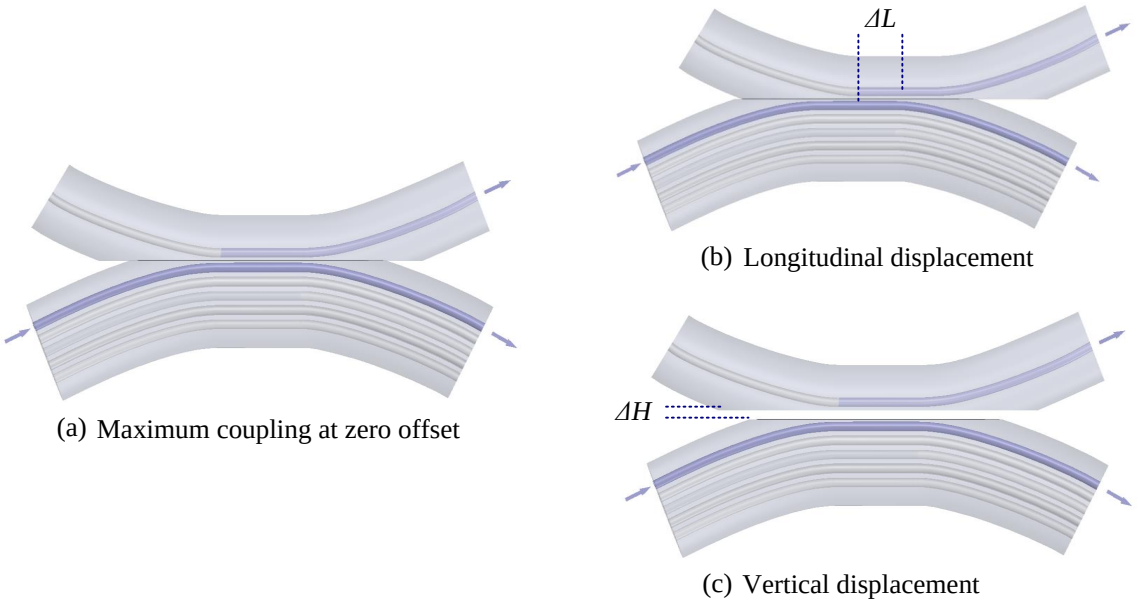

(a) Maximum coupling at zero offset

(b) Longitudinal displacement

(c) Vertical displacement

Figure 8.5: (a) Illustration of the multi-core to single-mode fibre coupler position for maximum coupling. Arrows show the flow of light into and out of the device. Schematics showing (b) longitudinal and (c) vertical adjustments of the coupling ratio.

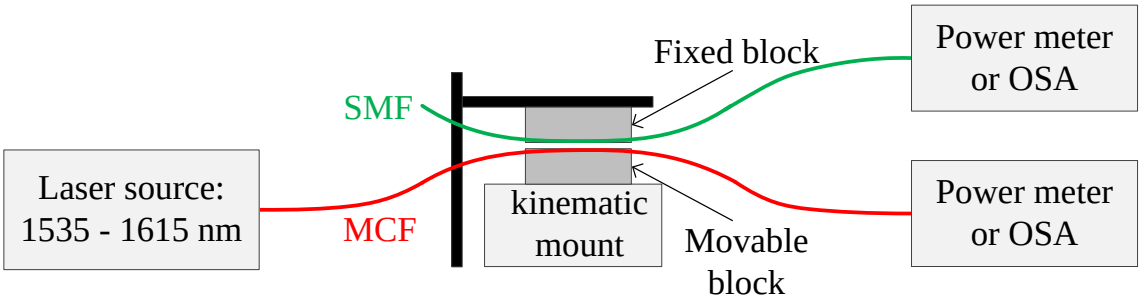

Figure 8.6: Experimental configuration for the coupler transmission measurements.

that the coupling ratio could be tuned by longitudinally or vertically displacing the relative positions of the fibres, as shown in Figure 8.5, which amounts to changing the effective coupling length and coupling strength, respectively. The relative position is quantified by calculating the longitudinal or vertical distance travelled by the kinematic mount. A liquid with a refractive index equal to the fibre cladding ($n \sim 1.4468$) was applied to the polished surface to improve the coupling efficiency and lubricate the surfaces of the optical fibres [139]. An amplified spontaneous emission (ASE) source was used to generate a broadband input signal (1535 to 1615 nm). A power meter (Thorlabs PM 100D) and an OSA (Yokogawa AQ6370) were used to check the two output signals, as shown in Figure 8.6 .

8.4 Experiment Results

8.4.1 Transmission Loss

By adjusting the movable block with the kinematic mount and monitoring the output power of the single-mode and multi-core fibres, a maximum coupling percentage of $\sim$33 % was obtained for the telecommunication wavelength 1550 nm, and this coupling position was fixed as the zero offset for the remaining measurements. The throughput loss for this device at the zero offset was estimated by comparing the total output power from both fibres to the input power. Figure 8.7 shows the results obtained across the entire spectral band, where it can be seen that the losses vary by less than 10% around the value of $\sim$ 1 dB. The low loss of this coupler is attributed both to the ultra-smooth surface (nanometer-scale roughness) and the adiabatic transmission from the full fibre to the coupling region. The index matching liquid, which lubricates the fibre surfaces, also helps to reduce the transmission loss of $\sim$2 dB. A polarisation dependent transmission measurement was also conducted, where the polarisation state of the input light was changed and the power in the two output arms was monitored. No polarisation dependent loss was observed in the side-polished fibre coupler during this experiment.

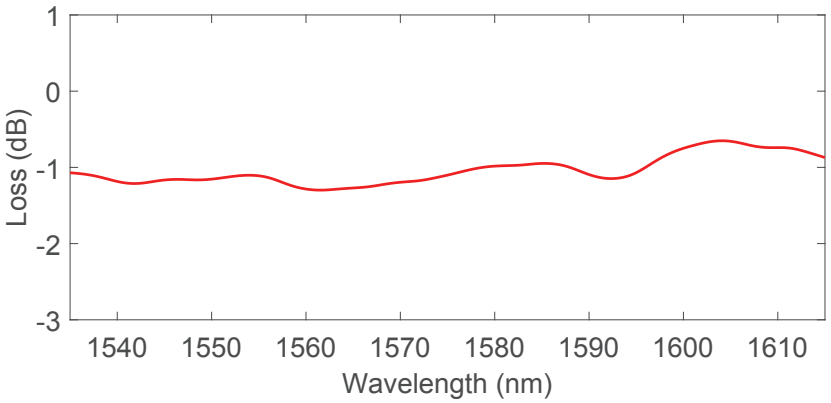

Figure 8.7: Spectral response of the throughput loss when set at the maximum coupling for an operation wavelength of 1550 nm.

8.4.2 Coupling Ratio Alteration via Lateral Displacement

The spectral response of the MCF-SMF coupler at the zero offset was then measured using the ASE source and monitoring the output on an optical spectrum analyser across the wavelength range $1535 - 1615$ nm. The results of this measurement are shown as the top curve ($0\,\mu$m) in Figure 8.8, where it can be seen that the coupled power only varies by 10 % over the spectral range, i.e. the entire telecommunications C-band. The variation is because coupling increases with increasing wavelength, which can be explained by the higher evanescent field of the longer wavelengths. This measurement was then repeated for different coupling lengths by adjusting the longitudinal displacement $\triangle L$ in intervals of $\sim 15\,\mu$m, as illustrated in Figure 8.5(b). As expected, reducing the interaction length reduced the coupled power at each wavelength correspondingly, so that the device retained its spectral flatness. These results serve to highlight the excellent broadband nature of this type of coupler.

8.4.3 Coupling Ratio Alteration via Vertical Displacement

To demonstrate tunability of the coupler, our next set of measurements investigated the effect of altering the coupling strength by vertically displacing the SMF, as shown in Figure 8.5(c). Starting from the zero offset position, the core to core spacing $\triangle H$ was increased in steps of 600 nm, thus decreasing the modal overlap. Data points in Figure 8.9 shows the measured change in coupled power relative to the displacement $\triangle H$ for two wavelengths, 1550 nm (triangles) and 1600 nm (circles). These results show the expected trend

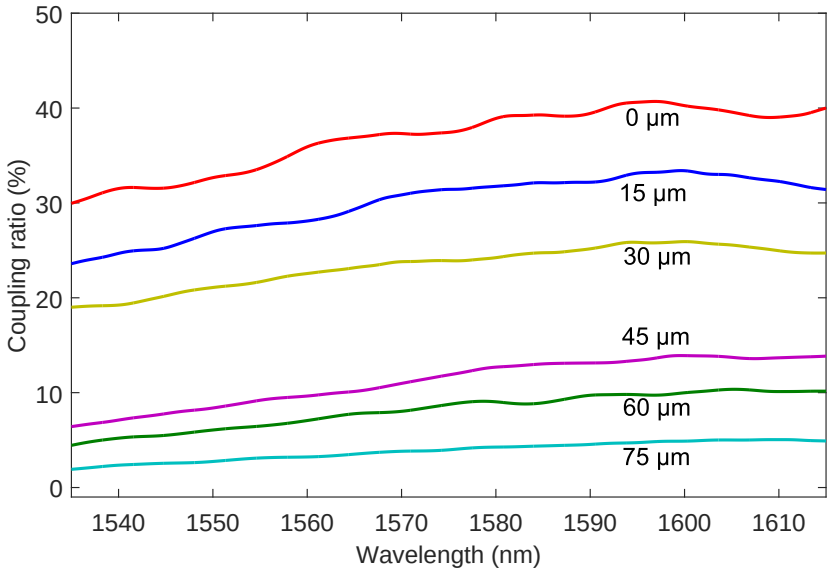

Figure 8.8: Spectral response of the coupler for different longitudinal tunings $\triangle L$, in increments of $\sim 15\,\mu$m.

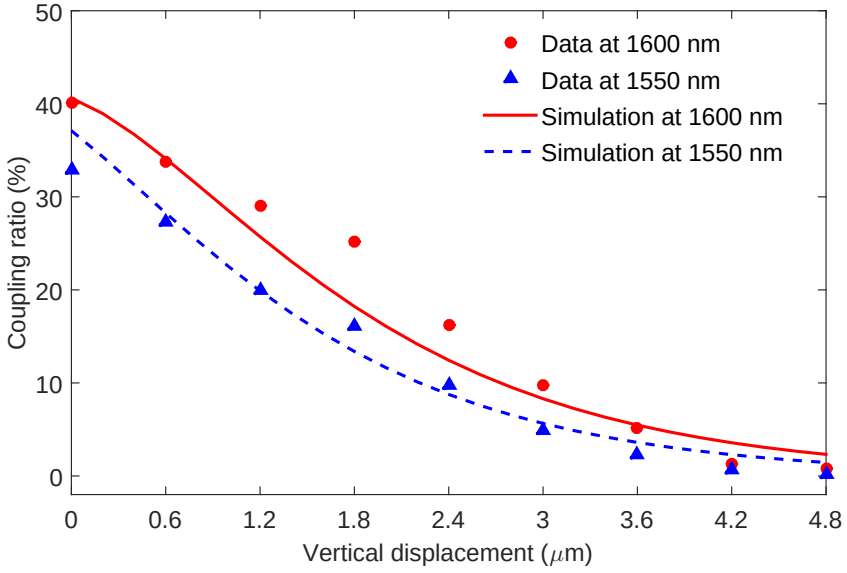

Figure 8.9: Coupling throughput as a function of vertical displacement $\triangle H$ at wavelengths of 1550 nm (triangles) and 1600 nm (circles). The fitted curves are the numerical simulations at 1550 nm (dashed) and 1600 nm (solid).

of decreasing coupling ratio with increasing core to core spacing. Due to the nature of the evanescent coupling condition, the coupling ratio decreases much faster for vertical displacements than for longitudinal displacements of the same size (vertical: decrease exponentially; lateral: decrease linearly). Also, since the coupling strength depends on the overlap integral between the modal fields of the core modes of the coupler, which is proportional to the light's wavelength, the initial coupling ratio is slightly higher for the longer wavelength, in agreement with the results in Figure 8.8, but drops rapidly for $\triangle H > 3$ μm. Noticeably, in both cases, the rate of decrease in the coupling was slightly slower than the expected exponential rate for two identical fibre cores, thereby suggesting the MCF-SMF coupler is slightly asymmetric. To further investigate this asymmetry, a numerical simulation was conducted in Section 8.5.

8.5 Numerical Simulation of MCF to SMF Coupling

In the experiment results, the minimum coupling ratio is less than 2% for both the vertical and lateral separations, and the transmission loss at the zero offset is less than 1 dB, which suggest a good coupling between the two fibres. For a symmetry coupling system, in which the two constituent fibre cores are identical, if the minimum coupling ratio is low and the transmission loss is also low, then the maximum coupling should consequently be high, i.e. tend towards 100%. But in our experimental results, the maximum coupling ratio achieved at the zero offset is less than 40% over the entire transmission band, thereby suggesting that the coupler is asymmetric. In terms of phase mismatch, asymmetric couplers are those in which the two constituent fibre cores are dissimilar. To investigate this further, the system was modelled using the well-known coupled mode theory [140] by Dr. Sonali Dasgupta with the assistance of the author.

Iterative simulations were performed to obtain the best match to the experimental results, starting with a symmetric coupler system comprising of two single-mode fibres, and then gradually introducing asymmetry in the geometrical parameters. Mismatch between the refractive index profiles of the multi-core and single-mode fibres was ruled out following refractive index profile measurements, indicating that any discrepancy should be in the core size. From the best fit simulations, it is found that there is most likely a small difference of $\sim$2% between the core radii of the multi-core and single-mode fibres, which is

reasonable considering that the core diameter of SMF-28 is typically around 8.2 μm (i.e., 2 % larger than our MCF cores). Thus, the maximum coupling of less than $\sim$40 % at the entire transmission band in Figure 8.8 can now be understood as a limitation imposed by the asymmetry in the coupler system in which there is a slight mismatch in the propagation constants of the fundamental modes in each fibre. This core mismatch means that it is not possible to achieve 100 % coupling for this system, but this could easily be addressed through careful selection of the starting fibres. Overall, the observed trends in the experimental measurements match well with the simulation results for most displacements in Figure 8.9. Both experimental results in Section 8.4.3 and simulations in this section show there is a core size mismatch between the multi-core and single-mode fibres, thus, further loss reduction may be possible with identical core sizes (as low as < 0.5 dB loss has been realised using the same polishing technique with two SMFs).

8.6 Conclusion

In this chapter, a MCF to SMF coupler is demonstrated using the side-polishing technique. By removing parts of the cladding region of a MCF and a SMF fibre, effective evanescent field coupling was achieved to realize a tunable multi-core to single-mode fibre coupler. By controlling the fibre core separation via micro-positioning, the coupling ratio can be smoothly and continuously tuned. Experiment characterizations show the maximum coupling ratio is around 40% at the zero offset and the transmission loss of the device is as low as 1 dB. Simulation results have confirmed this relatively low coupling ratio is due to a slight different in the core diameters of the MCF and SMF fibres. The experiment results are in good agreement with numerical simulations, which confirm the high precision of our fabrication approach. Polished fibre couplers offer key benefits in that they offer low loss, are capable of operating over a broad bandwidth, and can be tuned continuously using simple displacement methods. As in the case of the standard polished SMF coupler, the coupling characteristics of our MCF device, such as the spectral response and the coupling ratio, can be varied quite dramatically by altering the polishing depth and interaction length for the two fibres.

Chapter 9

Conclusions

In recent years, side-polished fibre devices have been revisited in an attempt to meet the need for miniature, multifunctional, and sensitive device platforms [141]. My research project sets out to investigate the potential for this technology to be used with new materials to produce new devices with new functionality. In this final chapter, I will review my research work shown in this thesis.

9.1 Thesis Conclusions

In this dissertation, a novel method for producing side-polished fibres that enable strong light-matter interaction while keeping ultra-low insertion loss has been developed. After trying different polishing blocks, an aluminium block with a curved U-groove was used to bond fibres during polishing processes. Three types of polishing papers with different abrasive sizes were used in the fibre polishing to get a best combination of polishing speed and surface quality. Using this polishing method, side-polished fibres with ultra-smooth and flat surfaces were achieved. Optical measurements show that the polished fibres have negligible transmission losses across a broad wavelength range due to the ultra-smooth polished surface and the adiabatic transition design.

The side-polished fibre platform has been utilized for the development of photonic devices that incorporate some of the most popular 2D materials, including graphene and MoS_2. By coating graphene onto the window of the side-polished fibre, a high-performance graphene-based fibre polariser was fabricated and characterised. A high index PVB over-

layer was applied onto the graphene film to enhance the light-graphene interaction, which was demonstrated both theoretically and experimentally. Characterization of the graphene-based fibre polariser shows a high extinction ratio of $\sim$37.5 dB and a low device loss of $\sim$1 dB, which is an order of magnitude improvement in performance over any previously reported fibre-based graphene polarisers. The broadband nature of our device was confirmed by characterisation across the wavelength range 1425-1600 nm and an additional test at 2000 nm. The experimental results are in good agreement with the numerical investigations, which highlight the usefulness of these side-polished fibres as templates for the integration of other low-dimensional materials.

The graphene-based fibre device was also demonstrated for use as an all-optical modulator. Nonlinear absorption measurements showed a $\sim$17 dB variation in the transmission of the TM mode, highlighting the possibility for high modulation depth. A pump-probe experiment verified that the modulation had an extinction ratio as high as 9 dB and operation bandwidth of 0.5 THz, indicating a FOM of 9 which is greater than the previous best result.

A MoS_2-based all-optical modulator was also demonstrated based on the similar design as the graphene-based device. A significant increase in modulation depth was achieved when compared to the graphene-based device. A strong wavelength-dependent interaction was measured in this device, which was believed to be due to the resonance-enhanced light-matter interaction. Spectral broadening via self-phase modulation was also observed in the MoS_2-based device. With further optimization of the device design and number of material layers, this device may be used in wide-ranging nonlinear optical applications.

As these 2D material-based devices are built into a side-polished optical fibre, it is also extremely robust, stable and is immediately compatible with existing fibre networks. Owing to the combination of low losses and high extinction ratios, these results represent a key step towards the practical integration of low-dimensional materials with traditional optical fibres. Furthermore, it can be packaged using methods that are well-established for existing fibre devices, enabling immediate compatibility with standard infrastructures. Also, this method for enhancing light-matter interactions could be easily transferred to other two-dimensional materials to realize fictionalized side-polished fibre devices that are capable of generating, modulating, and detecting light in next generation all-fibre opto-electronic systems.

Other than these 2D material-based devices, the side-polishing technique has also been used to develop a low loss, wide-band multi-core to single-mode fibre coupler, which enables light access from a single core of the multi-core fibre without disrupting the signal propagation in the remaining cores. By using the same polishing method, effective evanescent field coupling was achieved between the multi-core and the single-mode fibres. The coupling ratio could be smoothly and continuously tuned by controlling the fibre core separation via micro-positioning, such as altering the polishing depth or interaction length for the two fibres. A coupling ratio as high as 40% and a transmission loss of 1 dB was achieved across a broadband wavelength range. This relatively low maximum coupling was attributed to an asymmetry in the core diameters of the multi-core and single-mode fibres. The robust and low loss couplers are expected to form a critical component of future MCF networks, providing lateral access to the propagating light for monitoring, splitting and multiplexing applications in a spatially controlled manner. Furthermore, it would also be possible to replace the SMF in this coupler with a second MCF to expand the potential application scenarios.

Bibliography

[1] J. M. Lopez-Higuera, *Handbook of optical fibre sensing technology*. Wiley, 2002.

[2] J. Dakin and B. Culshaw, "Optical fiber sensors: Principles and components. volume 1," *Boston, MA, Artech House, 1988, 343 p. For individual items see A90-36770 to A90-36775.*, vol. 1, 1988.

[3] J. Zhang, *Optical side-polished fiber coupler: design and fabrication*. PhD thesis, Concordia University, 2006.

[4] S. F. Silva, L. Coelho, O. Frazão, J. L. Santos, and F. X. Malcata, "A review of palladium-based fiber-optic sensors for molecular hydrogen detection," *IEEE Sensors Journal*, vol. 12, no. 1, pp. 93–102, 2012.

[5] R. Bergh, G. Kotler, and H. Shaw, "Single-mode fibre optic directional coupler," *Electronics Letters*, vol. 16, no. 7, pp. 260–261, 1980.

[6] H. Kim, J. Kim, U.-C. Paek, B. H. Lee, and K. T. Kim, "Tunable photonic crystal fiber coupler based on a side-polishing technique," *Optics Letters*, vol. 29, no. 11, pp. 1194–1196, 2004.

[7] R. Slavik, J. Homola, J. Ctyroky, and E. Brynda, "Novel spectral fiber optic sensor based on surface plasmon resonance," *Sensors and Actuators B: Chemical*, vol. 74, no. 1, pp. 106–111, 2001.

[8] Q. Bao, H. Zhang, B. Wang, Z. Ni, C. H. Y. X. Lim, Y. Wang, D. Y. Tang, and K. P. Loh, "Broadband graphene polarizer," *Nature Photonics*, vol. 5, no. 7, pp. 411–415, 2011.

[9] W.-G. Jung, S.-W. Kim, K.-T. Kim, E.-S. Kim, and S.-W. Kang, "High-sensitivity temperature sensor using a side-polished single-mode fiber covered with the polymer planar waveguide," *IEEE Photonics Technology Letters*, vol. 13, no. 11, pp. 1209–1211, 2001.

[10] N. K. Sharma and B. Gupta, "Fabrication and characterization of ph sensor based on side polished single mode optical fiber," *Optics Communications*, vol. 216, no. 4, pp. 299–303, 2003.

[11] A. C. Neto, F. Guinea, N. M. Peres, K. S. Novoselov, and A. K. Geim, "The electronic properties of graphene," *Reviews of Modern Physics*, vol. 81, no. 1, p. 109, 2009.

[12] Q. Bao and K. P. Loh, "Graphene photonics, plasmonics, and broadband optoelectronic devices," *ACS Nano*, vol. 6, no. 5, pp. 3677–3694, 2012.

[13] M. Feng, H. Zhan, and Y. Chen, "Nonlinear optical and optical limiting properties of graphene families," *Applied Physics Letters*, vol. 96, no. 3, p. 033107, 2010.

[14] Y. Wu, B. Yao, Q. Feng, X. Cao, X. Zhou, Y. Rao, Y. Gong, W. Zhang, Z. Wang, Y. Chen, *et al.*, "Generation of cascaded four-wave-mixing with graphene-coated microfiber," *Photonics Research*, vol. 3, no. 2, pp. A64–A68, 2015.

[15] M. Liu, X. Yin, E. Ulin-Avila, B. Geng, T. Zentgraf, L. Ju, F. Wang, and X. Zhang, "A graphene-based broadband optical modulator," *Nature*, vol. 474, no. 7349, pp. 64–67, 2011.

[16] D. Popa, Z. Sun, T. Hasan, F. Torrisi, F. Wang, and A. Ferrari, "Graphene q-switched, tunable fiber laser," *Applied Physics Letters*, vol. 98, no. 7, p. 3106, 2011.

[17] H. Zhang, D. Tang, L. Zhao, Q. Bao, and K. Loh, "Large energy mode locking of an erbium-doped fiber laser with atomic layer graphene," *Optics Express*, vol. 17, no. 20, pp. 17630–17635, 2009.

[18] F. Xia, T. Mueller, R. Golizadeh-Mojarad, M. Freitag, Y.-m. Lin, J. Tsang, V. Perebeinos, and P. Avouris, "Photocurrent imaging and efficient photon detection in a graphene transistor," *Nano Letters*, vol. 9, no. 3, pp. 1039–1044, 2009.

[19] K.-K. Liu, W. Zhang, Y.-H. Lee, Y.-C. Lin, M.-T. Chang, C.-Y. Su, C.-S. Chang, H. Li, Y. Shi, H. Zhang, *et al.*, "Growth of large-area and highly crystalline mos2 thin layers on insulating substrates," *Nano Letters*, vol. 12, no. 3, pp. 1538–1544, 2012.

[20] A. Shmeliov, M. Shannon, P. Wang, J. S. Kim, E. Okunishi, P. D. Nellist, K. Dolui, S. Sanvito, and V. Nicolosi, "Unusual stacking variations in liquid-phase exfoliated transition metal dichalcogenides," *ACS Nano*, vol. 8, no. 4, pp. 3690–3699, 2014.

[21] K. F. Mak, C. Lee, J. Hone, J. Shan, and T. F. Heinz, "Atomically thin mos 2: a new direct-gap semiconductor," *Physical Review Letters*, vol. 105, no. 13, p. 136805, 2010.

[22] D. Krasnozhon, D. Lembke, C. Nyffeler, Y. Leblebici, and A. Kis, "Mos2 transistors operating at gigahertz frequencies," *Nano Lett.*, vol. 14, no. 10, pp. 5905–5911, 2014.

[23] F. K. Perkins, A. L. Friedman, E. Cobas, P. Campbell, G. Jernigan, and B. T. Jonker, "Chemical vapor sensing with monolayer mos2," *Nano Lett.*, vol. 13, no. 2, pp. 668–673, 2013.

[24] R. Wang, H.-C. Chien, J. Kumar, N. Kumar, H.-Y. Chiu, and H. Zhao, "Third-harmonic generation in ultrathin films of mos2," *Appl. Mater. Interfaces*, vol. 6, no. 1, pp. 314–318, 2013.

[25] K. Wang, J. Wang, J. Fan, M. Lotya, A. ONeill, D. Fox, Y. Feng, X. Zhang, B. Jiang, Q. Zhao, *et al.*, "Ultrafast saturable absorption of two-dimensional mos2 nanosheets," *ACS Nano*, vol. 7, no. 10, pp. 9260–9267, 2013.

[26] S. Wang, H. Yu, H. Zhang, A. Wang, M. Zhao, Y. Chen, L. Mei, and J. Wang, "Broadband few-layer mos2 saturable absorbers," *Advanced Materials*, vol. 26, no. 21, pp. 3538–3544, 2014.

[27] J. Du, Q. Wang, G. Jiang, C. Xu, C. Zhao, Y. Xiang, Y. Chen, S. Wen, and H. Zhang, "Ytterbium-doped fiber laser passively mode locked by few-layer molybdenum disulfide (mos2) saturable absorber functioned with evanescent field interaction," *Sci. Rep.*, vol. 4, p. 6346, 2014.

[28] R. Woodward, E. Kelleher, R. Howe, G. Hu, F. Torrisi, T. Hasan, S. Popov, and J. Taylor, "Tunable q-switched fiber laser based on saturable edge-state absorption in few-layer molybdenum disulfide (mos 2)," *Opt. Express*, vol. 22, no. 25, pp. 31113–31122, 2014.

[29] D. J. Richardson *et al.*, "Space-division multiplexing in optical fibres," *Nature Photon.*, vol. 7, no. 5, pp. 354–362, 2013.

[30] S. Matsuo, Y. Sasaki, I. Ishida, K. Takenaga, K. Saitoh, and M. Koshiba, "Recent progress on multi-core fiber and few-mode fiber," in *Optical Fiber Communication Conference and Exposition and the National Fiber Optic Engineers Conference (OFC/NFOEC), 2013*, pp. 1–3, IEEE, 2013.

[31] T. Hayashi, T. Taru, O. Shimakawa, T. Sasaki, and E. Sasaoka, "Design and fabrication of ultra-low crosstalk and low-loss multi-core fiber," *Optics Express*, vol. 19, no. 17, pp. 16576–16592, 2011.

[32] T. Hayashi, R. Ryf, N. K. Fontaine, C. Xia, S. Randel, R.-J. Essiambre, P. J. Winzer, and T. Sasaki, "Coupled-core multi-core fibers: High-spatial-density optical transmission fibers with low differential modal properties," in *Optical Communication (ECOC), 2015 European Conference on*, pp. 1–3, IEEE, 2015.

[33] C. Xia, N. Bai, I. Ozdur, X. Zhou, and G. Li, "Supermodes for optical transmission," *Optics Express*, vol. 19, no. 17, pp. 16653–16664, 2011.

[34] G. Keiser, *Optical fiber communications*. Wiley Online Library, 2003.

[35] D. Gloge, "Weakly guiding fibers," *Applied Optics*, vol. 10, no. 10, pp. 2252–2258, 1971.

[36] A. Ghatak and K. Thyagarajan, *An introduction to fiber optics*. Cambridge university press, 1998.

[37] K. Okamoto, *Fundamentals of optical waveguides*. Academic Press, 2010.

[38] A. W. Snyder and J. Love, *Optical waveguide theory*. Springer Science & Business Media, 2012.

[39] M. Rabeh, A. Samra, and M. Abouheaf, "Evanescent wave coupling between optical fiber and planar optical waveguide," in *Radio Science Conference, 2006. NRSC 2006. Proceedings of the Twenty Third National*, pp. 1–6, IEEE, 2006.

[40] W.-P. Huang, "Coupled-mode theory for optical waveguides: an overview," *JOSA A*, vol. 11, no. 3, pp. 963–983, 1994.

[41] H. Haus, "Coupled-mode theory revisited," in *Cambridge Symposium-Fiber/LASE'86*, pp. 68–78, International Society for Optics and Photonics, 1987.

[42] P. R. Wallace, "The band theory of graphite," *Physical Review*, vol. 71, no. 9, p. 622, 1947.

[43] R. R. Nair, P. Blake, A. N. Grigorenko, K. S. Novoselov, T. J. Booth, T. Stauber, N. M. Peres, and A. K. Geim, "Fine structure constant defines visual transparency of graphene," *Science*, vol. 320, no. 5881, pp. 1308–1308, 2008.

[44] F. Bonaccorso, Z. Sun, T. Hasan, and A. Ferrari, "Graphene photonics and optoelectronics," *Nature Photonics*, vol. 4, no. 9, pp. 611–622, 2010.

[45] S. Zhou, G.-H. Gweon, J. Graf, A. Fedorov, C. Spataru, R. Diehl, Y. Kopelevich, D.-H. Lee, S. G. Louie, and A. Lanzara, "First direct observation of dirac fermions in graphite," *Nature Physics*, vol. 2, no. 9, pp. 595–599, 2006.

[46] C. Guan, S. Li, Y. Shen, T. Yuan, J. Yang, and L. Yuan, "Graphene-coated surface core fiber polarizer," *Journal of Lightwave Technology*, vol. 33, no. 2, pp. 349–353, 2015.

[47] J. Gosciniak and D. T. Tan, "Theoretical investigation of graphene-based photonic modulators," *Scientific Reports*, vol. 3, p. 1897, 2013.

[48] J. Horng, C.-F. Chen, B. Geng, C. Girit, Y. Zhang, Z. Hao, H. A. Bechtel, M. Martin, A. Zettl, M. F. Crommie, *et al.*, "Drude conductivity of dirac fermions in graphene," *Physical Review B*, vol. 83, no. 16, p. 165113, 2011.

[49] Z. Li and J. Carbotte, "Longitudinal and spin-valley hall optical conductivity in single layer mos2," *Physical Review B*, vol. 86, no. 20, p. 205425, 2012.

[50] K. F. Mak, K. He, J. Shan, and T. F. Heinz, "Control of valley polarization in monolayer mos2 by optical helicity," *Nature Nanotechnology*, vol. 7, no. 8, pp. 494–498, 2012.

[51] Y. Tan, R. He, C. Cheng, D. Wang, Y. Chen, and F. Chen, "Polarization-dependent optical absorption of mos2 for refractive index sensing," *Scientific Reports*, vol. 4, p. 7523, 2014.

[52] G. P. Agrawal, *Nonlinear fiber optics*. Academic press, 2007.

[53] E. Hendry, P. J. Hale, J. Moger, A. Savchenko, and S. Mikhailov, "Coherent nonlinear optical response of graphene," *Physical review letters*, vol. 105, no. 9, p. 097401, 2010.

[54] Q. Bao, H. Zhang, Y. Wang, Z. Ni, Y. Yan, Z. X. Shen, K. P. Loh, and D. Y. Tang, "Atomic-layer graphene as a saturable absorber for ultrafast pulsed lasers," *Advanced Functional Materials*, vol. 19, no. 19, pp. 3077–3083, 2009.

[55] N. Healy, *Robust Optical Fibre Devices*. PhD thesis, University of Limerick, 2006.

[56] C. Hussey and J. Minelly, "Optical fibre polishing with a motor-driven polishing wheel," *Electronics Letters*, vol. 24, no. 13, pp. 805–807, 1988.

[57] A. T. Andreev, B. S. Zafirova, and E. I. Karakoleva, "Single-mode fiber polished into the core as a sensor element," *Sensors and Actuators A: Physical*, vol. 64, no. 3, pp. 209–212, 1998.

[58] S.-M. Tseng and C.-L. Chen, "Side-polished fibers," *Applied Optics*, vol. 31, no. 18, pp. 3438–3447, 1992.

[59] L. Yao, T. Birks, and J. C. Knight, "Low bend loss in tightly-bent fibers through adiabatic bend transitions," *Optics express*, vol. 17, no. 4, pp. 2962–2967, 2009.

[60] D. Golini and S. D. Jacobs, "Transition between brittle and ductile mode in loose abrasive grinding," in *San Dieg-DL Tentative*, pp. 80–91, International Society for Optics and Photonics, 1990.

[61] K. L. Blaedel, J. S. Taylor, and C. J. Evans, "Ductile-regime grinding of brittle materials," *MANUFACTURING ENGINEERING AND MATERIALS PROCESSING*, vol. 53, pp. 139–176, 1999.

[62] R. B. Mindek, E. Whitenton, and C. Evans, "Visualization of grit interactions during the ductile to brittle polishing transition," *TRANSACTIONS-NORTH AMERICAN MANUFACTURING RESEARCH INSTITUTION OF SME*, pp. 213–220, 2001.

[63] L. Yin, H. Huang, W. Chen, Z. Xiong, Y. Liu, and P. Teo, "Polishing of fiber optic connectors," *International Journal of Machine Tools and Manufacture*, vol. 44, no. 6, pp. 659–668, 2004.

[64] P. Hariharan, *Optical interferometry*. Academic press, 2003.

[65] P. de Groot, "Principles of interference microscopy for the measurement of surface topography," *Advances in Optics and Photonics*, vol. 7, no. 1, pp. 1–65, 2015.

[66] J. Reed, M. Teitell, and J. Schmidt, "Biomedical optics & medical imaging interference microscopy offers new applications for biomedical research,"

[67] D. Stokes, *Principles and practice of variable pressure: environmental scanning electron microscopy (VP-ESEM)*. John Wiley & Sons, 2008.

[68] K. S. Novoselov, A. K. Geim, S. Morozov, D. Jiang, M. Katsnelson, I. Grigorieva, S. Dubonos, and A. Firsov, "Two-dimensional gas of massless dirac fermions in graphene," *Nature*, vol. 438, no. 7065, pp. 197–200, 2005.

[69] Y. Zhang, L. Zhang, and C. Zhou, "Review of chemical vapor deposition of graphene and related applications," *Accounts of Chemical Research*, vol. 46, no. 10, pp. 2329–2339, 2013.

[70] C. C. Huang, F. Al-Saab, Y. Wang, J.-Y. Ou, J. C. Walker, S. Wang, B. Gholipour, R. E. Simpson, and D. W. Hewak, "Scalable high-mobility mos 2 thin films fabricated by an atmospheric pressure chemical vapor deposition process at ambient temperature," *Nanoscale*, vol. 6, no. 21, pp. 12792–12797, 2014.

[71] C. Mattevi, H. Kim, and M. Chhowalla, "A review of chemical vapour deposition of graphene on copper," *Journal of Materials Chemistry*, vol. 21, no. 10, pp. 3324–3334, 2011.

[72] J. Creighton and P. Ho, "Introduction to chemical vapor deposition (cvd)," 2001.

[73] F. Bonaccorso, A. Lombardo, T. Hasan, Z. Sun, L. Colombo, and A. C. Ferrari, "Production and processing of graphene and 2d crystals," *Materials Today*, vol. 15, no. 12, pp. 564–589, 2012.

[74] M. S. Dresselhaus, A. Jorio, M. Hofmann, G. Dresselhaus, and R. Saito, "Perspectives on carbon nanotubes and graphene raman spectroscopy," *Nano Letters*, vol. 10, no. 3, pp. 751–758, 2010.

[75] A. C. Ferrari, "Raman spectroscopy of graphene and graphite: disorder, electron–phonon coupling, doping and nonadiabatic effects," *Solid State Communications*, vol. 143, no. 1, pp. 47–57, 2007.

[76] L. Malard, M. Pimenta, G. Dresselhaus, and M. Dresselhaus, "Raman spectroscopy in graphene," *Physics Reports*, vol. 473, no. 5, pp. 51–87, 2009.

[77] G. Wilkinson, "Light scattering in solids ii," *Journal of Modern Optics*, vol. 29, no. 12, pp. 1585–1585, 1982.

[78] J. R. Ferraro, *Introductory raman spectroscopy*. Academic press, 2003.

[79] D. Haberer, D. Vyalikh, S. Taioli, B. Dora, M. Farjam, J. Fink, D. Marchenko, T. Pichler, K. Ziegler, S. Simonucci, *et al.*, "Tunable band gap in hydrogenated quasi-free-standing graphene," *Nano Letters*, vol. 10, no. 9, pp. 3360–3366, 2010.

[80] A. Ferrari, J. Meyer, V. Scardaci, C. Casiraghi, M. Lazzeri, F. Mauri, S. Piscanec, D. Jiang, K. Novoselov, S. Roth, *et al.*, "Raman spectrum of graphene and graphene layers," *Physical Review Letters*, vol. 97, no. 18, p. 187401, 2006.

[81] H. Li, Q. Zhang, C. C. R. Yap, B. K. Tay, T. H. T. Edwin, A. Olivier, and D. Baillargeat, "From bulk to monolayer mos2: evolution of raman scattering," *Advanced Functional Materials*, vol. 22, no. 7, pp. 1385–1390, 2012.

[82] P. Bertrand, "Surface-phonon dispersion of mos 2," *Physical Review B*, vol. 44, no. 11, p. 5745, 1991.

[83] C. Lee, H. Yan, L. E. Brus, T. F. Heinz, J. Hone, and S. Ryu, "Anomalous lattice vibrations of single-and few-layer mos2," *ACS Nano*, vol. 4, no. 5, pp. 2695–2700, 2010.

[84] C. Yim, M. O'Brien, N. McEvoy, S. Winters, I. Mirza, J. G. Lunney, and G. S. Duesberg, "Investigation of the optical properties of mos2 thin films using spectroscopic ellipsometry," *Applied Physics Letters*, vol. 104, no. 10, p. 103114, 2014.

[85] W. Regan, N. Alem, B. Aleman, B. Geng, C. Girit, L. Maserati, F. Wang, M. Crommie, and A. Zettl, "A direct transfer of layer-area graphene," *Applied Physics Letters*, vol. 96, no. 11, p. 113102, 2010.

[86] Y. Wang, Y. Zheng, X. Xu, E. Dubuisson, Q. Bao, J. Lu, and K. P. Loh, "Electrochemical delamination of cvd-grown graphene film: toward the recyclable use of copper catalyst," *ACS Nano*, vol. 5, no. 12, pp. 9927–9933, 2011.

[87] A. Reina, X. Jia, J. Ho, D. Nezich, H. Son, V. Bulovic, M. S. Dresselhaus, and J. Kong, "Large area, few-layer graphene films on arbitrary substrates by chemical vapor deposition," *Nano Letters*, vol. 9, no. 1, pp. 30–35, 2008.

[88] L.-J. Chen, J.-D. Liao, S.-J. Lin, Y.-J. Chuang, and Y.-S. Fu, "Synthesis and characterization of pvb/silica nanofibers by electrospinning process," *Polymer*, vol. 50, no. 15, pp. 3516–3521, 2009.

[89] D. Ma, J. Shi, Q. Ji, K. Chen, J. Yin, Y. Lin, Y. Zhang, M. Liu, Q. Feng, X. Song, *et al.*, "A universal etching-free transfer of mos2 films for applications in photodetectors," *Nano Research*, vol. 8, no. 11, pp. 3662–3672, 2015.

[90] Z. Zhu, C. Guo, K. Liu, J. Zhang, W. Ye, X. Yuan, and S. Qin, "Electrically controlling the polarizing direction of a graphene polarizer," *Journal of Applied Physics*, vol. 116, no. 10, p. 104304, 2014.

[91] D. H. Goldstein, *Polarized light*. CRC Press, 2010.

[92] J. Feth and C. Chang, "Metal-clad fiber-optic cutoff polarizer," *Optics Letters*, vol. 11, no. 6, pp. 386–388, 1986.

[93] K. Liu, W. Sorin, and H. Shaw, "Single-mode-fiber evanescent polarizer/amplitude modulator using liquid crystals," *Optics Letters*, vol. 11, no. 3, pp. 180–182, 1986.

[94] Y. V. Bludov, M. I. Vasilevskiy, and N. M. Peres, "Tunable graphene-based polarizer," *Journal of Applied Physics*, vol. 112, no. 8, p. 084320, 2012.

[95] J. T. Kim and C.-G. Choi, "Graphene-based polymer waveguide polarizer," *Optics Express*, vol. 20, no. 4, pp. 3556–3562, 2012.

[96] V. Gusynin, S. Sharapov, and J. Carbotte, "Unusual microwave response of dirac quasiparticles in graphene," *Physical Review Letters*, vol. 96, no. 25, p. 256802, 2006.

[97] N. Peres, "Colloquium: The transport properties of graphene: An introduction," *Reviews of Modern Physics*, vol. 82, no. 3, p. 2673, 2010.

[98] K. F. Mak, M. Y. Sfeir, Y. Wu, C. H. Lui, J. A. Misewich, and T. F. Heinz, "Measurement of the optical conductivity of graphene," *Physical Review Letters*, vol. 101, no. 19, p. 196405, 2008.

[99] G. T. Reed, G. Mashanovich, F. Gardes, and D. Thomson, "Silicon optical modulators," *Nature Photonics*, vol. 4, no. 8, pp. 518–526, 2010.

[100] S. Yu, X. Wu, Y. Wang, X. Guo, and L. Tong, "2d materials for optical modulation: Challenges and opportunities," *Advanced Materials*, 2017.

[101] Z. Sun, A. Martinez, and F. Wang, "Optical modulators with 2d layered materials," *Nature Photonics*, vol. 10, no. 4, pp. 227–238, 2016.

[102] L. Li, Y. Yu, G. J. Ye, Q. Ge, X. Ou, H. Wu, D. Feng, X. H. Chen, and Y. Zhang, "Black phosphorus field-effect transistors," *Nature Nanotechnology*, vol. 9, no. 5, pp. 372–377, 2014.

[103] R. L. Gieseking, S. Mukhopadhyay, C. Risko, S. R. Marder, and J.-L. Brédas, "25th anniversary article: Design of polymethine dyes for all-optical switching applications: Guidance from theoretical and computational studies," *Advanced Materials*, vol. 26, no. 1, pp. 68–84, 2014.

[104] J. Cheng, N. Vermeulen, and J. Sipe, "Third order optical nonlinearity of graphene," *New Journal of Physics*, vol. 16, no. 5, p. 053014, 2014.

[105] G. Xing, H. Guo, X. Zhang, T. C. Sum, and C. H. A. Huan, "The physics of ultrafast saturable absorption in graphene," *Optics Express*, vol. 18, no. 5, pp. 4564–4573, 2010.

[106] W. Li, B. Chen, C. Meng, W. Fang, Y. Xiao, X. Li, Z. Hu, Y. Xu, L. Tong, H. Wang, *et al.*, "Ultrafast all-optical graphene modulator," *Nano Letters*, vol. 14, no. 2, pp. 955–959, 2014.

[107] Z. Sun, T. Hasan, F. Torrisi, D. Popa, G. Privitera, F. Wang, F. Bonaccorso, D. M. Basko, and A. C. Ferrari, "Graphene mode-locked ultrafast laser," *ACS Nano*, vol. 4, no. 2, pp. 803–810, 2010.

[108] S. Yu, X. Wu, K. Chen, B. Chen, X. Guo, D. Dai, L. Tong, W. Liu, and Y. R. Shen, "All-optical graphene modulator based on optical kerr phase shift," *Optica*, vol. 3, no. 5, pp. 541–544, 2016.

[109] L. Shen, N. Healy, C. J. Mitchell, J. S. Penades, M. Nedeljkovic, G. Z. Mashanovich, and A. C. Peacock, "Mid-infrared all-optical modulation in low-loss germanium-on-silicon waveguides," *Optics Letters*, vol. 40, no. 2, pp. 268–271, 2015.

[110] J.-l. Kou, J.-h. Chen, Y. Chen, F. Xu, and Y.-q. Lu, "Platform for enhanced light–graphene interaction length and miniaturizing fiber stereo devices," *Optica*, vol. 1, no. 5, pp. 307–310, 2014.

[111] M. Liu, X. Yin, and X. Zhang, "Double-layer graphene optical modulator," *Nano Letters*, vol. 12, no. 3, pp. 1482–1485, 2012.

[112] B. Nechay, U. Siegner, M. Achermann, H. Bielefeldt, and U. Keller, "Femtosecond pump-probe near-field optical microscopy," *Review of Scientific Instruments*, vol. 70, no. 6, pp. 2758–2764, 1999.

[113] J. M. Dawlaty, S. Shivaraman, M. Chandrashekhar, F. Rana, and M. G. Spencer, "Measurement of ultrafast carrier dynamics in epitaxial graphene," *Applied Physics Letters*, vol. 92, no. 4, p. 042116, 2008.

[114] M. Mohsin, D. Schall, M. Otto, A. Noculak, D. Neumaier, and H. Kurz, "Graphene based low insertion loss electro-absorption modulator on soi waveguide," *Optics Express*, vol. 22, no. 12, pp. 15292–15297, 2014.

[115] H. Zhang, N. Healy, L. Shen, C. C. Huang, D. W. Hewak, and A. C. Peacock, "Enhanced all-optical modulation in a graphene-coated fibre with low insertion loss," *Scientific Reports*, vol. 6, p. 23512, 2016.

[116] C. T. Phare, Y.-H. D. Lee, J. Cardenas, and M. Lipson, "Graphene electro-optic modulator with 30 ghz bandwidth," *Nature Photonics*, vol. 9, no. 8, pp. 511–514, 2015.

[117] S. J. Koester and M. Li, "High-speed waveguide-coupled graphene-on-graphene optical modulators," *Applied Physics Letters*, vol. 100, no. 17, p. 171107, 2012.

[118] N. Kuse, C.-C. Lee, J. Jiang, C. Mohr, T. Schibli, and M. Fermann, "Ultra-low noise all polarization-maintaining er fiber-based optical frequency combs facilitated with a graphene modulator," *Optics Express*, vol. 23, no. 19, pp. 24342–24350, 2015.

[119] K. Roy, M. Padmanabhan, S. Goswami, T. P. Sai, G. Ramalingam, S. Raghavan, and A. Ghosh, "Graphene-mos2 hybrid structures for multifunctional photoresponsive memory devices," *Nature Nanotechnology*, vol. 8, no. 11, pp. 826–830, 2013.

[120] C.-C. Huang, F. Al-Saab, Y. Wang, J.-Y. Ou, J. C. Walker, S. Wang, B. Gholipour, R. E. Simpson, and D. W. Hewak, "Scalable high-mobility mos 2 thin films fabricated by an atmospheric pressure chemical vapor deposition process at ambient temperature," *Nanosc.*, vol. 6, no. 21, pp. 12792–12797, 2014.

[121] Z.-C. Luo, M. Liu, H. Liu, X.-W. Zheng, A.-P. Luo, C.-J. Zhao, H. Zhang, S.-C. Wen, and W.-C. Xu, "2 ghz passively harmonic mode-locked fiber laser by a microfiber-based topological insulator saturable absorber," *Optics Letters*, vol. 38, no. 24, pp. 5212–5215, 2013.

[122] H. Liu, A.-P. Luo, F.-Z. Wang, R. Tang, M. Liu, Z.-C. Luo, W.-C. Xu, C.-J. Zhao, and H. Zhang, "Femtosecond pulse erbium-doped fiber laser by a few-layer mos 2 saturable absorber," *Optics Letters*, vol. 39, no. 15, pp. 4591–4594, 2014.

[123] M. Liu, X.-W. Zheng, Y.-L. Qi, H. Liu, A.-P. Luo, Z.-C. Luo, W.-C. Xu, C.-J. Zhao, and H. Zhang, "Microfiber-based few-layer mos 2 saturable absorber for 2.5 ghz passively harmonic mode-locked fiber laser," *Optics Express*, vol. 22, no. 19, pp. 22841–22846, 2014.

[124] H. Xia, H. Li, C. Lan, C. Li, X. Zhang, S. Zhang, and Y. Liu, "Ultrafast erbium-doped fiber laser mode-locked by a cvd-grown molybdenum disulfide (mos 2) saturable absorber," *Optics Express*, vol. 22, no. 14, pp. 17341–17348, 2014.

[125] G. P. Agrawal, *Nonlinear Fiber Optics*. Academic Press, 2012.

[126] Y. Yamamoto, Y. Tamura, and T. Hasegawa, "Silica-based highly nonlinear fibers and their applications," *SEI Tech. Rev.*, vol. 83, pp. 15–20, 2016.

[127] K. Saitoh and M. Koshiba, "Highly nonlinear dispersion-flattened photonic crystal fibers for supercontinuum generation in a telecommunication window," *Opt. Express*, vol. 12, no. 10, pp. 2027–2032, 2004.

[128] K. Saitoh and S. Matsuo, "Multicore fiber technology," *Journal of Lightwave Technology*, vol. 34, no. 1, pp. 55–66, 2016.

[129] K. S. Abedin *et al.*, "Amplification and noise properties of an erbium-doped multicore fiber amplifier," *Optics Express*, vol. 19, no. 17, pp. 16715–16721, 2011.

[130] T. Hayashi, T. Taru, O. Shimakawa, T. Sasaki, and E. Sasaoka, "Characterization of crosstalk in ultra-low-crosstalk multi-core fiber," *Journal of Lightwave Technology*, vol. 30, p. 583, 2012.

[131] R. Van Uden *et al.*, "Ultra-high-density spatial division multiplexing with a few-mode multicore fibre," *Nature Photonics*, vol. 8, no. 11, pp. 865–870, 2014.

[132] T. Almeida, A. Shahpari, A. Rocha, R. Oliveira, F. Guiomar, A. Pinto, A. L. Teixeira, P. André, and R. N. Nogueira, "Experimental demonstration of selective core coupling in multicore fibers of a 200 gb/s dp-16qam signal," in *Proc. OFC*, pp. 1–3, IEEE, 2016.

[133] J. M. Senior and M. Y. Jamro, *Optical fiber communications: principles and practice*. Pearson Education, 2009.

[134] H. Zhang, N. Healy, S. Dasgupta, J. R. Hayes, M. N. Petrovich, D. J. Richardson, and A. C. Peacock, "A tuneable multi-core to single mode fiber coupler," *IEEE Photonics Technology Letters*, vol. 29, no. 7, pp. 591–594, 2017.

[135] M. Yoshida *et al.*, "Fused type fan-out device for multi-core fiber based on bundled structure," in *Proc. OFC*, pp. 1–3, IEEE, 2016.

[136] D. Noordegraaf, P. M. Skovgaard, M. D. Nielsen, and J. Bland-Hawthorn, "Efficient multi-mode to single-mode coupling in a photonic lantern," *Optics Express*, vol. 17, no. 3, pp. 1988–1994, 2009.

[137] L. Yuan, Z. Liu, and J. Yang, "Coupling characteristics between single-core fiber and multicore fiber," *Optics Letters*, vol. 31, no. 22, pp. 3237–3239, 2006.

[138] M. Koshiba, K. Saitoh, and Y. Kokubun, "Heterogeneous multi-core fibers: proposal and design principle," *IEICE Electron. Express*, vol. 6, no. 2, pp. 98–103, 2009.

[139] G. Ren, P. Shum, J. Hu, X. Yu, and Y. Gong, "Fabrication of all-solid photonic bandgap fiber coupler," *Optics Letters*, vol. 32, no. 21, pp. 3059–3061, 2007.

[140] A. W. Snyder, "Coupled-mode theory for optical fibers," *Journal of the Optical Society of America*, vol. 62, no. 11, pp. 1267–1277, 1972.

[141] B. M. Beam, R. C. Shallcross, J. Jang, N. R. Armstrong, and S. B. Mendes, "Planar fiber-optic chips for broadband spectroscopic interrogation of thin films," *Applied Spectroscopy*, vol. 61, no. 6, pp. 585–592, 2007.